

Analysis and improvement of irradiance modelling algorithms for the simulation of photovoltaic systems

Von der Fakultät für Mathematik und Physik
der Gottfried Wilhelm Leibniz Universität Hannover

zur Erlangung des Grades
Doktor der Naturwissenschaften
Dr. rer. nat.

genehmigte Dissertation von

M.Sc. Martin Hofmann
geboren am 16.04.1983 in Mannheim

2019

Referent: Prof. Dr. Gunther Seckmeyer

1. Korreferent: Prof. Dr.-Ing. Rolf Brendel

2. Korreferent: Prof. Dr.-Ing. Volker Quaschnig

Tag der Promotion: 25.04.2019

Peer reviewed articles of this cumulated thesis

This thesis is a cumulated thesis based on the following peer-reviewed open access articles:

- [1] M. Hofmann, S. Riechelmann, C. Crisosto, R. Mubarak and G. Seckmeyer, "Improved synthesis of global irradiance with one-minute resolution for PV system simulations," *Int. J. Photoenergy*, vol. 2014, 2014.
<https://www.hindawi.com/journals/ijp/2014/808509/>
- [2] M. Hofmann and G. Seckmeyer, "A New Model for Estimating the Diffuse Fraction of Solar Irradiance for Photovoltaic System Simulations," *Energies*, vol. 10, no. 2, p. 248, 2017
<http://www.mdpi.com/1996-1073/10/2/248>
- [3] M. Hofmann and G. Seckmeyer, "Influence of Various Irradiance Models and Their Combination on Simulation Results of Photovoltaic Systems," *Energies*, vol. 10, no. 10, p. 1495, Sep. 2017.
<http://www.mdpi.com/1996-1073/10/10/1495>
- [4] R. Mubarak, M. Hofmann, S. Riechelmann and G. Seckmeyer, "Comparison of Modelled and Measured Tilted Solar Irradiance for Photovoltaic Applications," *Energies*, vol. 10, no. 11, p. 1688, Oct. 2017.
<http://www.mdpi.com/1996-1073/10/11/1688>

Table of contents

Peer reviewed articles of this cumulated thesis	3
Table of contents.....	5
1 Summary.....	7
1.1 Abstract (EN)	7
1.2 Zusammenfassung (DE)	8
2 Introduction.....	9
2.1 PV Market development and economic aspects of PV simulations	9
2.2 Short introduction into the meteorology of solar irradiance.....	10
2.2.1 Clouds.....	11
2.2.2 Aerosols.....	12
2.2.3 Water vapor.....	13
2.2.4 Oxygen, ozone and other atmospheric gases.....	14
2.2.5 Air Mass, Geometry	15
2.3 Irradiance components.....	15
2.4 Meteorological modelling for PV system simulations	16
2.5 The challenge of model validation.....	18
2.6 Preparation of the measurement database	19
2.6.1 Description of the measurement data mainly used in the presented papers.....	19
2.6.2 Structure.....	22
2.6.3 Queries.....	25
2.6.4 Advantages of the database design.....	26
3 Peer-reviewed publications and their context.....	29
3.1 Synthesis of one-minute time series from one-hour data.....	29
3.2 Diffuse decomposition models.....	41
3.3 Influence of meteorological models on PV system simulations.....	65
3.4 Transposition models for the solar irradiance on tilted surfaces.....	91
4 Outlook.....	111
5 Declaration of Authorship / Eidesstattliche Erklärung.....	112
6 Acknowledgements.....	113
7 References	114
Curriculum Vitae	119

1 Summary

1.1 Abstract (EN)

The electricity generation from photovoltaic systems (PV) is becoming more relevant from year to year in the context of global power generation, with the newly installed capacity exceeding all other forms of generation for the first time in 2016. With its triumphal sweep around the globe, it is becoming increasingly cheap, more competitive in more places and thus an increasingly important pillar of our energy system.

This is accompanied by increasing demands on the quality of solar energy yield forecasts, as these form the basis for every investment decision. Furthermore, yield forecasts form an important basis for grid operators and actors in the energy market, on which the power generated must be brought into line with the power consumed at all times. At present, major energy yield forecast uncertainties are caused by the input data – time series of global irradiance which are mostly available in one-hour resolution – and by the models which convert these data into the irradiance at the PV module level.

To reduce these uncertainties, this work introduces two new algorithms and validates many existing ones with a very large set of measurement data. The validation data-set comprises high-quality measurement data of the Baseline Surface Radiation Network (BSRN), covering a large part of the Earth's climate zones.

The first algorithm synthesizes time series of global irradiance of one minute resolution from time series with one hour resolution. Thanks to this algorithm it is possible to simulate PV systems with statistically representative, synthetic input data with a resolution of one minute even at locations where only hourly measured data is available. Compared to existing algorithms the new approach is capable of producing substantially more natural frequency distributions of the global irradiance, of the irradiance gradients and of the clear-sky index. The root mean squared deviation (RMSD) of the global irradiance distribution is reduced by 61%, the RMSD of the gradients by 52% and the RMSD of the clear-sky index by 71%.

In addition, a new model for calculating the diffuse fraction of the global irradiance is presented and compared with a selection of existing models. The new approach realizes a reduction by 50% of the deviations of the modelled from measured diffuse irradiation per year, the RMSD is reduced by 18%. In contrast to existing models, the annual deviation of the diffuse irradiation is smaller than 20% in all cases, while it is smaller than 10% in 80% of the analyzed test cases.

It is a complex and time consuming task to implement these two algorithms. In order to be usable by fellow researchers, they are publicly available on <http://www.pvmodelling.org>.

A comprehensive matrix simulation analysis forms the third part of the thesis. A wide range of available irradiance models, different simulation time steps and orientations of the PV modules are combined with each other to analyze the effects of the different models on the irradiance on the inclined module surface and finally the PV yield. Thanks to this data, it is possible to evaluate the interaction of the models and the time step for different PV systems with regard to energy yield simulations.

The thesis is rounded off by a detailed validation study of models that calculate the global irradiance on tilted surfaces. A validation dataset of long-term irradiance measurements at two locations and 19 different PV module orientations with one minute resolution is used to evaluate the performance of five transposition models. The study helps to answer important questions about the model uncertainties for calculating the irradiance for differently oriented PV module. Recommendations for locations with mostly cloudless or overcast skies are developed as well.

Keywords: Photovoltaics, Solar, Irradiance, Modelling, Simulation

1.2 Zusammenfassung (DE)

Titel: Analyse und Weiterentwicklung von Algorithmen zur Strahlungsmodellierung für die Simulation photovoltaischer Systeme

Die Stromerzeugung aus photovoltaischen Anlagen (PV) wird im Kontext der globalen Stromerzeugung von Jahr zu Jahr relevanter, die neu installierte Leistung überstieg im Jahr 2016 erstmals alle anderen Erzeugungsformen. Mit ihrem Siegeszug rund um den Globus wird sie immer günstiger, an immer mehr Orten konkurrenzfähig und so zunehmend zu einer wichtigen Säule unseres Energiesystems.

Damit gehen steigende Qualitäts-Anforderungen an Ertragsprognosen einher, da diese die Grundlage für jede Investitionsentscheidung bilden und eine wichtige Entscheidungshilfe für Akteure des Energiemarkts sind. Große Unsicherheitsfaktoren liegen derzeit vor allem in den Eingangsdaten für die Modellierung – den zumeist stündlich aufgelösten Globalstrahlungsdaten – und den Modellen, die diese Daten umrechnen zur Strahlung auf die PV-Modul-Ebene.

Um die Unsicherheiten in der Strahlungsmodellierung zu reduzieren, werden in dieser Arbeit zwei neue Algorithmen vorgestellt und viele existierende mit einem sehr großen Messdatensatz validiert. Der Validierungs-Datensatz umfasst die hochwertigen Messdaten des Baseline Surface Radiation Networks (BSRN), die einen Großteil der Klimazonen der Erde abdecken.

Der erste Algorithmus dient der Synthese von minütlich aufgelösten Zeitreihen aus stündlich aufgelösten Zeitreihen der Globalstrahlung vor. Damit ist es möglich, PV-Anlagen auch an Standorten, an denen nur stündlich aufgelöste Messdaten vorliegen, mit statistisch repräsentativen synthetischen Daten in einer Auflösung von einer Minute zu simulieren. Verglichen mit bestehenden Algorithmen liefert der neue Ansatz wesentlich natürlichere Häufigkeitsverteilungen der Globalstrahlung, der Gradienten und des Clear-Sky-Indizes. Die mittlere quadratische Abweichung (RMSD) der Globalstrahlungsverteilung wird um 61 % reduziert, der RMSD der Strahlungsgradienten um 52 % und der des Clear-Sky-Indizes um 71 %.

Außerdem wird ein neues Modell zur Berechnung des Diffusanteils vorgestellt und mit einer Auswahl bereits existierender Modelle verglichen. Der neue Ansatz erreicht im Mittel eine Reduktion der Abweichungen der modellierten von der gemessenen Diffusstrahlung pro Jahr um 50 %, der RMSD kann um 18 % reduziert werden. Im Gegensatz zu den anderen Modellen ist die Abweichung der Jahressummen in keinem der untersuchten Fälle größer als 20 %, wobei in 80 % aller Fälle die Abweichung geringer ist als 10 %.

Die Implementierung dieser beiden Algorithmen ist komplex und zeitaufwändig. Damit sie dennoch genutzt werden können, sind sie für Forscher unter <http://www.pvmodelling.org> öffentlich zugänglich.

Der dritte Teil der Arbeit ist eine umfassende Matrix-Simulation, in der eine große Auswahl an verfügbaren Strahlungsmodellen, verschiedenen Simulations-Zeitschritten und Ausrichtungen der PV-Anlage auf immer unterschiedliche Weise miteinander kombiniert wird, um die Auswirkungen der verschiedenen Modelle auf die Strahlung auf die geneigte Fläche und schließlich den PV-Ertrag zu analysieren. Dank dieser Daten ist es möglich, das Zusammenspiel der Modelle und des Zeitschritts für verschiedene PV-Systeme in Hinsicht auf die Ertragssimulation auf globaler Ebene zu bewerten.

Der vierte Teil der Arbeit ist eine detaillierte Validierungsstudie von Modellen, die die Globalstrahlung auf die geneigte Ebene berechnen. Es wird ein Datensatz von langjährigen Strahlungsmessungen an zwei Standorten mit 19 verschiedenen PV-Modul-Orientierungen und einer Auflösung von einer Minute verwendet, um die Performance von fünf Transpositionsmodellen zu bewerten. Die Studie hilft bei der Einschätzung von Modellunsicherheiten in Abhängigkeit von der Modulausrichtung und stellt Empfehlungen zur Nutzung von Modellen für Standorte mit meist wolkenlosem oder bedecktem Himmel vor.

Schlagerworte: Photovoltaik, Solar, Strahlung, Modellierung, Simulation

2 Introduction

2.1 PV Market development and economic aspects of PV simulations

In their current report, SolarPower Europe (formerly EPIA) states that only a 35 % share of renewable energy production by 2030 would be able to keep the EU on the right track to the 2050 decarbonisation objectives [5]. For solar electricity systems, the reports estimates a total of newly installed capacity in the EU of 62.9 GW in the medium scenario and 98.6 GW in the highest scenario for the next five years until 2021.

With levelized costs of electricity (LCOE) of 0.06 €/kWh in Germany, solar electricity systems already constitute one of the most cost effective energy generation technologies [5]. A recent study of the US market reported comparable LCOE of 0.05 USD/kWh [6]. Another indicator of the recent rapid advances of the PV technology is that the energy payback time has fallen below a tenth of the guaranteed PV system lifetime nowadays. In the European Union the energy payback time is between 1.2 and 2.1 years depending on the annual irradiation [7].

With photovoltaic systems being cost competitive, zero-emission, with a low technical complexity and low-maintenance compared to both fossil and other renewable technologies like wind power or geothermal, a steep rise of the solar electricity share of the global energy production is probable.

While the return on assets (ROA) for average grid-connected PV systems with 100 to 120 kWp is in the range of comfortable 18 to 20% in upcoming European markets like Greece and Portugal, it can be observed that it decreases in markets with a high penetration of installed PV capacity and often lies between 7 and 10% [8] [5]. This implies that with increasing share of solar electricity the quality and reliability of economic calculations of PV systems must be improved in order to minimize uncertainties as much as possible.

Simulations that estimate the annual energy output of solar systems form the basis of all economic calculation and are of paramount importance for the bankability of solar power projects [9]. This is equally true for large-scale grid feed-in systems as well as smaller residential systems focused on self-consumption, a latter becoming more important in markets with high PV penetration like UK and Germany [5].

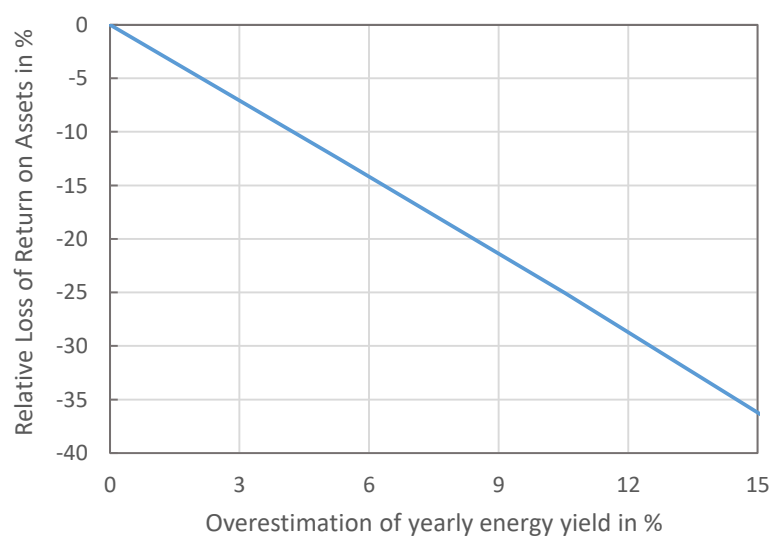


Figure 1. Modelled relative loss of the return on assets (ROA) as a function of the overestimation of the energy yield. If the yearly energy yield is overestimated by 5% by the simulation, the ROA will decrease by more than 10%.

In the following short example the sensitivity of the ROA on the energy yield simulations is demonstrated. A 10 kWp residential standard system in Berlin, Germany, was simulated using PV*SOL [10], resulting in an energy yield of 9935 kWh/a. With specific installation costs of 1500 €/kWp, a standard grid feed-in tariff according to the German EEG and no further economic aspects, the ROA is 5.1%. The simulation is repeated with different soiling loss factors to analyze how the ROA reacts to decreasing energy yields. Figure 1 illustrates the relationship of energy yield and ROA in form of a relative loss of ROA as a function of a hypothetical overestimation of the energy yield. If, for example, the simulated energy yield was 9935 kWh/a, but the real value was 5% less, then the ROA would reduce by more than 10%.

This indicates the importance of high quality solar irradiation data as input of the simulation models on the one hand as well as the necessity of high quality simulation models with lowest possible uncertainties. The publications presented in this thesis can be classified in the domain of solar simulation models, specifically in the subdomain of solar irradiance models and their impact on the electrical output of PV systems.

2.2 Short introduction into the meteorology of solar irradiance

Since major parts of this work concern the field of solar irradiance on the Earth's surface for photovoltaic applications, important aspects of the interaction of the solar irradiance and the Earth's atmosphere are presented in this section.

To comply with the common terminology in energy meteorology and to differentiate between the power and energy of the solar radiation, the word 'irradiance' is used in this work to denote the instantaneous solar power per square meter in W/m^2 , whereas the word 'irradiation' refers to the integral of the irradiance over time, thus denoting the energy of the solar radiation in Ws/m^2 or kWh/m^2 [11], [12].

The irradiance from the sun reaches the top of the Earth's atmosphere with a varying intensity of $1360.8 \pm 0.5 \text{ W}/\text{m}^2$ [13]. On its way through the atmosphere, different kinds of interaction alter the intensity, spectral composition and direction of the solar irradiance.

In Figure 2, the irradiance transit through the atmosphere is displayed schematically for conditions that are valid for a global yearly average. Absorption, reflection and scattering are the main effects that determine the quality and the quantity of the solar irradiance on the Earth's surface, the global horizontal irradiance (GHI). Absorption by aerosols, water vapor and gases like oxygen (O_2) and ozone (O_3) reduce the annual solar radiation by about 19%, whereas the absorption by clouds leads to a reduction by 4%. A fraction of 30% is reflected by backscattering to space by air molecules (7%), from clouds (16%) and from the ground (7%). The annual solar irradiance incident on the Earth's surface is $161 \text{ W}/\text{m}^2$ in average, or 47% of the extraterrestrial total (all [14], [15]).

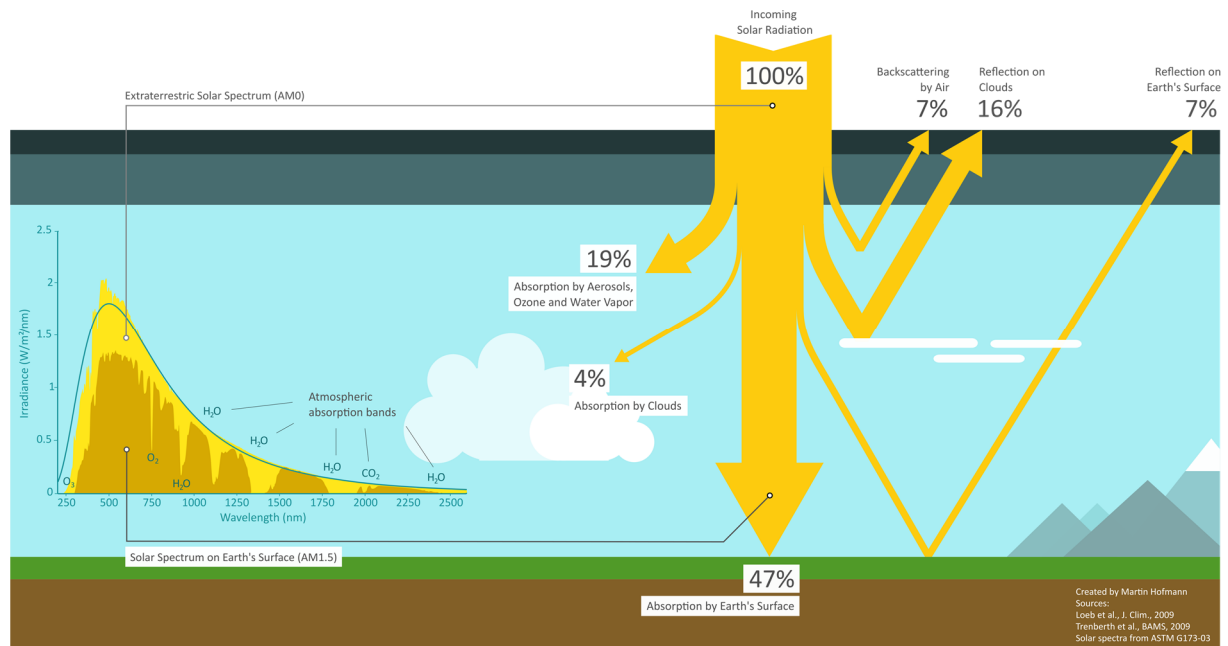


Figure 2. Right: Schema of the absorption and reflection of the incoming solar radiation. The global annual solar radiation energy balance is averaged over the Earth's surface with data from Mar 2000 to May 2004 [15][14]. The actual amount of solar energy incident on the Earth's surface varies strongly dependent on the location, season, time of day and composition of the atmosphere. Left: The solar spectrum is affected both quantitatively and qualitatively by aerosols, water vapor and gases like oxygen and ozone. The effect of attenuation is subject to the composition of the atmosphere, as well as the Air Mass. The spectra shown here are from the ASTM standard [16][17].

The spectral composition of the solar irradiance in the ultra-violet, visible and near infra-red spectrum is mainly influenced by selective absorption of water vapor (H₂O), oxygen (O₂) and ozone (O₃). The solar spectrum at the top of the Earth's atmosphere is similar to the spectrum of a black body with a temperature of 5700 K. The Fraunhofer lines, which are caused by selective absorptions in the sun's atmosphere significantly alter this extraterrestrial spectrum. Characteristic absorption bands from gases in the Earth's atmosphere further modify the spectrum that is observable at the Earth's surface, see Figure 2. The extinction depends on the composition of the atmosphere and on the path that the sunlight has to travel through the atmosphere. The path length for the direct beam is characterized by the Air Mass (AM), which is defined as the ratio relative to the path length vertically downwards, i.e. at the zenith. An example of a spectrum at the Earth's surface is given in Figure 2 on the left side for AM1.5.

The percentages in Figure 2 refer to long-term averages of the annual global radiation budget. The average is compiled over the Earth's surface with data from March 2000 to May 2004 [15]. It should be noted that absorption or reflection vary significantly with time and location and therefore differ from these averaged values. The most important factors that influence absorption, reflection and scattering in the atmosphere are clouds, aerosols, water vapor, oxygen, ozone and other trace gases as well as geometrical factors (e.g. sun height, Air Mass). The following sections will give a short overview on these factors and how they affect the solar irradiance on its way to the Earth's surface.

2.2.1 Clouds

The presence of clouds, the overall instantaneous cloud coverage, but also their shape, their position in the troposphere, their type (cumulus, stratos, etc.), their optical thickness and their microphysical properties show the strongest influence on the solar irradiance, both quantitatively and qualitatively. Being the most visible expression of the troposphere's state, it is easily observable that clouds show a strong temporal, geometrical and regional variability. Clouds interact with the solar irradiance by reflection, scattering and to a lesser extent by absorption. The wavelength-independent Mie scattering dominates the scattering

process. Reflection on clouds can also lead to irradiance enhancements, not only extinction, given that the geometry of solar angles, cloud position and shape supports it [18], [19].

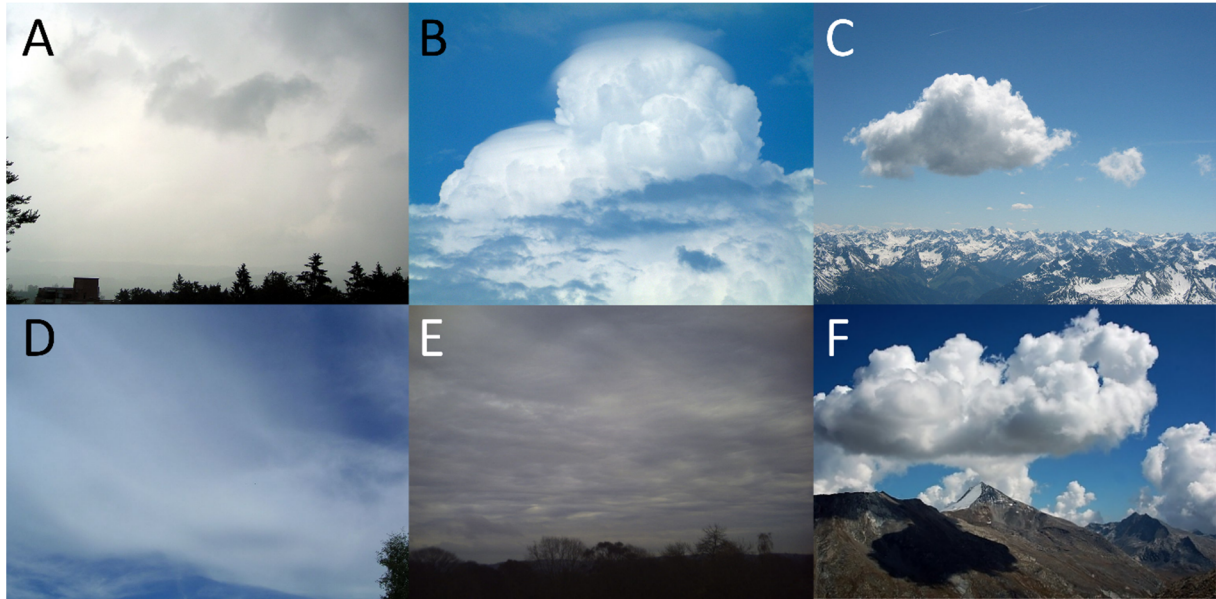


Figure 3. Illustrative examples of cloud types with varying reflection and absorption characteristics. A. nimbostratus clouds (with pannus clouds in the foreground); B. cumulonimbus (with small pileus on top); C. cumulus humilis; D. cirrostratus; E. altostratus; F. cumulus with static location. Source of above pictures: Wikipedia, published under CC BY-SA 3.0.

Both broadband and wavelength-dependent reflection and absorption in clouds are strongly dependent on the cloud characteristics and even vary over short time periods within a single observed cloud [20]. Overall broadband absorption rates for nimbostratus and cumulonimbus clouds are about 10 to 20%, while fair weather cumulus clouds only absorb around 4 to 9%. Thin stratus clouds show absorption rates of 1 to 6% only, while altostratus clouds can lead to 8 to 15% of absorbed irradiance. Reflection rates vary between 45% for thin stratus and up to 90% for cumulonimbus. In singular cases, airborne measurements showed instantaneous absorption rates of up to 40% that indicate the presence of hydrophobic aerosol particles in clouds that enhance the absorption rate that otherwise would have a theoretical limit of around 20% [21].

In addition to the microphysical properties of water or ice clouds (droplet size, ice crystal shape and distribution), the spectral reflection, absorption and scattering rates depend strongly on the angle of incidence of the solar irradiance [22].

2.2.2 Aerosols

Aerosols are airborne particles of diverse nature. Dust, sea salt, sand, biogenic and anthropogenic emissions are the most important [23]. Aerosols vary in size and concentration and there is a strong regional variation in the Aerosol Optical Depth (AOD) globally. Recent studies have confirmed that the AOD also varies significantly seasonally and even daily, while the AOD values also change with the wavelength [24], [25]. Figure 4 shows a heat map of the AOD at 550 nm with 15 years of data from the Terra/Modis satellites [26], averaged on a monthly basis, illustrating both the seasonal and regional variations.

Depending on their particle size and shape, aerosols influence the solar radiation by an interplay of Rayleigh and Mie scattering processes as well as absorption [27][28]. The ratio of the scattering coefficient to the total extinction coefficient is referred to as the single scattering albedo (SSA), where SSA values of 1 denote that the extinction is dominated completely by scattering. SSA values of 0 consequentially imply a complete extinction by absorption. The wavelength dependent optical thickness of aerosols AOD_{λ} can be approximatively expressed as

$$\frac{AOD_{\lambda}}{AOD_{\lambda_0}} = \left(\frac{\lambda}{\lambda_0}\right)^{-\alpha},$$

where AOD_{λ} is the optical thickness at the wavelength λ and AOD_{λ_0} the optical thickness at a second wavelength λ_0 . The Ångström exponent α relates the two ratios and is higher for smaller particle sizes [29], [30].

As a consequence of scattering and absorption, the AOD is not only forcing the total amount of global irradiance on the Earth's surface [31]–[33], but also affects the relation of direct to diffuse irradiance. The effect is wavelength dependent and is stronger at shorter wavelengths [34]. The Ångström formula expresses this relationship as

$$AOD_{\lambda} = \beta \lambda^{-\alpha},$$

where β is a dimensionless coefficient for the opacity of a vertical column of the atmosphere. It was found that an increase of the AOD at 550 nm is directly correlated to an increase of the broadband diffuse irradiance [35].

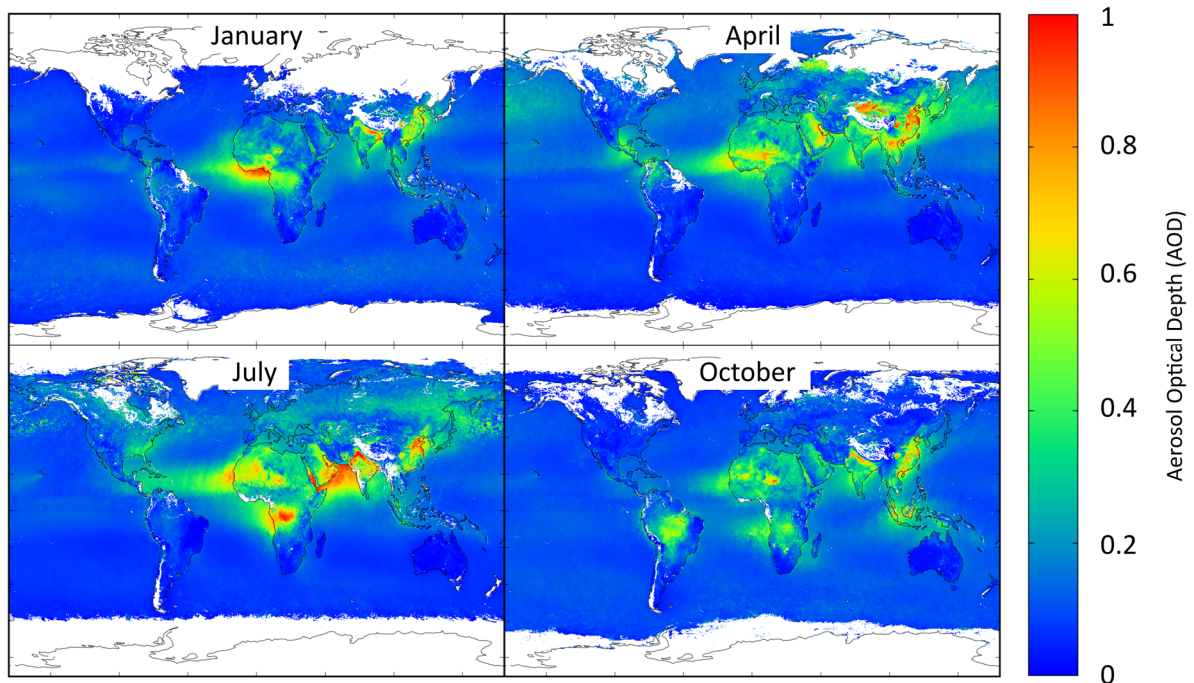


Figure 4. The Aerosol Optical Depth (AOD), as averages over 15 years from 2001 to 2015, with data taken from Terra/Modis satellites [26]. The AOD shows strong regional and seasonal variation.

A long-term study of aerosol measurements of the AERONET network [36] revealed that also the nature of aerosol particles influences the absorption rate. Absorption rates of desert dust aerosols are very weak above 550 nm, but pronounced in the blue spectral range (0.92 – 0.93 for wavelengths of 440nm). The optical properties of aerosols produced by burning of biomass depend on the type of vegetation and ratio of flaming to smoldering combustion. Aerosol absorption is significantly less for forest than grassland fire smokes. Anthropogenic aerosols emitted in urban areas feature varying absorption behavior depending on the type of industry [37].

2.2.3 Water vapor

Water vapor is omnipresent in the Earth's atmosphere, with its concentration ranging from about 5% in the troposphere to only 1 to 5 parts per million by volume (ppmv) in the stratosphere [38]. The water vapor concentration is also varying regionally and seasonally, illustrated by Figure 5. It absorbs the solar

irradiance at specific wavelength bands which leads to the characteristic gaps in the terrestrial solar spectrum, compare Figure 2. Mie scattering can also be observed on tiny water droplets.

The spectral absorption bands of water vapor start at wavelengths of around 720 nm and affect the solar spectrum towards higher wavelengths significantly, but with varying intensity [39]. Other absorption bands that are relevant for solar energy applications on the Earth's surface are around 810 nm, 930 nm, 1130 nm and 1370 nm, compare Table 1.

Measurements show that both the diffuse and the direct fraction of the solar irradiance are subject to water vapor absorption [40].

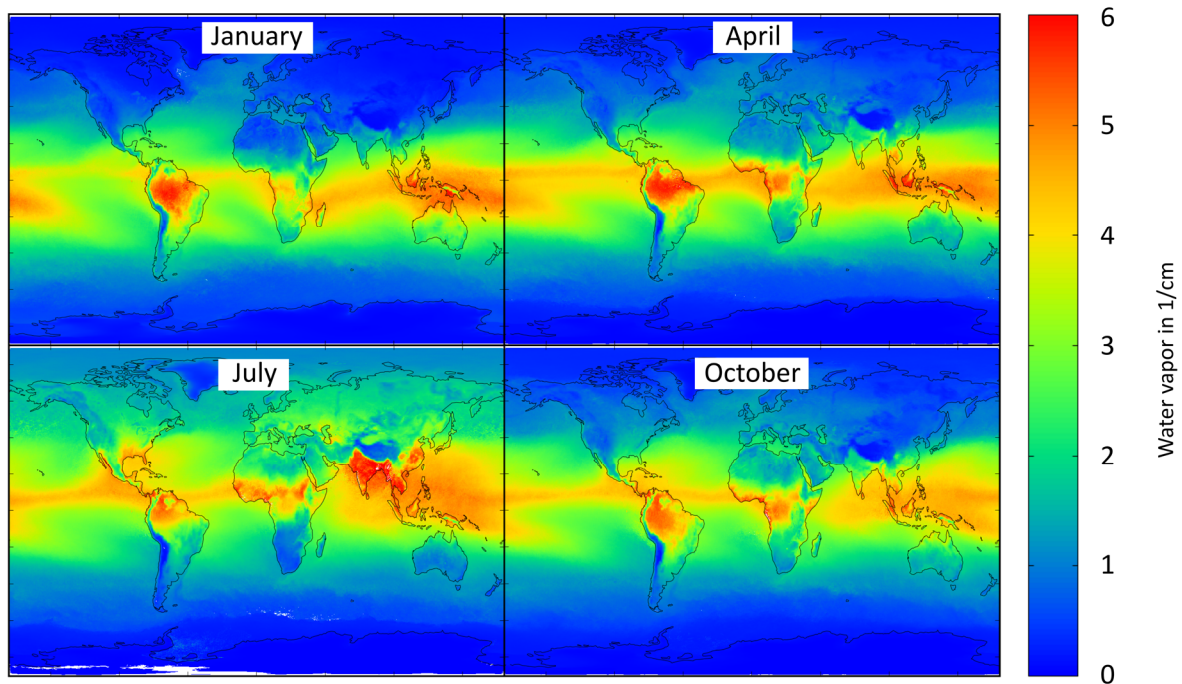


Figure 5. The column water vapor averaged over 15 years from 2001 to 2015, with data taken from Terra/Modis satellites [41]. Like the AOD and other properties of the atmosphere, the water vapor as well shows a strong regional and seasonal variation.

2.2.4 Oxygen, ozone and other atmospheric gases

Solar irradiance is also absorbed by oxygen, ozone and other trace gases of smaller concentrations. The absorption is wavelength dependent, which leads to a qualitative modification of the terrestrial spectrum with typical absorption bands, compare Figure 2.

The most important atmospheric gases that alter the solar spectrum in the ultra-violet, visible and near infra-red range, which forms the spectral range that is relevant for photovoltaic applications, are listed in Table 1.

Table 1. Absorption wavelength bands for selected atmospheric gases in the ultra-violet (UV), visible (VIS) and near infra-red spectrum up to wavelengths of 2 μm . From [39].

Atmospheric gas	Name	Absorption wavelengths in μm
O ₂	Oxygen	0.1 – 0.18, 0.2 – 0.24
O ₃	Ozone	0.22 – 0.29, 0.30 – 0.35, 0.69 – 0.76
H ₂ O	Water	0.72, 0.81, 0.93, 1.13, 1.37, 1.85
CO ₂	Carbon dioxide	1.46, 1.6, 2.04

Molecular nitrogen and oxygen in the troposphere are the main agents for Rayleigh scattering. This process of elastic scattering – the vector of incident direct irradiance is modified without modifying the wavelength

– is the most important source of the diffuse irradiance and the changes in the spectral composition of the global irradiance incident on the Earth’s surface [42]–[44].

2.2.5 Air Mass, Geometry

Another highly important factor that is influencing the extinction and modification of the solar irradiance on its way through the atmosphere is the distance that the solar irradiance has to travel until it reaches the surface of the Earth. The distance is expressed in relation to the distance when the solar elevation is 90° (sun zenith angle of 0°). This is referred to as the Air Mass (AM). While the AM is not affecting the solar irradiance directly, it is the intensity and the spectral effect of absorption, reflection and scattering processes that are depending on the AM. The AM itself is obviously depending on the solar elevation angle and hence on its daily and seasonal changes. Furthermore, the AM is also subject to the altitude of the location and the actual thickness of the atmosphere, if to a limited extent.

In general, the overall extinction of the solar irradiance increases with increasing AM, and a qualitative change in the spectrum is observable, the “red shift”, where shorter wavelengths are typically scattered more intensively than longer wavelengths [45]. The AM should not be considered an additional effect that influences the solar irradiance, but rather as an amplifier for the other atmospheric effects mentioned above.

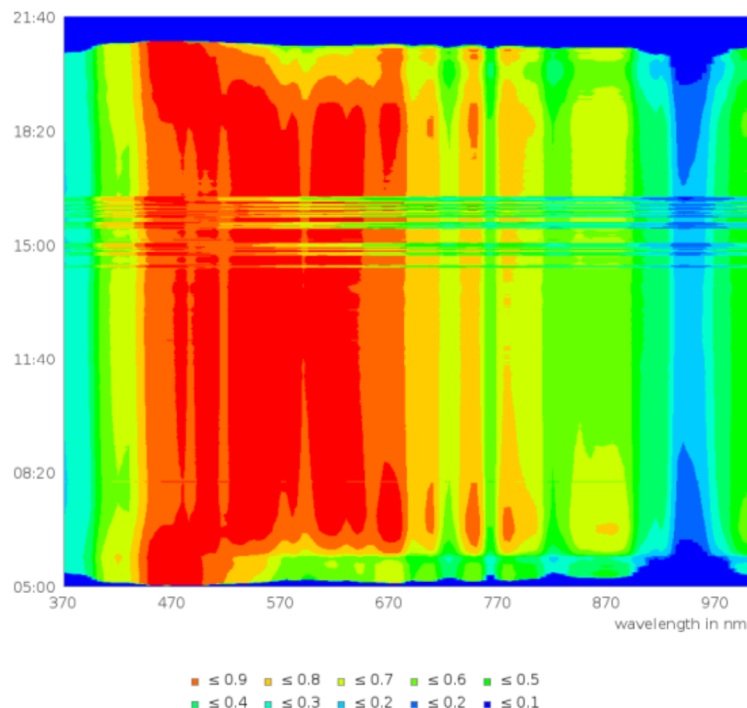


Figure 6. Normalized spectra of the global irradiance in one-minute resolution on July 19, 2014, in Berlin, Germany, from 370 nm to 1000 nm. Each spectrum is normalized to its maximum and color-coded from 0 (blue) to 1 (red). Each recorded spectrum is represented by a horizontal row, starting from sunrise (bottom) to sunset (top of plot). Significant shifts of the spectral composition are observable in the morning and evening around sunrise and sunset, as well as during phases with broken clouds (around 15:00 – 16:00 local time). From [46].

2.3 Irradiance components

This section introduces the most important components of the terrestrial solar irradiance. A schematic illustration is given in Figure 7.

The total of the solar irradiance incident on the Earth’s surface is referred to as the global horizontal irradiance (GHI). When reaching the surface, the GHI features a direct and a diffuse fraction. The direct

horizontal irradiance is the fraction of the total irradiance whose direction was not altered by scattering or reflection. The diffuse horizontal irradiance, in contrast, reaches the surface from various angles, since it results from Rayleigh and Mie scattering of air molecules and particles and from reflection by clouds.

The ratio of the direct and the diffuse irradiance is, as a consequence, dependent on all factors mentioned in the section before.

A third component of the irradiance that is important for PV applications is the ground reflected irradiance. The intensity of it is dependent on the ground reflectivity (albedo), the solar angles and the tilt and orientation angles of the PV system.

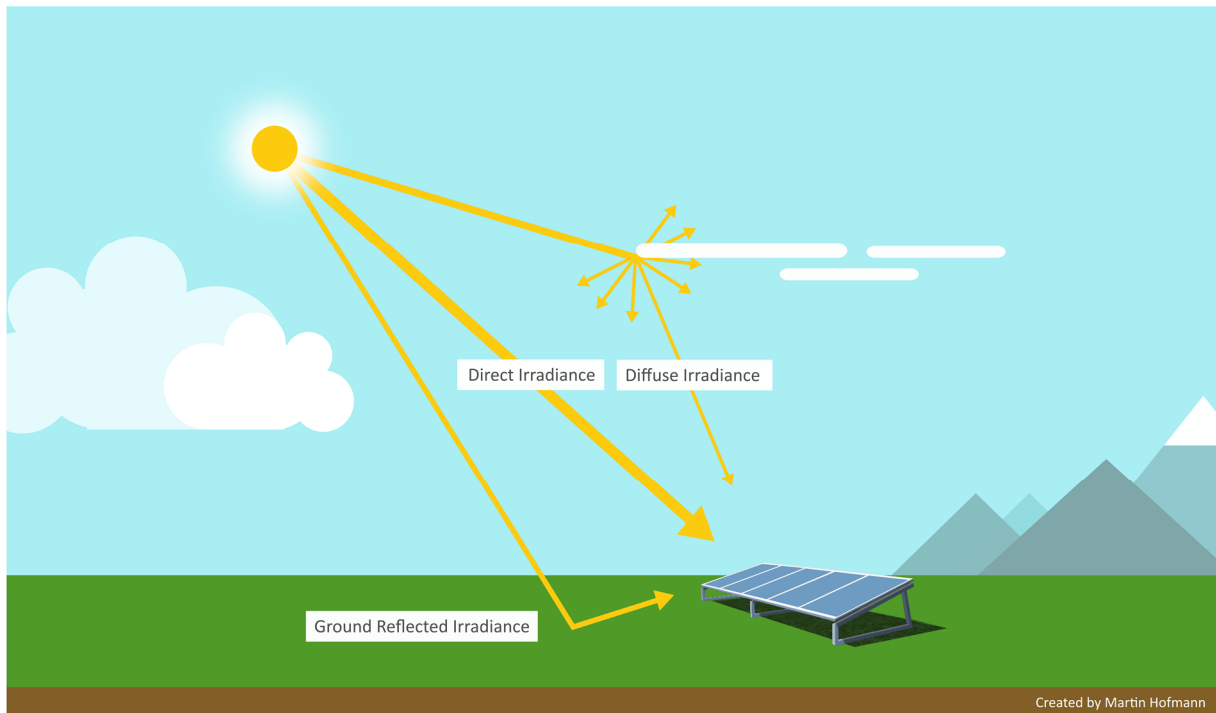


Figure 7. The components of the solar irradiance incident on the tilted plane of a PV system. The direct fraction of the global irradiance reaches the module surface directly. Diffuse irradiance with arbitrary direction is reflected and scattered in the atmosphere (clouds, aerosols, water vapor, etc.) and reaches the module surface from the whole sky dome. Depending on the ground's reflectivity, the solar zenith angle and the tilt angle of the modules, a fraction of the global horizontal irradiance is reflected back upwards and can also reach the module surface as ground reflected irradiance.

2.4 Meteorological modelling for PV system simulations

In this section the most common model chain for PV system simulations is presented. The system borders of the model chains are limited to the electrical output of the PV modules. In full-featured PV system simulations, models for DC/AC inverter efficiency, battery storage and load profiles as well as the interaction with the grid are also part of the model chain.

As displayed in Figure 8 and Figure 9, the model chain can be separated into two logic blocks: The irradiance processor (Figure 8) and the (electrical) PV simulation model chain (Figure 9). The output of the irradiance processor acts as a part of the input of the PV simulation model chain.

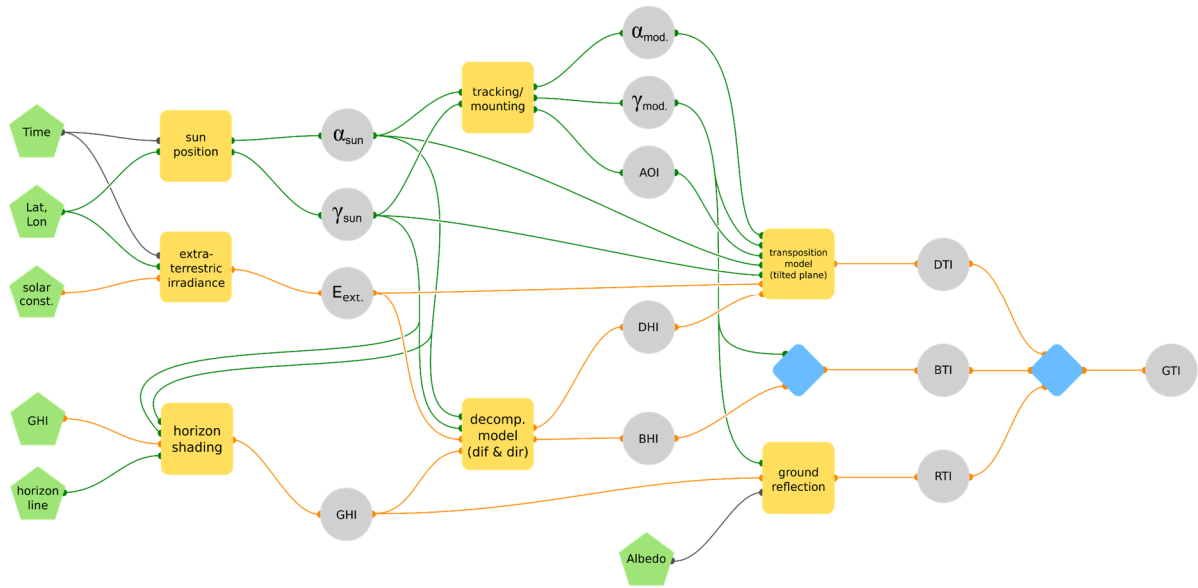


Figure 8. Schema of input data, model chain and output data of the irradiance processor for time-step based solar system simulations.

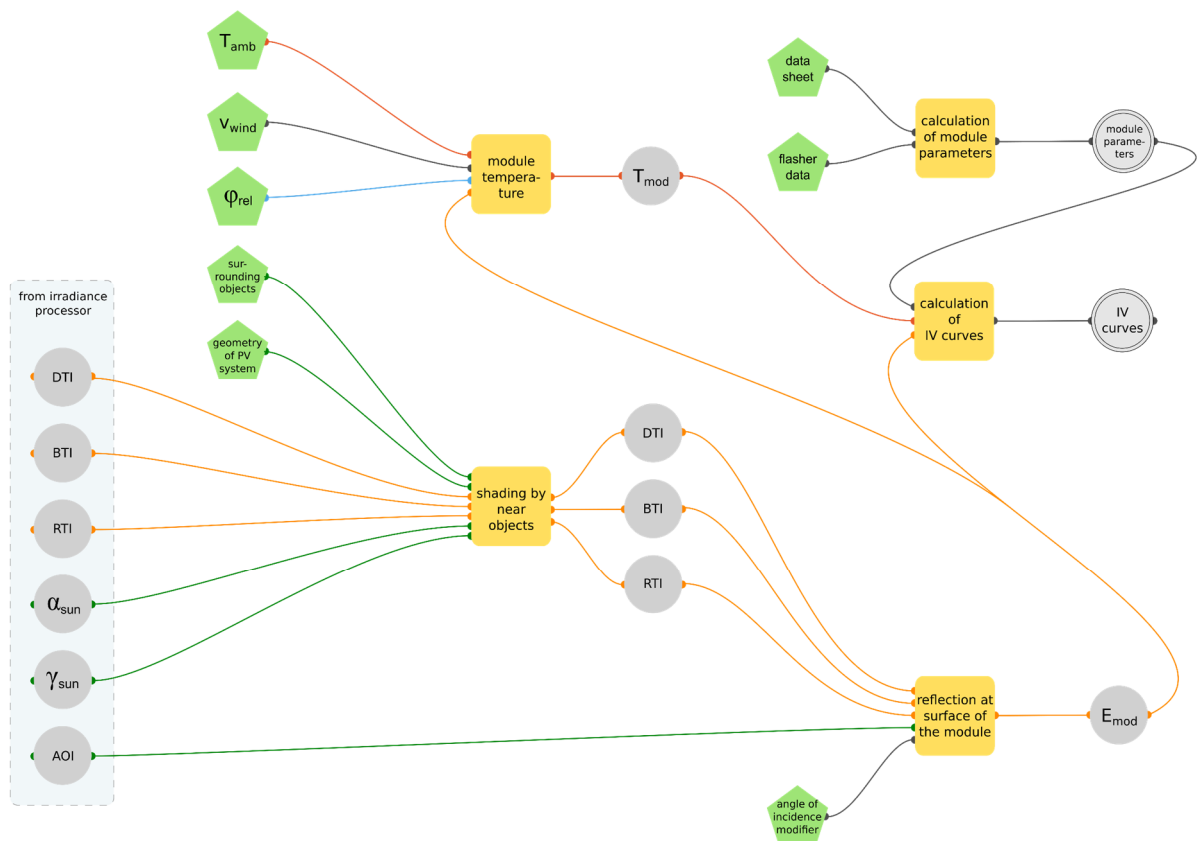


Figure 9. Schema of input data, model chain and output data of the PV simulation model chain. The irradiance input data is the output of the irradiance processor model chain.

From the structure of the model chain it becomes apparent that the main uncertainties are caused by the meteorological input data, i.e. the global horizontal irradiance, and the models used to convert the global horizontal irradiance to the global irradiance on the tilted PV module.

The main steps of the irradiance processor is to decompose the global horizontal irradiance in its direct and diffuse components, to convert the direct and diffuse fraction to the tilted plane, and to estimate the ground reflected irradiance that can additionally reach the module’s surface. For each of these steps there exists a number of models, all of which are subject to uncertainties that can add up or eliminate each other in the course through the model chain. For the direct irradiance the calculation follows geometric relations, but for the diffuse irradiance more complex models are involved. The amount of publications on the topic of solar irradiance decomposition and transposition of diffuse irradiance can be interpreted as an indicator of the complexity of the tasks.

The meteorological input data usually comes in one-hour resolution, e.g. from data providers like Meteonorm [47] or SolarGIS [48] or from satellite data like Heliosat [49] or SARA ed. 2 [50]. The global irradiance however is highly volatile and only roughly represented by hourly averaged values. With these one-hour averages important effects cannot be simulated [51], [52]. Since high quality one-minute measurement data is not available on a global scale with sufficient spatial resolution, there is the need for synthesizing one-minute data from hourly averages.

2.5 The challenge of model validation

One aspect that is important to highlight in the context of simulation models is model validation. The most inherent problem of a number of models and algorithms that have been developed in the past is the limited dataset that they have been validated against. The development of irradiance models that are used in the PV industry started in the 1960, when only few measurements of the solar irradiance were available and also the computational power was in a very early stage of development.

Over the years, both the availability of datasets with hourly resolution and the computational power increased, leading to a wider range of possibilities in model development and validation. Table 2 outlines a short exemplary evolution of the development and validation datasets for selected decomposition models that estimate the diffuse fraction of the global horizontal irradiance. The models listed here are still part of the most well-known and most widely used algorithms today.

Table 2: Evolution of development and validation datasets of well-known diffuse fraction models over time.

Model	Year	Resolution of data	No. of Locations	Covered countries	Time range (in years)
Liu-Jordan [53]	1960	Daily	1	USA	10
Orgill & Hollands [54]	1977	Hourly	1	Canada	5
Skartveit & Olseth [55]	1987	Hourly	3	Norway, Canada	22
Reind [56]	1990	Hourly	6	USA, Denmark, Germany, Spain and Norway	9
Perez [57]	1990	Hourly, partly 15min	13	USA, Switzerland and France	17
Skartveit & Olseth [58]	1998	Hourly	5	Norway, Portugal, UK, France, Sweden	37

A number of enhancements can be observed from the compilation in Table 2. Over time, the number of validation datasets increased, as well as the spread of locations. The resolution developed from daily to 15-minute datasets. Also, the years of measurements available to the model developers increased continuously.

However, the provenance of the data remained Northern America and Europe, covering only a small subset of the multitude of the world’s climate zones. According to the classification by Köppen [59], [60] there is a

total of 29 climate zones around the world, only 10 or 11 of which can be found in Northern America and Europe.

Due to the highly empirical nature of both decomposition and transposition models it is not evident, unfortunately, that a model developed for Northern America or Europe is performing just as well for locations in the other parts of the world. Another consequence of the empirical nature of the models, being developed mostly for hourly averaged input data, is that their application on one-minute time series of global horizontal irradiance data is questionable and demands thorough validation.

Hence, one of the main aspects of my work presented here is the attempt to develop models on a broad basis of high resolution measurement data and to offer validation of existing models against the same data.

2.6 Preparation of the measurement database

2.6.1 Description of the measurement data mainly used in the presented papers

As outlined in the previous section, a main goal of my work consists of the analyses of existing models and the development of new models on a broad basis of high resolution measurements. The Baseline Surface Radiation Network (BSRN) provides an unprecedented publicly available database of WMO quality measurements from 1992 until today [61].



Figure 10. Overview of the measurement stations that form the BSRN, as of 2013.

The BSRN comprises 58 locations worldwide, spread across a high range of latitudes and altitudes, representing a variety of climatic conditions, from arid, desert like regions over tropical climates to

moderate continental climates. Figure 10 gives an overview over the spatial distribution of the locations that are additionally listed in Table 3.

At each location, different meteorological entities are measured: global horizontal irradiance, diffuse horizontal irradiance, direct normal irradiance, ambient temperature, relative humidity, atmospheric pressure etc. The resolution of the data is 60 s for most time series, but also 180 s or 1 h can be found.

Table 3. Complete list of BSRN locations and their three-character labels. Only stations that were part of the snapshot of 2013 are displayed. A complete up-to-date list can be obtained at <https://www.pangaea.de/ddi?request=bsrn/BSRNEvent&format=html&title=BSRN+Stations>

Location	Location Label	Location name	Latitude	Longitude	Elevation
Alert	ALE	Lincoln Sea	82.49	-62.42	127
Alice Springs	ASP	Macdonnell Ranges, Northern Territory, Australia	-23.798	133.888	547
Barrow	BAR	Alaska, USA	71.323	-156.607	8
Bermuda	BER	Bermuda	32.267	-64.667	8
Billings	BIL	Oklahoma, USA	36.605	-97.516	317
Bondville	BON	Illinois, USA	40.0667	-88.3667	213
Boulder	BOU	Colorado, USA	40.05	-105.007	1577
Boulder	BOS	Colorado, USA	40.125	-105.237	1689
Brasilia	BRB	Brasilia City, Distrito Federal, Brazil	-15.601	-47.713	1023
Cabauw	CAB	The Netherlands	51.9711	4.9267	0
Camborne	CAM	United Kingdom	50.2167	-5.3167	88
Carpentras	CAR	France	44.083	5.059	100
Cener	CNR	Spain, Sarriguren, Navarra	42.816	-1.601	471
Chesapeake Light	CLH	North Atlantic Ocean	36.905	-75.713	37
Cocos Island	COC	Cocos (Keeling) Islands	-12.193	96.835	6
Concordia Station, Dome C	DOM	Antarctica	-75.1	123.383	3233
Darwin	DAR	Australia	-12.425	130.891	30
Darwin Met Office	DWN	Australia	-12.424	130.8925	32
De Aar	DAA	South Africa	-30.667	23.993	1287
Desert Rock	DRA	Nevada, USA	36.626	-116.018	1007
Eureka	EUR	Ellesmere Island, Canadian Arctic Archipelago	79.989	-85.9404	85
Florianopolis	FLO	South Atlantic Ocean	-27.605	-48.5227	11
Fort Peck	FPE	Montana, USA	48.3167	-105.1	634
Fukuoka	FUA	Japan	33.5822	130.3764	3
Georg von Neumayer	GVN	Dronning Maud Land, Antarctica	-70.65	-8.25	42
Gobabeb	GOB	Namib Desert, Namibia	-23.561	15.042	407

Goodwin Creek	GCR	Mississippi, USA	34.2547	-89.8729	98
Ilorin	ILO	Nigeria	8.5333	4.5667	350
Ishigakijima	ISH	Japan	24.3367	124.1644	6
Izaña	IZA	Tenerife, Spain	28.3093	-16.4993	2373
Kwajalein	KWA	North Pacific Ocean	8.72	167.731	10
Langley Research Center	LRC	Hampton, Virginia, USA	37.1038	-76.3872	3
Lauder	LAU	New Zealand	-45.045	169.689	350
Lerwick	LER	Shetland Island, UK	60.1389	-1.1847	80
Lindenberg	LIN	Germany	52.21	14.122	125
Minamitorishima	MNM	Minami-Torishima	24.2883	153.9833	7
Momote	MAN	Papua New Guinea	-2.058	147.425	6
Nauru Island	NAU	Nauru	-0.521	166.9167	7
Ny-Ålesund	NYA	Ny-Ålesund, Spitsbergen	78.925	11.93	11
Palaiseau, SIRT Observatory	PAL	France	48.713	2.208	156
Payerne	PAY	Switzerland	46.815	6.944	491
Petrolina	PTR	Brazil	-9.068	-40.319	387
Regina	REG	Canada	50.205	-104.713	578
Rock Springs	PSU	Pennsylvania, USA	40.72	-77.9333	376
Rolim de Moura	RLM	Brazil	-11.582	-61.773	252
Sapporo	SAP	Japan	43.06	141.3286	17
Sede Boqer	SBO	Israel	30.8597	34.7794	500
Sioux Falls	SXF	South Dakota, USA	43.73	-96.62	473
Solar Village	SOV	Saudi Arabia	24.91	46.41	650
South Pole	SPO	Antarctica	-89.983	-24.799	2800
Southern Great Plains	E13	Oklahoma, USA	36.605	-97.485	318
Syowa	SYO	Cosmonaut Sea	-69.005	39.589	18
São Martinho da Serra	SMS	Brazil	-29.443	-53.8231	489
Tamanrasset	TAM	Algeria	22.7903	5.5292	1385
Tateno	TAT	Japan	36.0581	140.1258	25
Tiksi	TIK	Siberia, Russia	71.5862	128.9188	48
Tiruvallur	TIR	India	13.0923	79.9738	36
Toraverre	TOR	Estonia	58.254	26.462	70
Xianghe	XIA	China	39.754	116.962	32

2.6.2 Structure

For this work the snapshot of 2013 was chosen, having undergone quality checks and plausibility routines [62]. The measurement data of the BSRN is available in the form of text files that contain the actual measurement values as well as meta information, e.g. on the used sensors.

In order to facilitate and speed up the data access the BSRN snapshot of 2013 was preprocessed into a high speed versatile MySQL database. The structure of the database is detailed in the following sections.

2.6.2.1 Locations

In the locations table all location specific information is stored. The structure of the table is listed in Table 4. A primary key is set on the ID field that corresponds to the BSRN location labels of Table 3. The values for each location were parsed from the header of the data files. The climate zone according to Köppen [59] was retrieved automatically from the world map by Kottek et al. of 2006 [60]. An example of a table entry is given in Table 5.

Table 4. Structure of the locations table with field names and data types.

#	Field name (<u>key</u>)	Data type
1	<u>ID</u>	varchar(4)
2	Name	varchar(50)
3	Latitude	double
4	Longitude	double
5	Height	float
6	Timezone	float
7	Country	varchar(3)
8	Surface	varchar(25)
9	Topography	varchar(25)
10	Climate	varchar(3)

Table 5. Example entry of the location table.

<u>ID</u>	Name	Latitude	Longitude	Height	Timezone	Country	Surface	Topography	Climate
ASP	Alice Springs	-23.798	133.888	547	9.5	AU	grass	Flat, rural	BWh

2.6.2.2 Entities

All measured entities, i.e. the meteorological measurands like the global horizontal irradiance or the ambient temperature, are stored in the entities table. Its structure is displayed in Table 6 and an example in Table 7.

Table 6. Structure of the entities table with field names and data types.

#	Field name (<u>key</u>)	Data type
1	<u>ID</u>	varchar(4)
2	Name	varchar(100)
3	Unit	varchar(12)
4	Min	double
5	Max	double

Table 7. Example entry of the entities table.

<u>ID</u>	Name	Unit	Min	Max
DIR	Direct radiation	W/m ²	0	2000

2.6.2.3 Devices

Each device that was used for the measurement of an entity is stored in the devices table. The ID is the primary key and corresponds to the WRMC identifier assigned to every sensor [63].

Table 8. Structure of the devices table with field names and data types.

#	Field name (<u>key</u>)	Data type
1	<u>ID</u>	varchar(4)
2	Name	varchar(50)
3	Model	varchar(20)
4	Manufacturer	varchar(50)
5	Serial	varchar(20)

Table 9. Example entry of the devices table.

<u>ID</u>	Name	Model	Manufacturer	Serial
1003	Pyrheliometer	CH1	Kipp & Zonen	940042

2.6.2.4 The mapper

The mapper table is where all other tables are connected. For each unique measurement, one entry is listed in the table, defined by the location, the measured entity, the measurement device, the time resolution and the sensor height. The last two fields contain the names of the tables where the respective measurement values and the list of timestamps of the missing measurements can be found. Table 10 shows the structure of that table, while Table 11 gives an example that follows the examples of the other tables above.

Table 10. Structure of the mapper table that serves as a link between all other tables. The primary key is a combination of the first five fields.

#	Field name (<u>key</u>)	Data type
1	<u>Location</u>	varchar(4)
2	<u>Entity</u>	varchar(12)
3	<u>Device</u>	mediumint(9)
4	<u>Resolution</u>	mediumint(9)
5	<u>Sensorheight</u>	smallint(6)
6	Series	varchar(42)
7	Missing	varchar(42)

Table 11. Example entry of the mapper table. Each entry of this table represents one unique data series.

<u>location</u>	<u>entity</u>	<u>device</u>	<u>resolution</u>	<u>sensorheight</u>	series	missing
ASP	DIR	1003	60	2	ASP_DIR_1003_2_60_Se	ASP_DIR_1003_2_60_Mi

2.6.2.5 The series tables

Finally, the series tables are where the actual measurement time series are stored. The primary key is set on the timestamp, which is expressed as a UNIX timestamp in UTC, without daylight saving time shifting. For each entry in the mapper table there is one series table with the name denoted in the 'series' field of the mapper table.

Table 12. Structure of the series tables.

#	Field name (key)	Data type
1	<u>Timestamp</u>	int(11)
2	Value	float

Table 13. Excerpt of the series table 'ASP_DIR_1003_2_60_Se'

<u>timestamp</u>	value
946681200	1027
946681260	1028
946681320	1029
946681380	1029
946681440	1030
946681500	1032
...	...

2.6.2.6 Overview over the relation of the database

Figure 11 gives an overview of the relation of the database that was generated out of the BSRN dataset. The first five fields of the mapper correspond to dedicated data tables that hold the meta information, but are not part of the actual measurement values. The measurement values are stored in dedicated tables containing nothing but the data series in question, indexed over the timestamp, which provides huge advantages in searches and data access speed.

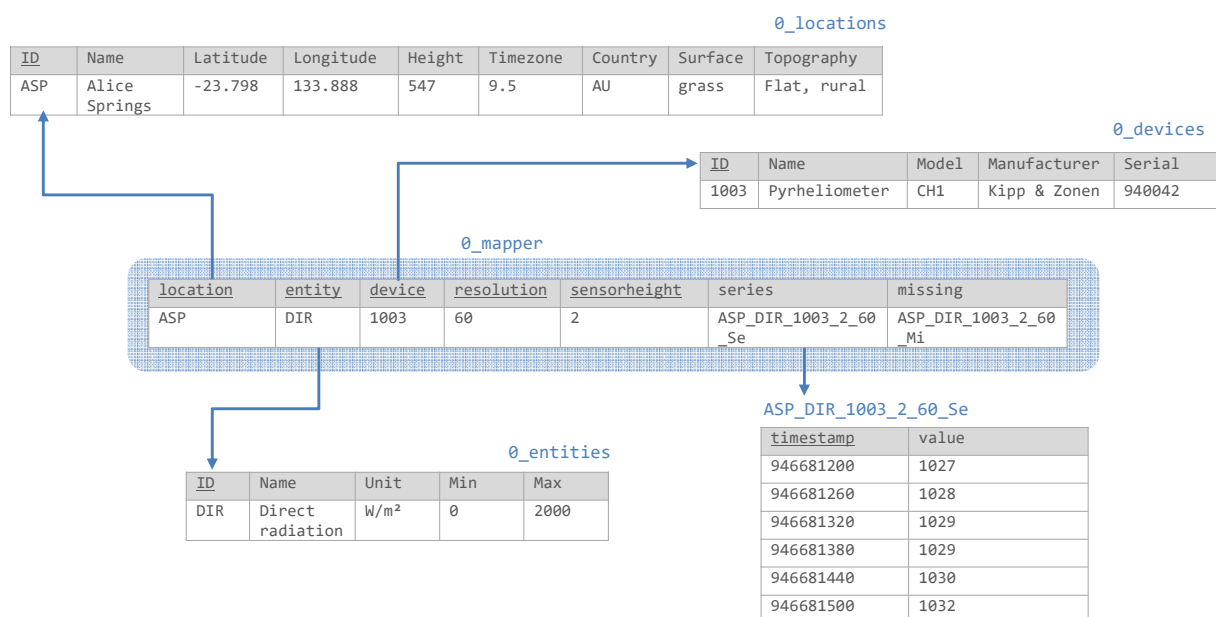


Figure 11. Overview over the relation of the database with example entries.

2.6.3 Queries

In order to illustrate the interaction with the database this section provides some examples of how the data can be accessed depending on the use case. Since the database was set up with MySQL, the query language is SQL.

With the knowledge of the database structure detailed above it is possible to query every thinkable subset of the BSRN data without having to read through the station lists or the meta information in the file headers.

Example 1

Task *“Select all stations that lie between 500 and 700 meters of altitude”*

SQL

```
SELECT * FROM `0_locations` WHERE Height > 500 AND Height < 700
```

Query time 1 ms

ID	Name	Latitude	Longitude	Height	Time zone	Country	Surface	Topography	Climate
ASP	Alice Springs	-23.798	133.888	547	9,5	AU	grass	flat, rural	BWh
FPE	Fort Peck	48.3167	-105.1	634	-7	US	grass	flat, rural	BSk
REG	Regina	50.205	-104.713	578	-6	CA	cultivated	flat, rural	Dfb
SOV	Solar Village	24.91	46.41	650	3	SA	desert, sand	flat, rural	BWh

Example 2

Task *“Show all used pyrhelimeters from Kipp & Zonen”*

SQL

```
SELECT * FROM `0_devices` WHERE Name = 'Pyrheliometer' AND Manufacturer = 'Kipp & Zonen'
```

Query time 5 ms

ID	Name	Model	Manufacturer	Serial
1003	Pyrheliometer	CH1	Kipp & Zonen	940042
1007	Pyrheliometer	CH1	Kipp & Zonen	940059
1010	Pyrheliometer	CHP 1	Kipp & Zonen	100372
53003	Pyrheliometer	CH1	Kipp & Zonen	20283
50006	Pyrheliometer	CH1	Kipp & Zonen	970135
50002	Pyrheliometer	CH1	Kipp & Zonen	950079
10010	Pyrheliometer	CH1	Kipp & Zonen	20189
10016	Pyrheliometer	CH1	Kipp & Zonen	970163
10018	Pyrheliometer	CH1	Kipp & Zonen	20282
10022	Pyrheliometer	CH1	Kipp & Zonen	10257
39016	Pyrheliometer	CH1	Kipp & Zonen	960132
...

Example 3

Task *“Show all measured time series of direct radiation from locations between 500 and 700 meters of altitude that were measured with pyrhelimeters from Kipp & Zonen”*

SQL

```

SELECT a.`series`      FROM `0_mapper` a
      JOIN `0_locations` b ON a.`location` = b.`ID`
      JOIN `0_devices`   c ON a.`device`   = c.`ID`
      JOIN `0_entities`  d ON a.`entity`   = d.`ID`

WHERE ( b.`height` < 700 AND b.`height` > 500)
      AND ( c.`Name` = 'Pyrheliometer' AND c.`Manufacturer` = 'Kipp
& Zonen' )
      AND ( d.`Name` = 'Direct Radiation' )
      AND a.`resolution` > 0

```

Query time 11 ms

Result

series
asp_dir_1003_2_60_se
asp_dir_1007_2_60_se
asp_dir_1010_2_60_se
reg_dir_5003_2_60_se
reg_dir_5004_2_60_se

Example 4

Task *“Show all measurement values from the first result table of example 3 between 2002-07-01 and 2002-08-01”*

SQL

```

SELECT * FROM `asp_dir_1003_2_60_se`
WHERE timestamp >= 1025481600 AND timestamp <= 1028160000
ORDER BY timestamp ASC

```

Query time 1 ms

Result

Timestamp	value
1025481600	800
1025481660	800
1025481720	807
1025481780	813
1025481840	816
1025481900	818
1025481960	820
1025482020	822
...	...

Note: It is possible to express the table name in example 4 with a slight modification of the SQL in example 3, so that the query would be comparable to *“Show all measurement values between 2002-07-01 and 2002-08-01 from the first direct irradiance data series measured by a Kipp & Zonen pyrheliometer, where the location lies between 500 and 700 m.”* In order to achieve that, the table name in example 4 would be replaced by the SQL code of example 3, with adding a `LIMIT 1` to the query.

2.6.4 Advantages of the database design

Nearly unlimited amounts of data series can be processed with this approach, which is only really limited by the available disc space. While this also holds true for any other database structure, databases that follow

a conventional table structure with a column for each sensor and a row for each timestamp suffer from significant performance issues during the insertion of new entries or the retrieval of a subset of the data.

In the approach presented above, the structure of the database follows the logic structure of the BSRN data, which makes it easily understandable and accessible. Arbitrary subsets of the whole dataset are selectable without the loss of performance. The indexing of the timestamp fields also makes it possible to search for any given point in time or time range very rapidly.

Another advantage that is mostly important for the performance of the data processing is that the measurement values are stored in a predefined data type. The database knows that a measurement value is of a floating point number, which means that no parsing (converting text to a number the computer can calculate with) is needed like it would when using text files.

Additionally, the database can be connected to any known programming language like C# or PHP, or computing environment like Matlab or IDL.

The design of a database should always fit the most frequent queries that are to be expected from the intended use case. In irradiance modelling and validation, one of the most common scenarios is to get continuous time series of the global horizontal irradiance from a specific location in a given range of time.

So as an example the query would be to get all measurement values of the global horizontal irradiance measured in Lindenberg, Germany, between 1995 and 2007. Since this covers a large time span, multiple pyranometers were used during that time. In total the result comprises 6.3 million data points, while it takes only 2.8 seconds to fetch them on an ordinary laptop. Figure 12 illustrates the result of the data query.

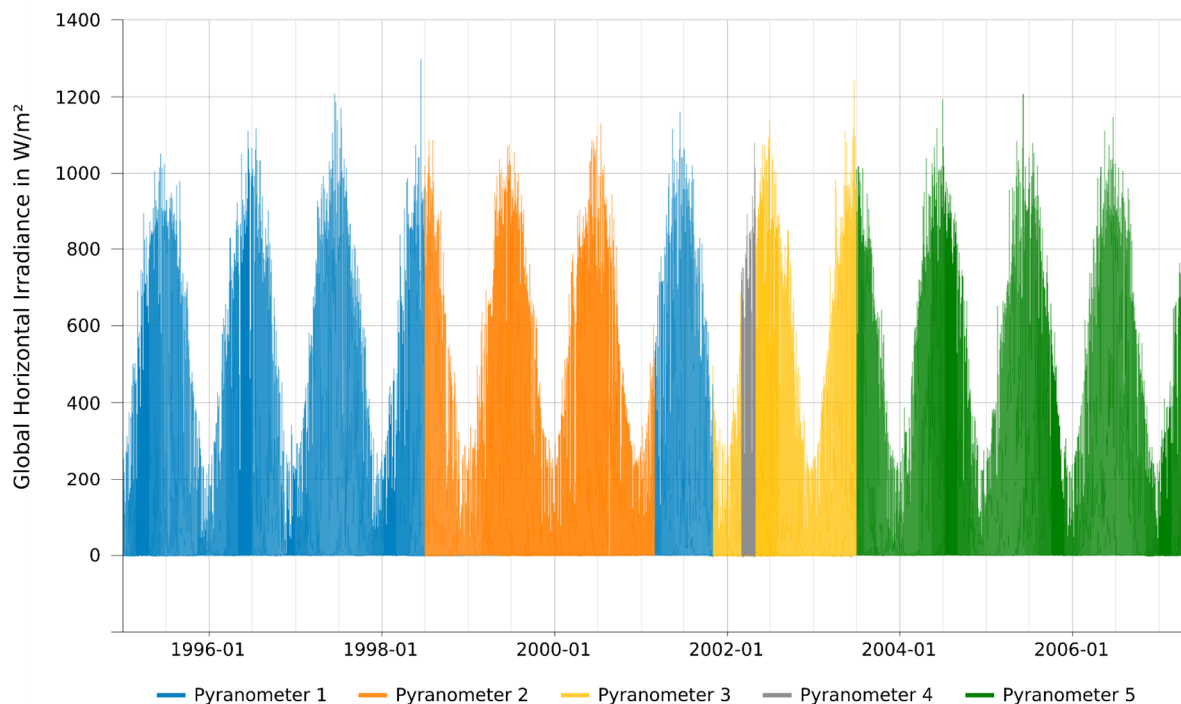


Figure 12. Measurements of global horizontal irradiance in one-minute resolution, from 1995 to 2007, from Lindenberg, Germany. The dataset comprises five series, since five different pyranometers were used. The data retrieval takes under 3 seconds on an ordinary computer.

With this database concept it is easily possible to process a high amount of measurement data for the use of model validation or the creation of new algorithms.

3 Peer-reviewed publications and their context

3.1 Synthesis of one-minute time series from one-hour data

With the development of PV technology and the increase of its market share over the past decades, the requirements for the quality of the energy yield simulations increased. In the beginning, yield estimations and irradiance models were based on meteorological input data with time steps of a day or even a month [64], [65], [66], [67]. First approaches followed that enabled researchers and modelers to synthesize time series with a time resolution of a day from monthly averages [68].

Then daily values were more widely available, and with the ever increasing quality requirements and scientific progress, models emerged to synthesize time series of one-hour resolution [69], [70], [71], [72]. Nowadays, hourly data is widely available thanks to a higher number of meteorological stations and satellite-derived measurement data that cover the whole surface of the Earth. High quality measurement data of higher time resolution is still scarce and thus the community faces the need to synthesize time series with one-minute resolution from hourly data. The most common commercial data provider tool in Europe, Meteonorm, featured two algorithms to synthesize one-minute values: Aguiar [70] and Skartveit [72], both of which have not been developed for the synthesis of one-minute data in the first place.

In the presented paper, these approaches were analyzed and found to be of insufficient quality for PV simulations. A new approach was developed that is based on one-minute measurement data from BSRN and uses precompiled transition probability matrices and Markov chains.

The approach produces time series of global irradiance of one minute resolution with substantially more natural features compared to the two existing models. The validation shows that the frequency distributions of the global irradiance, the irradiance gradients and the clear-sky index of the new algorithm are significantly closer to their natural ideals than the ones produced by the other algorithms. The root mean squared error (RMSE) of the global irradiance distribution is reduced by 61%, the RMSE of the irradiance gradients by 52% and the RMSE of the clear-sky index by 71%.

As of June 2017 the newly developed model is also part of Meteonorm.

Since it is a complex and time consuming task to implement the algorithm, it is publicly available for researchers on <http://www.pvmodelling.org>.

Research Article

Improved Synthesis of Global Irradiance with One-Minute Resolution for PV System Simulations

**Martin Hofmann,¹ Stefan Riechelmann,² Cristian Crisosto,²
Riyad Mubarak,² and Gunther Seckmeyer²**

¹ *Valentin Software GmbH, Stralauer Platz 34, 10243 Berlin, Germany*

² *Institute for Meteorology and Climatology, University Hannover, Herrenhäuser Straße 2, 30419 Hannover, Germany*

Correspondence should be addressed to Martin Hofmann; martin.hofmann@valentin-software.com

Received 6 August 2014; Revised 3 November 2014; Accepted 4 November 2014; Published 26 November

Academic Editor: Pramod H. Borse

Copyright © 2014 Martin Hofmann et al. This is an open access article distributed under the Creative Commons Attribution License, which permits unrestricted use, distribution, and reproduction in any medium, provided the original work is properly cited.

High resolution global irradiance time series are needed for accurate simulations of photovoltaic (PV) systems, since the typical volatile PV power output induced by fast irradiance changes cannot be simulated properly with commonly available hourly averages of global irradiance. We present a two-step algorithm that is capable of synthesizing one-minute global irradiance time series based on hourly averaged datasets. The algorithm is initialized by deriving characteristic transition probability matrices (TPM) for different weather conditions (cloudless, broken clouds and overcast) from a large number of high resolution measurements. Once initialized, the algorithm is location-independent and capable of synthesizing one-minute values based on hourly averaged global irradiance of any desired location. The one-minute time series are derived by discrete-time Markov chains based on a TPM that matches the weather condition of the input dataset. One-minute time series generated with the presented algorithm are compared with measured high resolution data and show a better agreement compared to two existing synthesizing algorithms in terms of temporal variability and characteristic frequency distributions of global irradiance and clearness index values. A comparison based on measurements performed in Lindenberg, Germany, and Carpentras, France, shows a reduction of the frequency distribution root mean square errors of more than 60% compared to the two existing synthesizing algorithms.

1. Introduction

The efficiency of PV modules depends mainly on the irradiance, amongst other secondary effects such as module temperature [1, 2]. The nonlinear dependency of the module efficiency on the irradiance and the influence of temperature on the module efficiency require simulations with a high temporal resolution.

For the understanding of the dynamic interaction of PV generator, storage systems, loads, and grids on a worldwide scale, one-minute data series of high quality in terms of realistic variability and frequency distributions are a key factor. Simulating those systems with hourly averaged values neglects significant behavior patterns like short time power enhancements [3].

To illustrate the importance of one-minute data for the simulation of PV systems, a 1 kWp PV example system with

PV generator, DC/AC inverter, and grid is analyzed at the location of HTW Berlin, Germany. DC/AC inverters are used in grid-connected PV systems as power processing interface between the PV power source (DC) and the electric grid (AC). The output power is very sensitive to the temporal variability of the solar radiation which is highest during broken clouds.

In some important markets (e.g., Germany), PV systems can be affected by grid connection restrictions that define the maximum AC power output of the inverter as a percentage of the installed PV power on the DC side, where the usual limit is around 70% [4]. In Figure 1 the power output of the PV example system is shown in a one-minute temporal resolution (grey) and in an hourly averaged temporal resolution (blue) for a day with broken clouds. An energy yield loss of 7% is calculated when the 70% restriction is applied to the hourly averaged power output. When applying the restriction to the

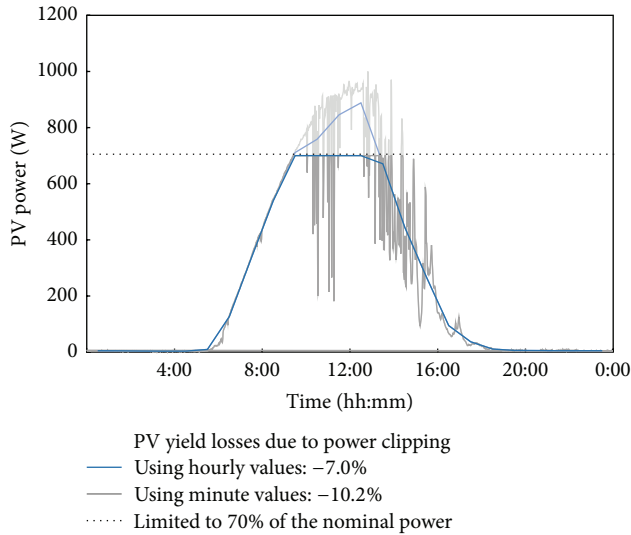


FIGURE 1: Power output of a 1kWp PV system at HTW Berlin, Germany, on April 01, 2012, measured one-minute values (grey) and hourly averaged values (blue). The yield losses due to maximum power clipping (output power is cut above 700 W) are calculated.

one-minute power output values, an energy yield loss of 10% is calculated.

Following Vanicek et al. in his contribution on the energy yield losses as a function of inverter dimensioning [3], we analyzed the dependency of energy yield losses due to maximum power clipping for PV inverters. Figure 2 shows that these losses are dependent on the inverter sizing factor as well and increase significantly when using one-minute instead of hourly averaged time series. In sum, energy losses due to inverter undersizing and maximum power clipping add up to a constant value within the inverter dimensioning range until the reciprocal of the power clipping value is reached (143%). This threshold marks the optimum inverter sizing factor for PV inverters with maximum power clipping, since losses will not decrease when using a larger inverter. With hourly averaged values (grey), the total energy loss is at 1.3% while the more precise simulation with one-minute values (blue) returns a total energy loss of 3.9%. These examples indicate that the use of hourly averaged irradiance datasets can result in falsified yield predictions.

While there exist several commercial providers and free sources of meteorological data in a resolution of one hour (e.g., Meteotest, SolarGIS, and TMY), covering nearly the whole earth, the availability of measured irradiance data with a resolution of less than an hour is very limited. This limited availability leads to the necessity to synthesize one-minute time series from hourly averaged data.

Several algorithms were developed in the past in order to synthesize one-minute global irradiance datasets with realistic variability and frequency distributions from hourly averaged datasets. The supposedly most established algorithms were developed by Aguiar and Collares-Pereira [5, 6], Skartveit and Olseth [7], and Glasbey [8]. Like many similar algorithms, the aim of those approaches is the reproduction

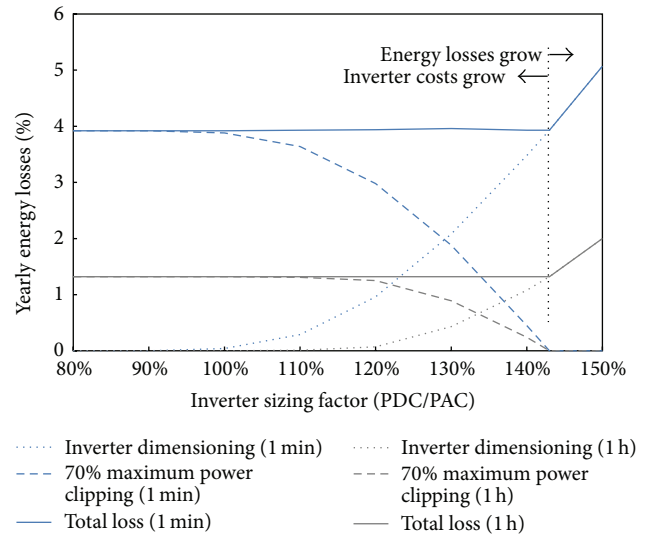


FIGURE 2: Yearly energy yield losses of a 1kWp PV system at HTW Berlin, Germany, for various inverter sizing factors (the relation between installed PV power on the DC side and nominal AC inverter output) and a maximum power clipping value of 70% (output power is cut at 70% of the installed DC power). Using hourly averaged values for the simulation of PV systems leads to a significant underestimation of the yearly yield losses. With hourly averaged values (grey), the total energy loss is at 1.3% while the more precise simulation with one-minute values (blue) returns a total energy loss of 3.9%. In addition, this figure illustrates that the optimal inverter sizing factor (here, 143%) for systems with maximum power clipping is the reciprocal of the clipping value (70%).

of the characteristic frequency distributions of the solar irradiance or the clearness index k_t , which is a measure for atmospheric transmission.

The contribution of Aguiar and Collares-Pereira was originally designed for the generation of hourly averaged time series with daily averages as input. It is based on the modeling of probability densities as Gaussian functions that depend on the clearness index k_t . Skartveit and Olseth focused on the modeling of frequency distributions of global and direct irradiance, depending on intrahour and interhour irradiance variability, while using first-order autocorrelation for the generation of the actual time series. Glasbey proposed nonlinear autoregressive time series generation with joint marginal distributions as multivariate Gaussian mixtures. The estimation of probability density distributions of the irradiance has recently been investigated by Voskresbenzev et al. [9].

Other important contributions to this topic were provided by Assunção et al. [10] with investigations on the dependency of k_t from the air mass and by Tovar et al. [11] with the analysis of the relation of hourly averaged [clearness indices] to one-minute clearness indices.

However, current algorithms only insufficiently withstand the validation against measurement values, since they underestimate irradiance enhancements caused by broken

clouds, overestimate mid irradiance values, and provide one-minute time series with a variability that is too high.

Therefore, we developed an improved algorithm capable of synthesizing one-minute global irradiance time series based on hourly averaged global irradiance. The algorithm takes three different weather conditions (cloudless, broken clouds and overcast) into consideration. We show that the improved algorithm exceeds the performance of the Aguiar and the Skartveit algorithm in terms of temporal variability and characteristic frequency distributions for the calculation of short-term global irradiance at two exemplary PV installation locations.

2. Measurement Data and Methodology

The new algorithm consists of two parts. The first part comprises a data preparation process that categorizes the input dataset and produces transition probability matrices (TPM) for three weather conditions: cloudless, broken clouds and overcast. The preparation process has to be executed only once.

The input dataset used for the initialization consists of global irradiance measurements conducted by the Baseline Surface Radiation Network (BSRN), featuring more than 50 locations all over the world with up to 20 years of measurements. The BSRN database is updated continuously with new measurement data; in this study we used a snapshot of May 2013. A subset of these data, one-minute global irradiance measurements performed in Lindenberg, Germany (2005), and Carpentras, France (2001), is used for the model validation.

The second part is the synthesis process for one-minute time series from hourly averaged time series. The required input of this process only consists of the prepared set of TPM and the hourly averaged time series of global irradiance that is to be disaggregated. The core of the process is based on Markov chains [12, 13], utilized in a similar way by McCracken [14].

The central idea in both parts of the new algorithm is the classification of weather situations by the temporal feature of the clearness index. In the first part, the preparation process, the BSRN dataset is split into three individual datasets corresponding to three weather conditions: cloudless, broken clouds and overcast. Each subset is then processed separately and transformed into a transition probability matrix. In the second part, the synthesis process, each daily dataset of the hourly averaged input values is categorized as well and processed according to their weather category. As a consequence, the main process steps of the new algorithm are only depending on those weather categories, in disregard of specific location information.

This leads to the advantage that the algorithm can be applied to hourly averaged datasets of arbitrary locations. Furthermore, the only required input is the hourly averaged datasets, once the TPM are created. Hence, the new algorithm combines aspects of existing work on this subject with a universally applicable method for the synthesis of one-minute time series from hourly averaged values.

2.1. Classification of Weather Condition by the Clearness Index.

The determination of predominant weather conditions is needed in both steps of the presented algorithm. The weather conditions are determined by the calculation of the clearness index k_t . The clearness index is defined as the ratio of measured global irradiance E_{measured} at Earth's surface and the irradiance calculated for cloudless conditions at the particular measuring site, denoted by clear sky irradiance E_{clear} :

$$k_t = \frac{E_{\text{measured}}}{E_{\text{clear}}}. \quad (1)$$

The calculation of the clear sky irradiance has a significant influence on the k_t index. A modification of Bourges' calculation [15] is used in this work, since it provided the best results for all analyzed locations:

$$E_{\text{clear}} = 0.78 E_{\text{ext}} \sin(\gamma_S)^{1.15}, \quad (2)$$

where γ_S is the elevation of the sun and E_{ext} is the extraterrestrial irradiance. The extraterrestrial irradiance E_{ext} was calculated using Maxwell's approach [16], whereas the elevation of the sun γ_S was modelled by the algorithm of Reda and Andreas [17] from NREL.

The predominant weather condition on a particular day results in a characteristic temporal pattern of k_t that can be used to categorize the day into one of the three classes. The detection algorithm of the weather condition is based on the daily average of hourly averaged k_t values $\bar{k}_{t,\text{day}}$ and the variability during a day $\tilde{k}_{t,\text{day}}$:

$$\bar{k}_{t,\text{day}} = \frac{1}{n} \sum_{i=1}^{24} k_{t,i}, \quad \tilde{k}_{t,\text{day}} = \frac{1}{n} \sum_{i=2}^{24} |k_{t,i} - k_{t,i-1}|, \quad (3)$$

where n is the number of hours where global and clear sky irradiance is above 0 W/m^2 .

Table 1 gives an overview about the three weather classes and their detection conditions. An example for the classification is shown in Figure 3 for some days in August 2005 in Lindenberg, Germany. For a better visualization we fall back on one-minute values here, whereas it is to be noted that the detection is based on hourly averaged values of the clearness index k_t , because these values form the input of the synthesis algorithm. The classification conditions are visualized as well in Figure 4 for an example dataset of Lindenberg, Germany.

2.2. Transition Probability Matrices.

For each class that represents a specific weather situation, matrices of transition probabilities (TPM) are created. The TPM contain information on how probable the switch is from one specific k_t at time i to another value at the time $i + 1$. To create those matrices, diurnal courses of measured one-minute values of equal weather class, independent of their location, are analyzed and converted into a common matrix. The frequency of every possible transition in the measured data is registered and afterwards normalized to obtain the transition probabilities. Therefore, a TPM contains all probabilities of the change of

TABLE 1: Overview of the three weather classes and their detection conditions.

Weather class	Condition
Overcast	$0.6 - \bar{k}_{t,\text{day}} > \bar{k}_{t,\text{day}}$
Cloudless	$-0.72 + 0.8\bar{k}_{t,\text{day}} \geq \bar{k}_{t,\text{day}}$
Broken clouds	Otherwise

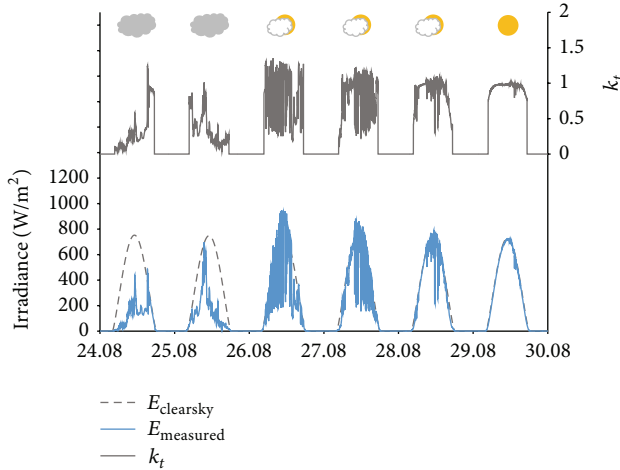


FIGURE 3: Example results of the weather category detection algorithm based on k_t patterns for 6 subsequent days from 24.08.2005 to 30.08.2005 in Lindenberg. Clear sky irradiance (dotted grey) and the clearness index (grey line on top) in comparison to the measured global irradiance (blue line, bottom). Visualization is done with one-minute values whereas the detection is based on hourly averaged values.

a specific value of $k_{t,i}$ to $k_{t,i+1}$ from one minute to the next under a specific weather condition. An example for a TPM of broken clouds weather condition is given in Table 2. In this case, the probability of k_t to change from 0.1 to 0.09 during one minute is 17.6%, the probability to stay the same is 53.2%, and the probability to change from 0.1 to 0.01 is 0%.

The excerpt of a TPM shown in Table 2 is an example of how such transition probability matrices are structured. The actual values of the TPM however are subject to the underlying dataset that is used to create those matrices. In this study we will use different subsets of the BSRN databases for the creation process, depending on the dataset we use for validation. The validation dataset is omitted from the dataset for the TPM creation process to avoid self-reference. Hence, the resulting values in the matrices may vary, whereas the presented method to create the matrices is universal. For this reason we refrain from listing all 200×200 TPM in this study.

Since the TPM are created using real weather data in one-minute resolution, each measured irradiance within a given time interval leaves a fingerprint in a TPM. Hence, the spatial and temporal validity of the algorithm is increasing with the number of input datasets. As of May 2013, the BSRN comprises more than 6900 irradiance measurement months distributed globally, which is equal to more than 200 000 measurement days in one-minute resolution that leave their fingerprint in the TPM. The influence of the number of input

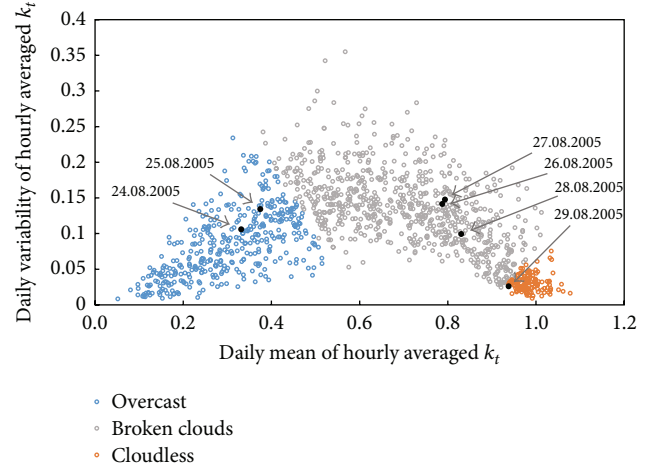


FIGURE 4: Visualization of the classification of weather conditions by k_t patterns using measurement values from Lindenberg, Germany. Cloudless days feature high daily means $\bar{k}_{t,\text{day}}$ with only little daily variability $\bar{k}_{t,\text{day}}$. Days with overcast sky can be characterized by low daily means and low to mid variability. Days with broken clouds feature a high daily variability and mid to high daily means. The black points refer to the example days of Figure 3.

data on the synthesis quality is referred to in Results section as well.

2.3. *Generation of k_t Sequences with Markov Chains.* To generate one-minute values from hourly averaged sequences of the global irradiance, the weather condition of the day in question is detected at first. Depending on the weather condition the correspondent k_t -TPM is chosen.

The actual generation of the one-minute values is conducted with the help of the so-called discrete-time Markov chains (DTMC). DTMC is a state-based process for the modelling of real-world events. In the first order, the process is memory-less, so that the next state only depends on the current state [12, 13].

To determine the successor $k_{t,i+1}$ of a specific k_t value $k_{t,i}$ at a given point in time i , the probabilities belonging to $k_{t,i}$ are cumulated. Then, a Markov number between 0 and 1 is generated and inserted as a threshold value into the cumulated probability function. The point at which the probability function is bigger than the Markov number for the first time is defined as $k_{t,i+1}$. The process continues in the same manner and generates a chain of 60 k_t values per hour. From these k_t sequences, the global irradiance for every point in time can be calculated with the help of the clear sky irradiance:

$$E_{\text{generated},i} = k_{t,i} \cdot E_{\text{clear sky},i} \quad (4)$$

This process is repeated until the mean value of the generated one-minute values equals the hourly averaged input value

TABLE 2: Excerpt of an example TPM for broken clouds weather condition. For each k_t value at time i (rows), the probability of a switch to another k_t at time $i + 1$ (columns) is given. The k_t values range from 0 to 2.

$k_{t,i}$	$k_{t,i+1}$											
	0	0.01	0.02	0.03	0.04	0.05	0.06	0.07	0.08	0.09	0.1	...
0	0	0	0	0	0	0	0	0	0	0	0	0
0.01	0	0.82927	0.17073	0	0	0	0	0	0	0	0	0
0.02	0	0.10345	0.72414	0.17241	0	0	0	0	0	0	0	0
0.03	0	0	0.06897	0.76724	0.15517	0	0.00862	0	0	0	0	0
0.04	0	0	0.00709	0.12057	0.70922	0.14894	0.01418	0	0	0	0	0
0.05	0	0	0	0	0.07004	0.75875	0.15564	0.01167	0.00389	0	0	0
0.06	0	0	0	0	0.01136	0.14773	0.64394	0.14773	0.03788	0.00758	0.00379	0
0.07	0	0	0	0	0	0.0084	0.19328	0.53361	0.2395	0.02521	0	0
0.08	0	0	0	0	0.0059	0	0.0236	0.17109	0.57817	0.17404	0.03245	0
0.09	0	0	0	0	0	0	0	0.03378	0.19932	0.46959	0.21284	0
0.1	0	0	0	0	0	0	0	0	0.02067	0.17571	0.5323	0
...												

E_{hour} with desired accuracy δ . If necessary, the values are scaled as well:

$$\left| \frac{E_{\text{hour}}}{\sum_{i=1}^{60} E_{\text{generated},i}} - 1 \right| < \delta, \quad (5)$$

$$E_{\text{gen., scaled},i} = \frac{E_{\text{hour}}}{\sum_{m=1}^{60} E_{\text{generated},m}} E_{\text{generated},i}.$$

3. Results

In the following section the new algorithm is validated with measurement data and compared to the algorithms by Aguiar and Skartveit. The result comparison is conducted for two exemplary datasets of one year at two different locations: Lindenberg, Germany, 2005, and Carpentras, France, 2001. Both datasets are taken from the BSRN database. To avoid self-reference in the presented results, the creation process of the TPM excludes all measurement data of the respective location.

First, the results are presented on the basis of diurnal courses to assess the temporal variability, afterwards in the form of frequency distributions. In addition we provide a table with comparative uncertainties.

When assessing the temporal variability of synthesized one-minute values, the results for days with broken clouds and overcast skies are more important, since the simulation of sunny days is not difficult. In Figure 5 the measured course of the global irradiance (black (a)) is displayed in comparison to the temporal course of the values generated with the new algorithm (blue (b)) and the algorithms by Aguiar (c) and Skartveit (d) for an overcast day.

Although the exact occurrence of irradiance peaks in the modelled time series may differ from the measured time series, the variability of the values modelled with the new algorithm agrees with measured values to a very high degree. The mean variability of irradiance changes from one minute to the next is 7.0 W/m^2 for measured time series, whereas it is 8.2 W/m^2 for the data modelled with the new algorithm

in the example dataset of Figure 5. With n being the number of minutes of a day (1440), the mean variability of the global irradiance is calculated as follows:

$$\overline{E_{\text{var}}} = \frac{1}{n} \sum_{i=2}^n |E_i - E_{i-1}|. \quad (6)$$

The methods of Aguiar and Skartveit lead to higher mean variability values of 13.1 W/m^2 and 16.6 W/m^2 , respectively. Scientists of the Sandia National Laboratories as well refrain from using these algorithms for this reason:

Without an adequate method to account for auto-correlations (of relatively high order) in the one-minute time series of clearness index, simulations using these distribution forms would likely prove too variable, as we found for simulations using Glasbey's model, and as we suspect would have resulted using the model of Skartveit and Olseth [18].

A more complete picture of the variability of solar irradiance can be obtained by analyzing the frequency of its gradients over a whole year. The gradients, in this case the absolute difference of the irradiance values of one minute to the next for the measured data and model data, are calculated and transferred into frequency plots. Figure 6 shows the frequency of irradiance gradients for Lindenberg, 2005, whereas the data for Carpentras, 2001, is displayed in Figure 7.

In both cases, the frequency distribution of the data modelled by the algorithms of Aguiar and Skartveit, respectively, shows significant overestimations for the gradient range from 10 to 100 W/m^2 , while the new algorithm is able to produce irradiance values that feature a similar frequency distribution in this range. For gradients of less than 10 W/m^2 the data modelled by all algorithms show similar deviations from the measured data. For gradients of more than 100 W/m^2 , the new algorithm and the approach of Skartveit display similar

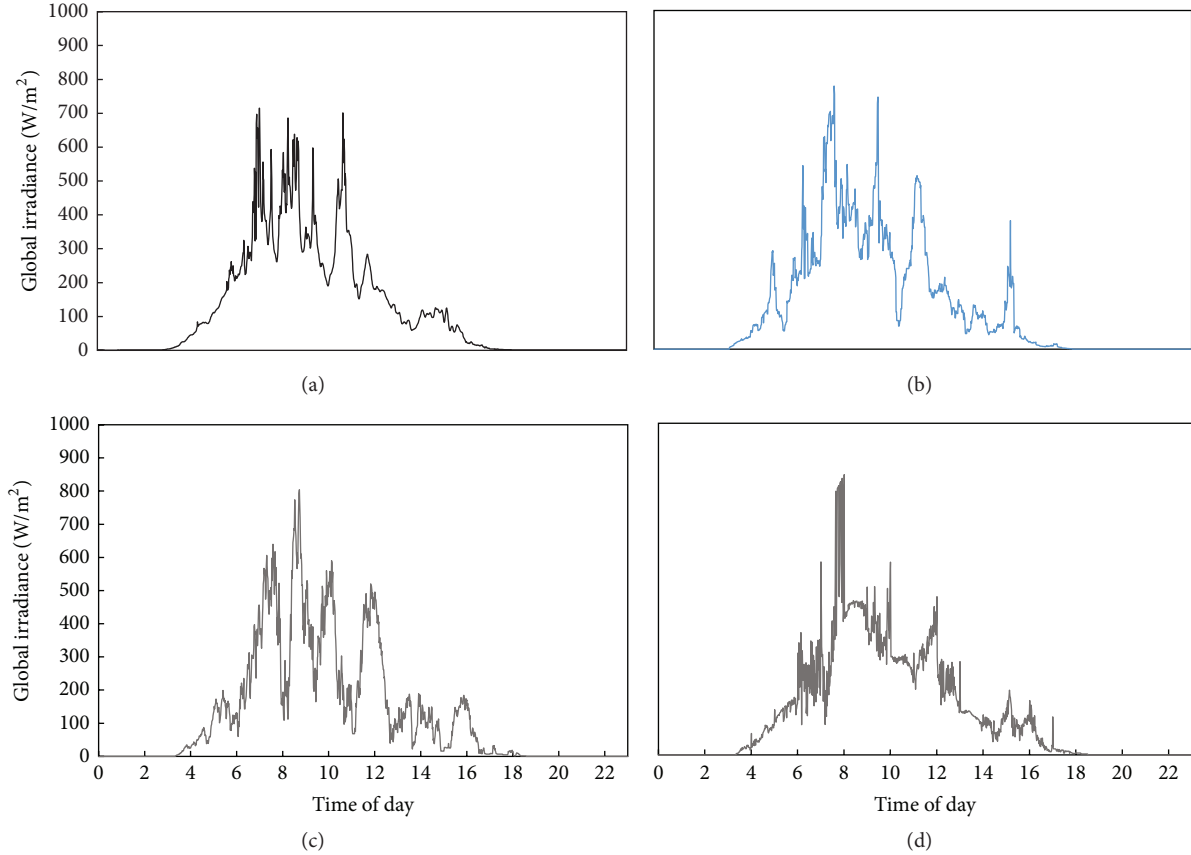


FIGURE 5: Lindenberg, May 14, 2005. The temporal course of the measured global irradiance (a) on a day that was rated as a day with overcast sky is compared to values generated by the new algorithm (b), the algorithm by Aguiar (c), and the algorithm by Skartveit (d). The mean variability, that is, the mean irradiance change from one minute to the next, of the measured irradiance of 7.0 W/m^2 shows good congruence with the new algorithm (8.2 W/m^2), while the usage of the algorithms by Aguiar and Skartveit leads to higher variability values of 13.1 W/m^2 and 16.6 W/m^2 .

quality, whereas the algorithm of Aguiar shows significant underestimations for both locations.

For the transfer into deviation indicators, the deviations of the modelled data from the measured ones for each irradiance value are squared, weighed by its frequency, and summed up. The frequency weight f_i is added in order to obtain information about the energetic relevance of each irradiance gradient. For the calculation of root mean square errors, these sums are then divided by the number of gradient steps and the square root is applied. Table 3 shows the results for all three analyzed models. In accordance with the visual impression of the frequency plots in Figures 6 and 7, the RMSE values for the new model presented in this study are significantly smaller than the RMSE values of the other two models by Aguiar and Skartveit:

$$\text{RMSE} = \sqrt{\frac{1}{n} \sum_{i=1}^n (f_i (x_{\text{Model},i} - x_{\text{Measurement},i}))^2}. \quad (7)$$

Since the frequency distributions of the global irradiance and the k_t values are more reliable indicators for the applicability to simulations of photovoltaic systems, they are displayed

TABLE 3: Root mean square errors (RMSE) of the frequency distributions of irradiance gradients of modelled data versus measurement in W/m^2 . The new model is able to produce significantly smaller values of RMSE than the models of Aguiar and Skartveit for both locations, Lindenberg, 2005, and Carpentras, 2001.

Model	Lindenberg	Carpentras
Aguiar	8131	8541
Skartveit	4758	5112
New	2787	3218

in Figures 8, 9, 10, and 11. Measured values (black) are compared to values calculated by the conventional algorithms by Aguiar and Skartveit (grey dotted and solid), as well as to the new algorithm presented in this study (blue). Each of these distributions is calculated from values of one whole year.

For the generation of those figures, measured one-minute values were averaged to hourly means, which were then fractionized again using the new improved algorithm as

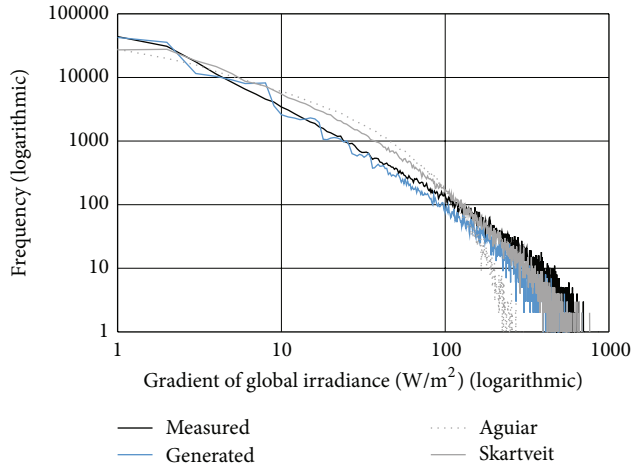


FIGURE 6: Frequency of gradients of the global irradiance in Lindenberg, Germany (2005). The model quality in lower gradient ranges of up to 10 W/m^2 is similar in all models. In the range of 10 to 100 W/m^2 , significant deviations can be detected for the models of Aguiar and Skartveit (grey), whereas the new method (blue) shows good congruence. For gradient values of more than 100 W/m^2 , the model of Aguiar underestimates the frequency significantly, while the new method and the method of Skartveit feature similar frequency values compared to the measurement data (black).

well as the approaches of Aguiar and Skartveit. The figures show how often a specific irradiance value occurs in a year. The maximum at high irradiance values represents clear sky situations, while the second maximum at lower values is evoked by skies covered by clouds. Hence, the maximum at high irradiance values is considerably more pronounced at sunnier locations than at locations with very variable weather.

It can be seen that the new algorithm is reproducing the frequency distributions of the global irradiance much better than the conventional approaches. Mid irradiance values are not overestimated, and a good modelling quality is present at high irradiance values. However, very high irradiances above 1100 W/m^2 are slightly overestimated.

If those frequency distributions are looked at in the form of the clearness index k_t , the problems of the existing algorithms become equally apparent (see Figures 10 and 11). With the improved algorithm the k_t distributions can be reproduced very well, and the typical bimodal character of the distribution is modelled very precisely for cloudy locations (Lindenberg) as well as for sunnier locations (Carpentras) with a pronounced clear sky peak of a k_t value near 1. The practical relevance of these effects was demonstrated with the help of the introductory example of the maximum power clipping at 70%.

These visual impressions give an indication, but an analysis of the uncertainty can be used for quantitative assessment. Table 4 lists root mean square errors (RMSE) for all distribution diagrams shown in Figures 8–11. For each irradiance or clearness index class i the modelled distributions are compared to the measured data, and the deviations are squared and summed up for the whole range

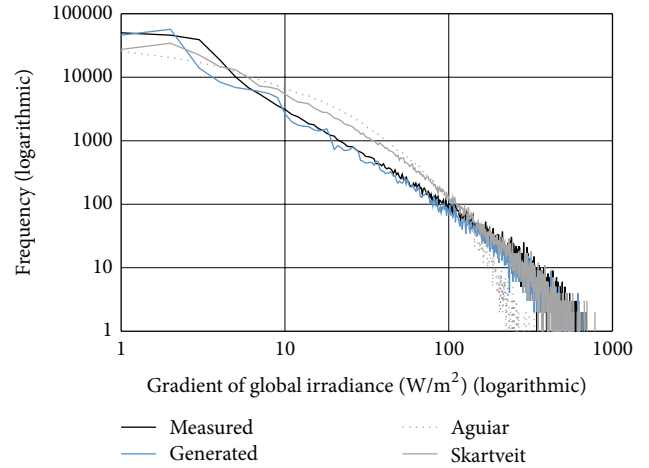


FIGURE 7: Frequency of gradients of the global irradiance in Carpentras, France (2001). As in Figure 6, the differences of the models for gradient values of less than 10 W/m^2 are comparable. In the range of 10 to 100 W/m^2 , the new model (blue) shows a better congruence with the measured data (black) than the models of Aguiar and Skartveit (grey), while only the model of Aguiar fails to produce good congruence for gradient values of more than 100 W/m^2 .

TABLE 4: Root mean square error (RMSE) values comparing the frequency distributions of the existing and the new algorithms with measured data. Smaller values of RMSE denote better congruence of the frequency distributions of modelled one-minute values with measured values.

Model	RMSE of irradiance in %		RMSE of k_t in counts	
	Lindenberg	Carpentras	Lindenberg	Carpentras
Aguiar	0.530	0.549	596	801
Skartveit	0.684	0.575	862	962
New	0.210	0.237	207	248

and then divided by the number of classes n . The square root of this value gives the RMSE listed:

$$\text{RMSE} = \sqrt{\frac{1}{n} \sum_{i=1}^n (x_{\text{Model},i} - x_{\text{Measurement},i})^2}. \quad (8)$$

The RMSE of both the irradiance and the clearness index distributions can be considerably decreased with the new algorithm compared to the conventional ones. In the case of Carpentras both distribution RMSE can be reduced between 24 % and 35 %, in case of Lindenberg between 31 % and 43 %.

To analyze the influence of the amount of input data for the TPM on the synthesis quality of the algorithm, the creation process of the TPM is varied as follows.

First, the algorithm is processed three times with its original setup, which includes all TPM except the ones from the respective location, to estimate the influence of the random Markov number generator on the RMSE range. Second, only TPM of the respective location are used. In a third iteration, the only measurement values included in the creation process are taken from BSRN stations that are located in the same

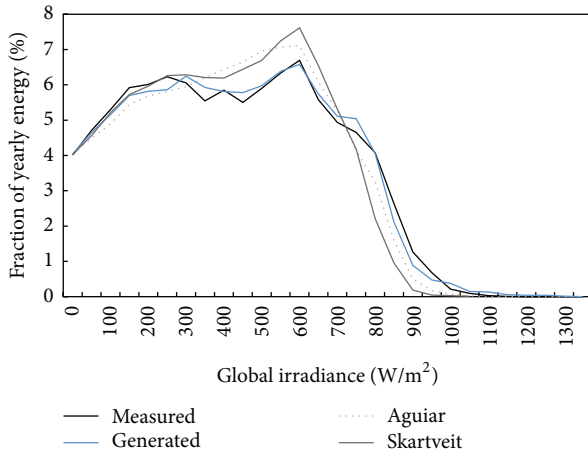


FIGURE 8: Frequency distributions of measured global irradiance for Lindenberg (Germany, 2005) against values generated by different algorithms. Mid values are slightly overestimated, and high values are underestimated by the existing models (grey dotted), resulting in RMSE of 0.530% for Aguiar and 0.684% for Skartveit. The modelling quality of the new method (blue) does not overestimate mid irradiance values and shows only little underestimation of high irradiance values. The new RMSE can be reduced to 0.210%.

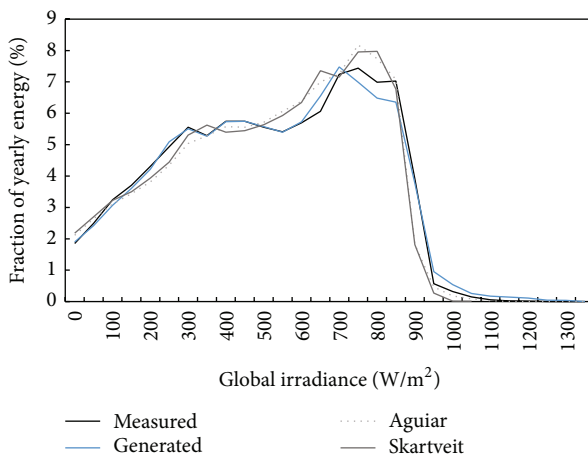


FIGURE 9: Frequency distributions of measured global irradiance for Carpentras (France, 2001) against values generated by different algorithms. For locations with higher yearly global irradiation, the high irradiance peak grows. Mid values are slightly overestimated, and high values are underestimated by the existing models (grey dotted), resulting in RMSE of 0.549% for Aguiar and 0.575% for Skartveit. The modelling quality of the new method (blue) does not overestimate mid irradiance values and shows only little underestimation of high irradiance values. The new RMSE can be reduced to 0.237%.

climate zone as per the definition of Köppen [19]. Current data published by Rubel and Kottek [20] is taken to assign the locations to climate zones. Lindenberg is located in the climate zone *Cfb*, which mainly comprises Western Europe. In the BSRN dataset there are another seven locations in this climate zone: Cabauw (the Netherlands), Camborne and Lerwick (Great Britain), Cener (Spain), Lauder (New Zealand),

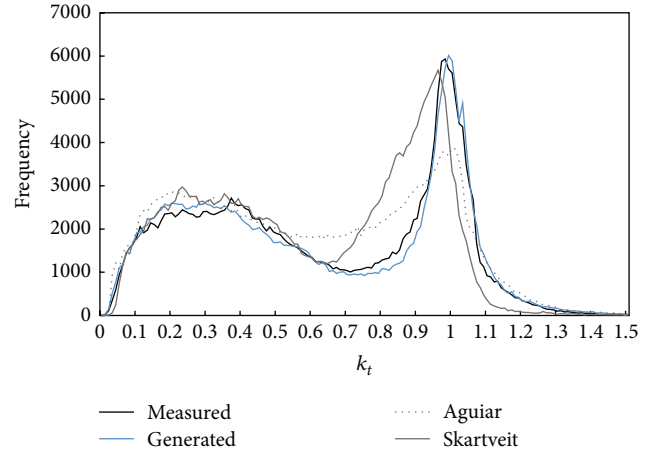


FIGURE 10: Frequency distributions of the clearness index k_t for Lindenberg (Germany, 2005). With the new method, the RMSE between measurement and synthesis can be reduced significantly (RMSE = 596 and 862 counts for Aguiar and Skartveit and RMSE = 207 counts for new method).

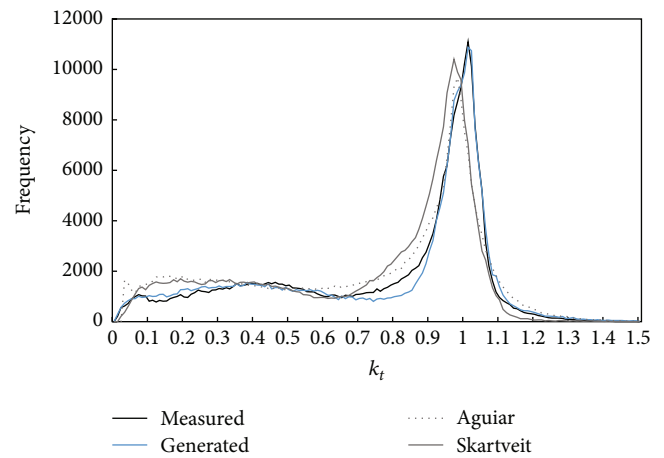


FIGURE 11: Frequency distributions of the clearness index k_t for Carpentras (France, 2001). For locations with higher yearly global irradiation, the second peak (clear sky) of the distribution grows. With the new method, the RMSE between measurement and synthesis can be reduced significantly (RMSE = 801 and 962 counts for Aguiar and Skartveit and RMSE = 248 counts for new method).

Palaiseau (France), and Payerne (Switzerland). According to Rubel and Kottek, Carpentras lies in climate zone *Csa*, but unfortunately there is no other location of this climate zone in the BSRN dataset. So this third iteration is conducted for Lindenberg only. The fourth iteration comprises the usage of all available TPM, this time including the TPM of Lindenberg and Carpentras.

The synthesis of one-minute irradiance values is now repeated with all varied TPM. The RMSE values are determined according to the previous chapter. Table 5 compares the error values of the variations with the original version of the process.

TABLE 5: Comparison of synthesis quality of the new algorithm as a function of input data for the locations of Lindenberg, Germany, 2005, and Carpentras, France, 2001.

Variation	RMSE of irradiance in %		RMSE of k_i in counts	
	Lindenberg	Carpentras	Lindenberg	Carpentras
All except own (1)	0.210	0.237	207	248
All except own (2)	0.244	0.174	210	273
All except own (3)	0.235	0.217	204	239
Own TPM only	0.232	0.199	202	279
<i>Cfb</i> only	0.193	—	315	—
All TPM	0.253	0.186	204	254

The repetition of the synthesis process with the original setup (all TPM except own 1–3) demonstrates the RMSE range that can be expected due to the random nature of the Markov number generator. The interesting aspect of the various TPM modifications (own TPM only, *Cfb* TPM only, and all TPM) is that the resulting RMSE mostly lie well within the natural RMSE range of the original algorithm. In other words, the synthesis quality remains approximately the same, whether the algorithm uses only data of the respective location or all globally available data except those from the respective location. By classifying the weather situation on a daily level, the influence of location specific weather phenomena is reduced at the best. This implies that the presented algorithm is location-independent and can be applied to every location worldwide.

4. Conclusions

An improved method for synthesizing one-minute time series of global irradiance has been presented that was developed on the basis of a large worldwide measurement dataset. It combines the advantages of conventional algorithms and adds new elements like the differentiation of weather conditions. It could be demonstrated that with the new approach it is possible to synthesize one-minute values of high statistical quality and realistic temporal variability. The independence on the location has been shown for selected cases. Such an independence would allow synthesizing one-minute time series for any location.

Conflict of Interests

The authors declare that there is no conflict of interests regarding the publication of this paper.

Acknowledgments

The authors acknowledge support by Deutsche Forschungsgemeinschaft and Open Access Publishing Fund of Leibniz Universität Hannover.

References

- [1] R. Haselhuhn, U. Hartmann, and P. Vanicek, "Uncertainty in yield prediction—what are the causes, how can they be reduced?" in *Proceedings of the 25th European Photovoltaic Solar Energy Conference and Exhibition*, pp. 4722–4725, 2010.
- [2] B. Herteleer, J. Cappelle, and J. Driesen, "Quantifying low-light behaviour of photovoltaic modules by identifying their irradiance-dependent efficiency from data sheets," in *Proceedings of the 27th European Photovoltaic Solar Energy Conference and Exhibition*, pp. 3714–3719, 2012.
- [3] P. Vanicek, G. Karg, and R. Haselhuhn, "Quality of the calculation of inverter losses with standard simulation programs," in *Proceedings of the 26th European Photovoltaic Solar Energy Conference and Exhibition*, pp. 3772–3775, 2011.
- [4] EEG, *Act on Granting Priority to Renewable Energy Sources*, Renewable Energy Sources Act, EEG, 2012.
- [5] R. J. Aguiar, M. Collares-Pereira, and J. P. Conde, "Simple procedure for generating sequences of daily radiation values using a library of Markov transition matrices," *Solar Energy*, vol. 40, no. 3, pp. 269–279, 1988.
- [6] R. Aguiar and M. Collares-Pereira, "TAG: a time-dependent, autoregressive, Gaussian model for generating synthetic hourly radiation," *Solar Energy*, vol. 49, no. 3, pp. 167–174, 1992.
- [7] A. Skartveit and J. A. Olseth, "The probability density and autocorrelation of short-term global and beam irradiance," *Solar Energy*, vol. 49, no. 6, pp. 477–487, 1992.
- [8] C. A. Glasbey, "Non-linear autoregressive time series with multivariate Gaussian mixtures as marginal distributions," *Journal of the Royal Statistical Society, Series C: Applied Statistics*, vol. 50, no. 2, pp. 143–154, 2001.
- [9] A. Voskrebenez, S. Riechelmann, A. Bais, H. Slaper, and G. Seckmeyer, "Estimating probability distributions of solar irradiance," *Theoretical and Applied Climatology*, 2014.
- [10] H. F. Assunção, J. F. Escobedo, and A. P. Oliveira, "Modelling frequency distributions of 5 minute-averaged solar radiation indexes using Beta probability functions," *Theoretical and Applied Climatology*, vol. 75, no. 3-4, pp. 213–224, 2003.
- [11] J. Tovar, F. J. Olmo, F. J. Batlles, and L. Alados-Arboledas, "Dependence of one-minute global irradiance probability density distributions on hourly irradiation," *Energy*, vol. 26, no. 7, pp. 659–668, 2001.
- [12] Markov, "Rasprostranenie zakona bol'shikh chisel na velichiny, zavisyaschie drug ot druga," *Izvestiya Fiziko-Matematicheskogo Obschestva pri Kazanskom Universitete, Seriya 2*, vol. 15, pp. 135–156, 1906.
- [13] R. A. Howard, *Dynamic Probabilistic Systems*, vol. 1, John Wiley & Sons, New York, NY, USA, 1971.
- [14] D. A. McCracken, *Synthetic high resolution solar data [M.S. thesis]*, Department of Mechanical Engineering, University of Strathclyde, 2011.
- [15] G. Bourges, "Reconstitution des courbes de fréquence cumulées de l'irradiation solaire globale horaire reçue par une surface plane," Report CEE 295-77, ESF of Centre d'Énergétique de l'École Nationale Supérieure des Mines de Paris, tome II, Paris, France, 1979.
- [16] E. L. Maxwell, "A quasi-physical model for converting hourly global horizontal to direct normal insolation," Tech. Rep. SERI/TR-215-3087, Solar Energy Institute, Golden, Colo, USA, 1987.

- [17] I. Reda and A. Andreas, "Solar position algorithm for solar radiation applications," *Solar Energy*, vol. 76, no. 5, pp. 577–589, 2004.
- [18] J. S. Stein, C. W. Hansen, A. Ellis, and V. Chadliev, "Estimating annual synchronized 1-min power output profiles from utility-scale PV plants at 10 locations in Nevada for a solar grid integration study," in *Proceedings of the 26th European Photovoltaic Solar Energy Conference and Exhibition*, pp. 3874–3880, 2011.
- [19] W. Köppen, "Klassifikation der Klimate nach Temperatur, Niederschlag und jahreslauf," *Petermanns Geographische Mitteilungen*, vol. 64, pp. 193–203, 243–248, 1918.
- [20] F. Rubel and M. Kottke, "Observed and projected climate shifts 1901–2100 depicted by world maps of the Köppen-Geiger climate classification," *Meteorologische Zeitschrift*, vol. 19, no. 2, pp. 135–141, 2010.

3.2 Diffuse decomposition models

The aim of diffuse composition models is to calculate the fraction of the diffuse irradiance, when only the global horizontal irradiance was measured. The diffuse fraction is important to know for two reasons: As input for transposition models that calculate the global irradiance on tilted surfaces. And for PV systems that are only capable of converting the direct fraction of the incident solar irradiance, like for concentrating PV systems.

The topic is on the list of meteorologists and scientists for more than 50 years now, starting with the remarkable work of Liu and Jordan in 1960 [53].

In the publication presented here a selection of diffuse fraction models is included in a worldwide validation against measured one-minute time series. The main part of the publication covers the description of a new model for the calculation of the diffuse fraction that is also based on high quality measurement data from BSRN and incorporates three sub-algorithms, two of which rely on precompiled probability matrices and Markov chains.

Compared to existing models, the new approach realizes a reduction by 50% of the deviations of the modelled from measured diffuse irradiation per year, the root mean squared deviation is reduced by 18%. In contrast to existing models, the annual deviation of the diffuse irradiation is smaller than 20% in all cases, while it is smaller than 10% in 80% of the analyzed test cases.

Since it is a complex and time consuming task to implement the algorithm, it is publicly available for researchers on <http://www.pvmodelling.org>.

Article

A New Model for Estimating the Diffuse Fraction of Solar Irradiance for Photovoltaic System Simulations

Martin Hofmann ^{1,2,*} and Gunther Seckmeyer ²

¹ Valentin Software GmbH, Stralauer Platz 34, 10243 Berlin, Germany

² Leibniz Universität Hannover, Institute for Meteorology and Climatology, Herrenhäuser Straße 2, 30419 Hannover, Germany; seckmeyer@muk.uni-hannover.de

* Correspondence: martin.hofmann@valentin-software.com, Tel.: +49-30-588-439-0

Academic Editor: Senthilarasu Sundaram

Received: 21 December 2016; Accepted: 13 February 2017; Published: 18 February 2017

Abstract: We present a new model for the calculation of the diffuse fraction of the global solar irradiance for solar system simulations. The importance of an accurate estimation of the horizontal diffuse irradiance is highlighted by findings that an inaccurately calculated diffuse irradiance can lead to significant over- or underestimations in the annual energy yield of a photovoltaic (PV) system by as much as 8%. Our model utilizes a time series of global irradiance in one-minute resolution and geographical information as input. The model is validated by measurement data of 28 geographically and climatologically diverse locations worldwide with one year of one-minute data each, taken from the Baseline Surface Radiation Network (BSRN). We show that on average the mean absolute deviation of the modelled and the measured diffuse irradiance is reduced from about 12% to about 6% compared to three reference models. The maximum deviation is less than 20%. In more than 80% of the test cases, the deviation is smaller 10%. The root mean squared error (RMSE) of the calculated diffuse fractions is reduced by about 18%.

Keywords: diffuse; diffuse fraction; irradiance; model; photovoltaic (PV); simulation; irradiation; Baseline Surface Radiation Network (BSRN)

1. Introduction

Adapting the common terminology in energy meteorology to differentiate between the power and energy of the solar radiation, the word ‘irradiance’ is used in this work to denote the instantaneous solar power per square meter in W/m^2 , whereas the word ‘irradiation’ refers to the integral of the irradiance over time, thus denoting the energy of the solar radiation in Ws/m^2 or kWh/m^2 [1].

In photovoltaic (PV) system simulations, the global horizontal irradiance and the ambient temperature are the two most important inputs in order to determine the PV system’s energy output. The global horizontal irradiance is split up in its direct and diffuse components. These components are then separately translated to a tilted plane if the PV system in question has a module orientation that differs from the horizontal plane. In simple terms the global irradiance incident on a tilted module is then calculated as the sum of the direct and the diffuse irradiance on the tilted plane.

The model for estimating the diffuse fraction of the global horizontal irradiance is hence the first element in a chain of models that is necessary to simulate the electrical output of a PV system. As such, it has strong influence on the final output of the simulation, which is demonstrated by the following comparative simulations for two locations: Lindenberg, Germany and Gobabeb, Namibia. The analysed PV system is a standard 8 kWp (kilo Watt peak) grid connected system, the simulation is conducted in one-minute resolution with measurement data from the Baseline Surface Radiation Network (BSRN) [2].

During the four exemplary days in June in Lindenberg, Germany, chosen for Figure 1, the model used for this comparison (reduced version of Reindl et al. [3]) underestimates the diffuse irradiance by 18%. In the next step of the simulation, the global irradiance on the tilted plane is calculated. In this case the modules are facing south and are elevated by 30° from the horizontal. The model applied for this step is from Hay and Davies [4]. When using the modelled horizontal diffuse irradiance, the resulting global irradiance on the modules is still 9% lower than using the measured horizontal diffuse irradiance.

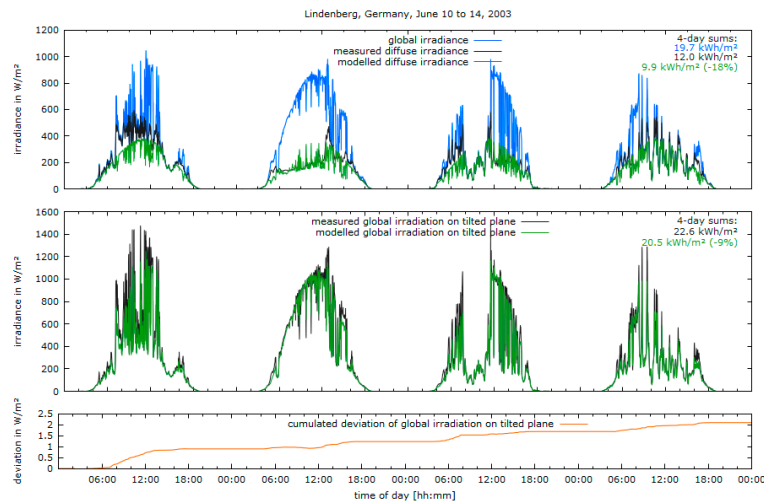


Figure 1. *Top:* Measured (grey) and modelled (green) time series of diffuse irradiance on a horizontal surface for four days in Lindenberg, Germany. Global irradiance (blue) for reference. The calculation of diffuse irradiance in this example was done with the reduced model of Reindl et al. [3]. The model underestimates the four-day sum of the diffuse irradiation by 18%.

Middle: The global irradiance on a tilted photovoltaic (PV) module (facing south, tilted by 30°) for the same four days. The model used for calculating the irradiance on a tilted surface is from Hay and Davies [4]. Due to the underestimation of the diffuse irradiance (see top), the four-day sum of the global irradiation on the PV module based on modelled values falls below the global irradiation based on measured values by -9% .

Bottom: The resulting cumulated deviation of the modelled global irradiation on the tilted plane from the measured. The plot shows that one of the main sources of deviation is the modelling of highly variable irradiance situations, as observed e.g., on 10 June, between 08:00 and 12:00.

The rest of the PV system model chain is then simulated with the help of the simulation core of PV software provider Valentin Software (Berlin, Germany) [5]. Table 1 lists the results of the comparison.

During these four days, the total PV energy yield would be 65.6 kWh when using the measured horizontal diffuse irradiance values. With the diffuse irradiance modelled by Reindl et al. [3], the total PV energy yield is only 60.2 kWh—an underestimation of 8.3%. The comparison was also conducted for the whole year 2003 in Lindenberg, where the annual deviation of the modelled diffuse irradiance is -7.2% , leading to a deviation of the annual PV energy output of -2.7% .

The second half of Table 1 lists the results of the same comparison that was conducted for the location of Gobabeb in Namibia, for the year 2014. Here, the deviation of the annual diffuse irradiation is as high as 42% which leads to an overestimation of the global irradiation of the module surface of 8.3% and to an overestimation of the annual PV energy yield of 7.6%.

These examples highlight the importance of a more accurate estimation of the horizontal diffuse irradiance. An inaccurately calculated diffuse irradiance can lead to significant over- or underestimations in the annual energy yield of a PV system. This is especially relevant in the price sensitive market of PVs, where only few percent more or less of PV energy output can render a project possible or uneconomical [6].

Table 1. Measured and modelled diffuse irradiation for Lindenberg, Germany (LIN), and Gobabeb, Namibia (GOB). The top section refers to the figures above, time ranges from 10–13 May 2003. The modelled underestimation of the diffuse irradiation by -17.9% leads to an underestimation of the global irradiation on the tilted PV module by -9.3% , hence leading to an underestimation of the simulated PV energy yield by 8.3% . When considering the whole year (2nd section), the modelled diffuse irradiation differs from the measured value by -7.2% , leading to an underestimation of the irradiation on module surface by -3.1% . The difference in the annual PV energy yield is -2.7% . In the 3rd and 4th section, the results of the same analysis are presented for Gobabeb, Namibia. Here, the PV module faces North and is tilted at 23° . The modelled sum of diffuse irradiation for selected days (23–26 July 2014) is 20.4% higher than the measured sum, leading to a deviation in the PV energy of 4.4% . Over the whole year of 2014, the deviation of the diffuse irradiation is even 42% , which causes a difference in the annual PV yield of 7.6% .

LIN, 10–13 May 2003	Unit	with Measured Data	Modelled	Deviation
Global horizontal irradiation	kWh/m ²	19.7	-	-
Diffuse irradiation	kWh/m ²	12.0	9.9	-17.9%
Global irradiation on tilted surface	kWh/m ²	22.6	20.5	-9.3%
PV energy yield	kWh	65.6	60.2	-8.3%
LIN, whole year 2003	Unit	with Measured Data	Modelled	Deviation
Global horizontal irradiation	kWh/m ²	1185.1	-	-
Diffuse irradiation	kWh/m ²	555.9	515.7	-7.2%
Global irradiation on tilted surface	kWh/m ²	1467.0	1422.0	-3.1%
PV energy yield	kWh	4339.2	4221.4	-2.7%
GOB, 23–26 July 2014	Unit	with Measured Data	Modelled	Deviation
Global horizontal irradiation	kWh/m ²	18.2	-	-
Diffuse irradiation	kWh/m ²	4.6	5.5	20.4%
Global irradiation on tilted surface	kWh/m ²	22.5	23.7	5.0%
PV energy yield	kWh	66.2	69.1	4.4%
GOB, whole year 2014	Unit	with Measured Data	Modelled	Deviation
Global horizontal irradiation	kWh/m ²	2433.1	-	-
Diffuse irradiation	kWh/m ²	454.9	645.8	42.0%
Global irradiation on tilted surface	kWh/m ²	2401.9	2600.8	8.3%
PV energy yield	kWh	6808.7	7325.4	7.6%

2. Measurement Data and Methodology

In the following section the measurement data and the methodology used in this contribution are presented.

2.1. Data basis (Baseline Surface Radiation Network)

As a source of high quality measurement data the data base of the BSRN is used [2]. The BSRN comprises 59 stations worldwide, 44 of which provide one-minute measurements of global horizontal and diffuse horizontal irradiance. The time range of the measurements starts in 1992 for the first stations and is still running until now. For this study the following criteria were applied for selecting the datasets:

- High annual completeness of one-minute measurements of global and diffuse irradiance;
- Between 60° North and -60° South;
- No leap years.

Table 2 gives an overview of the locations and years that were used for validation. In total, 28 locations with one year of measurement each were selected. The datasets feature a high geographic and climatological diversity. The last column of the table lists the annual completeness of the measurements (ACM) in %. The validation datasets comprise more than seven million data points (nights omitted) on which the following analysis is based.

Table 2. Overview over the 28 datasets that were used in this work. The locations are spread over the globe between -45° South and 52° North. Height above sea level, surface, topography and climate zones (according to Köppen [7]) show a high level of variation. The years of measurement were chosen to provide a high annual completeness of measurement (ACM), i.e., as few missing data points as possible. The total resulting amount of data points that is used in the following analysis exceeds 14.7 million (or approximately 7 million when omitting night time).

ID	Name	Country	Latitude in $^\circ$	Longitude in $^\circ$	Height in m	Time Zone	Surface	Topography	Climate Zone	ACM in %
ASP 2005	Alice Springs	Australia	-23.798	133.888	547	9.5	grass	flat, rural	BWh	99.4
BIL 2003	Billings	USA	36.605	-97.516	317	-6	grass	flat, rural	Cfa	99.6
BOU 2009	Boulder	USA	40.05	-105.007	1577	-7	grass	flat, rural	BSk	99.0
BRB 2010	Brasilia	Brasil	-15.601	-47.713	1023	-3	concrete	flat, rural	Aw	96.6
CAB 2009	Cabauw	Netherlands	51.971	4.927	0	1	grass	flat, rural	Cfb	99.1
CAM 2003	Camborne	UK	50.217	-5.317	88	0	grass	flat, rural	Cfb	90.4
CLH 2013	Chesapeake Light	USA	36.905	-75.713	37	-5	water, ocean	flat, rural	Cfa	99.8
CNR 2011	Cener	Spain	42.816	-1.601	471	1	asphalt	mountain valley, urban	Cfb	99.8
COC 2011	Cocos Islands	Cocos Islands	-12.193	96.835	-1	6.5	n.a.	n.a.	Af	95.6
DAA 2003	De Aar	South Africa	-30.667	23.993	1287	2	sand	flat, rural	BSk	88.1
DAR 2011	Darwin	Australia	-12.425	130.891	30	9.5	grass	flat, rural	Aw	100
FUA 2011	Fukuoka	Japan	33.582	130.375	3	9	asphalt	flat, urban	Cfa	99.9
GOB 2014	Gobabeb	Namibia	-23.561	15.042	407	1	n.a.	flat rural	BWh	100
IZA 2011	Izaña	Spain	28.309	-16.499	2372.9	0	rock	mountain top	Csb	96.1
LAU 2005	Lauder	New Zealand	-45.045	169.689	350	12	grass	flat, rural	Cfb	98.1
LER 2003	Lerwick	UK	60.133	-1.183	84	0	grass	hilly, rural	Cfb	100
LIN 2003	Lindenberg	Germany	52.21	14.122	125	1	cultivated	hilly, rural	Cfb	100
PAL 2011	Palaiseau	France	48.713	2.208	156	1	concrete	flat, urban	Cfb	99.7
PAY 2009	Payerne	Switzerland	46.815	6.944	491	1	cultivated	hilly, rural	Cfb	99.9
REG 2009	Regina	Canada	50.205	-104.713	578	-6	cultivated	flat, rural	BSk	100
SAP 2011	Sapporo	Japan	43.06	141.328	17.2	9	asphalt	flat, urban	Dfb	99.9
SBO 2009	Sede Boqer	Israel	30.905	34.782	500	2	desert rock	hilly, rural	Cwb	98.2
SMS 2007	São Martinho da Serra	Brasil	-29.443	-53.823	489	-3	concrete	flat, rural	Cfa	91.5
SOV 2001	Solar Village	Saudi Arabia	24.91	46.41	650	3	desert, sand	flat, rural	BWh	100
TAM 2006	Tamanrasset	Algeria	22.78	5.51	1385	1	desert, rock	flat, rural	BWh	99.9
TAT 2006	Tateno	Japan	36.05	140.133	25	9	grass	flat, urban	Cfa	99.9
TOR 2010	Toravere	Estonia	58.254	26.462	70	2	grass	flat, rural	Dfb	100
XIA 2009	Xianghe	China	39.754	116.962	32	8	desert, rock	flat, rural	Dwa	100

2.2. Description of Quantities and Models

For the calculation of the position of the sun, the solar position algorithm provided by the National Renewable Energy Laboratory (NREL; Golden, CO, USA) is used [8]. The clear sky irradiance E_{clear} is calculated on the basis of an adaption of the approach of Bourges [9]:

$$E_{\text{clear}} = 0.78E_{\text{ext}} \sin(\gamma_S)^{1.15} \quad (1)$$

where γ_S is the elevation of the Sun and E_{ext} is the extra-terrestrial irradiance. The extra-terrestrial irradiance was calculated using Maxwell's approach [10]. In 2014 this formula was identified as the most accurate for another subset of BSRN data by Hofmann et al. [11]. The clearness index kt is the fraction of the measured global irradiance to the clear sky irradiance:

$$kt = \frac{E_{\text{global, measured}}}{E_{\text{clear}}} \quad (2)$$

In the models for calculating the diffuse fraction of the global irradiance that are presented in Section 2.3 a simpler approach of calculating the clear sky index is used:

$$E_{\text{clear}} = E_{\text{ext}} \sin(\gamma_S) \quad (3)$$

This causes the kt value at clear sky to be around 0.8 instead of 1 in the existing models. For the comparison of the results in Section 4, the calculation of the clearness index occurs according to the respective model description.

All PV system simulations are conducted using the simulation core of PV*SOL, a commercial PV system planning and simulation software by Valentin Software. More information about the models that are relied on in the simulation core can be found at PV*SOL [5].

2.3. Presentation of Existing Models

For the estimation of the diffuse fraction of the global horizontal irradiance, several algorithms were developed in the past. Most of them can be categorized as models with one or two parameters as input. The one-parameter models feature a simple dependency of the diffuse fraction (df) on the clearness index (kt), cf. Figure 2.

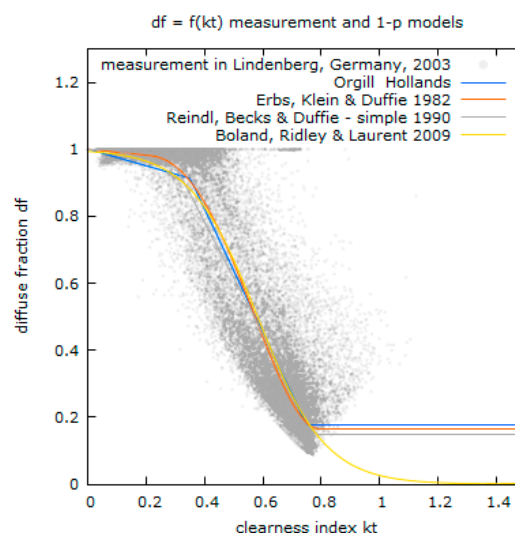


Figure 2. Measured diffuse fraction over clearness index kt for one year of measurement (grey points, extract of 2003) in Lindenberg, Germany. Line plots: Schematic overview of existing one-parameter models. Typically the models define three sections with varying $df = f(kt)$ functions.

These models typically define three functions for different ranges of kt . These kt ranges can be more or less referred to as different cloud situations. A kt value of less than 0.4 means only 40% of the possible global irradiance is measured, which is a good indicator for overcast skies. The maximum kt value that is detected at clear sky conditions is around 0.78–0.8. In between those areas, i.e., for kt values between 0.4 and 0.78, broken cloud situations are most likely [1,12]. Values of $kt > 1$ are possible due to broken cloud enhancement, firstly stated for the ultraviolet by Nack and Green [13] and later confirmed by Seckmeyer et al. [14]. Values of $kt > 1$ are possible at all wavelengths of the solar spectrum.

The first model, a one-parameter approach, was presented by Liu and Jordan in 1960 [15], but it soon became apparent that it was not able to produce good results in other locations than it was designed for (Blue Hill, MA, USA) [16,17].

In consequence, other models were developed that can also be categorized as one-parameter models: Orgill and Hollands [18], Erbs, Klein and Duffie [19], Reindl, Beckman and Duffie [3] and Boland and Ridley [20]. A schematic overview of those models is provided in Figure 2, along with sample measurement data of Lindenberg, Germany, 2003, for reference. Other one-parameter approaches include the model by Oliveira et al. [21] that provides varying clearness index polynomials for three periods per year (December–January, April–August and September–March).

Another category of algorithms is formed by the two-parameter models that—in addition to the clearness index kt —also make use of the sun height, γ_S . Two-parameter models include the approaches by Reindl, Beckman and Duffie [3], Skartveit and Olseth [12] and Maxwell [10]. The reduced version of the two-parameter model of Reindl, Beckman and Duffie [3] is presented in Figure 3.

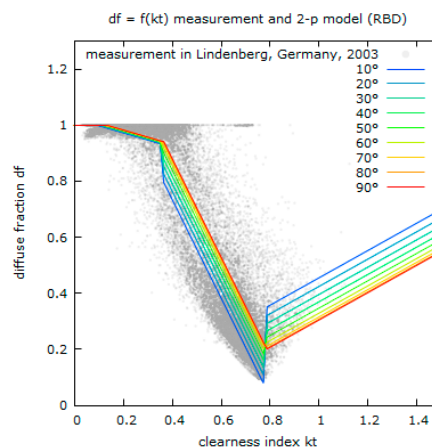


Figure 3. Measured diffuse fraction over clearness index kt for one year of measurement (grey points, extract of 2003) in Lindenberg, Germany. Line plots: The model by Reindl, Beckman and Duffie [3] (reduced version), using two parameters (kt and sun height) as input.

Not classifiable as one- or two-parameter model is the noteworthy approach by Furlan et al. [22] who developed a multi-parameter regression model for data from Sao Paolo, Brazil. Another important contribution was achieved by the model by Perez and Ineichen [23], which features a dynamic time-series approach to model the direct normal from the global irradiance based on the DISC model by Maxwell [10].

A good overview and an approach of global validation of the above mentioned models for calculating the diffuse fraction, also using BSRN data, is given by Zernikau [17]. In this thesis it was also shown that all analysed one- and two-parameter models showed relative mean absolute errors ($rMAE$) of $(10.4 \pm 0.4)\%$ for the 24 BSRN locations that were included in the study. The author also analysed the minimal $rMAE$ that can be achieved with a one- or two-parameter model by generating global medians of measurements of the diffuse fraction and the clearness index. According to this study, the minimal globally achievable $rMAE$ for any two-parameter model is 8.9%.

Another one-location comparison of the models was conducted for Athens, Greece, by Kambezidis [24]. Similarly, a study comparing ten models was presented by Jacovides et al. for validation data of Athalassa, Cyprus [25]. A model-to-model comparison for Hong Kong without validation on measurement data is provided by Wong [26]. A comparison of eight models for the location of Vienna, Austria, was conducted by Dervishi [27], resulting in findings that are in general agreement to the above mentioned studies.

3. Presentation of a New Model for the Diffuse Fraction of Solar Irradiance

In order to reduce the uncertainty of PV system simulations, a new model for calculating the diffuse fraction of global horizontal irradiance is presented in this section. The model consists of three parts that are calculated independently and then combined depending on statistic features of the clearness index. Each part is presented and afterwards the combination of the three parts into a single resulting diffuse fraction df is explained.

3.1. Part One. Diffuse Fraction as Function of Clearness Index

Like existing models with one parameter, this part of the new model makes use of the relation between the clearness index kt and the diffuse fraction. Instead of parameterized functions, a matrix of probabilities is utilized. For the generation of the matrix, the one-minute time series of global and diffuse horizontal irradiance are converted into value pairs of the clearness index kt and the diffuse fraction df , following the equations in Section 2.2. Each value pair is then stored into a matrix with kt ranging from 0 to 1.5 and df ranging from 0 to 1, both with a step size of 0.01. The frequency of occurrence of a specific df value for a given kt value is then converted into a probability value, so that for every value of kt a function of cumulated probabilities can be calculated. Figure 4 shows an example of such a probability matrix. In the matrix shown here, measurement values from Alice Springs, Australia (2009), Billings, USA (2005), Boulder, USA (2010), Brasilia, Brazil (2011), Cabauw, The Netherlands (2011), Cener, Spain (2010), De Aar, South Africa (2003), Fukuoka, Japan (2013), Gobabeb, Namibia (2013), Lauder, New Zealand (2007), Lerwick, UK (2002), Lindenberg, Germany (2002), Payerne, Switzerland (2010), Regina, Canada (2011), Tateno, Japan (2003) and Xianghe, China (2006) were incorporated.

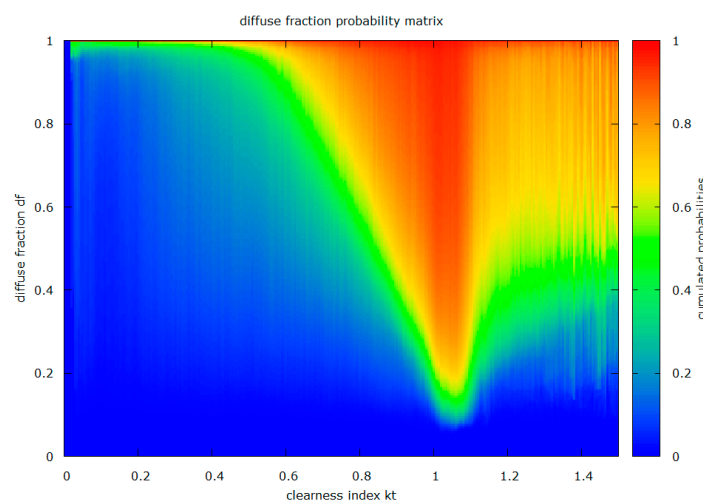


Figure 4. A probability matrix of the diffuse fraction as a function of the clearness index kt . For each value of kt , this matrix describes the probability with which a certain value of diffuse fraction will occur. The matrix correlates with the existing simple one-parameter models mentioned in Section 2.3, but it is based on measurements. Therefore the natural variability is better described by the model especially for high values of kt ($kt > 1.1$, irradiance enhancement due to reflections by broken clouds) while preserving the strong relation at low levels of kt ($kt < 0.4$, overcast sky).

In order to determine a value for df for a given kt , the procedure is as follows. Since this is the first part of the new model, the diffuse fraction of this part is referred to as df_1 :

- (1) Select column of probability matrix that corresponds to the kt value;
- (2) Generate a Markov number r_M (randomized number between 0 and 1) [28];
- (3) Select the row where r_M is smaller than the cumulated probabilities for the first time;
- (4) The selected row corresponds to df_1 value.

The usage of real measurement values, incorporated into a matrix of probabilities, holds the advantage of preserving the natural relationship of the diffuse fraction and the clearness index and additionally resulting in a more realistic variability of the modelled df value series.

3.2. Part Two. Change of df as Function of Change of kt

By analyzing the extensive BSRN measurement database, a strong correlation has been found between the relative changes of the clearness index (from one minute to the next) to changes of the diffuse fraction. In Figure 5 this correlation is shown for Lindenberg, Germany, for the year 2003.

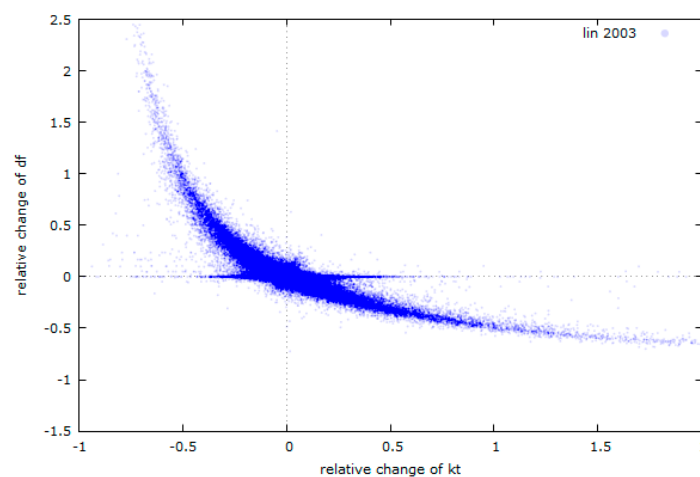


Figure 5. Scatter plot of the relative changes of the diffuse fraction over the relative changes of the clearness index for Lindenberg, Germany, 2003. This strong relation is very valuable for modelling a realistic behaviour of the diffuse fraction over the day, since it depends highly on the behaviour of kt . The area where the change of df is 0 while kt shows relative changes between -0.5 and 0.5 , i.e., df is changing while kt is not, indicates days with movement of broken clouds, the reflection on which causes the measured global irradiance to change rapidly without changing its diffuse fraction.

It was observed that for positive relative changes of kt (when the current kt is higher than the kt one minute before), the diffuse fraction will most likely show a negative relative change. If the relative change of kt is negative, the change of the diffuse fraction will be positive.

There are situations, however, where kt is changing from one minute to the next without an observable change of df (compare the horizontal value accumulation at $d_{df} = 0$). These situations are typical for days with rapid irradiance enhancements due to moving broken clouds.

In correspondence to part 1, the relationship between the relative change of df and the relative change of kt (d_{kt}) is also expressed in a matrix of probabilities, displayed in Figure 6. This matrix is only used in the d_{kt} range of -0.5 to 1 , since the amount of measurement values outside of this range is too small, which results in unwanted noise. The procedure to retrieve a value for the diffuse fraction in this part, df_2 , is as follows:

- (1) Calculate the relative change of kt as:

$$d_{kt} = kt_{\text{now}} / kt_{\text{before}} - 1 \quad (4)$$

- (2) For d_{kt} greater than -0.5 and smaller than 1
- Select the column of the probability matrix that corresponds to d_{kt} ;
 - Generate a Markov number r_M (randomized number between 0 and 1) [28];
 - Select the row where r_M is smaller than the cumulated probabilities for the first time;
 - The selected row corresponds to change of df , that is:

$$d_{df} = df_{\text{now}} / df_{\text{before}} - 1 \quad (5)$$

- (3) For d_{kt} smaller than -0.5 , d_{df} is not taken from the matrix, but extrapolated as:

$$d_{df} = 0.5d_{kt}^4 - 1.23d_{kt}^3 + 1.1d_{kt}^2 - 0.87d_{kt} \quad (6)$$

- (4) For d_{kt} greater than 1 , d_{df} is extrapolated as:

$$d_{df} = -0.35 - 0.15d_{kt} \quad (7)$$

- (5) The diffuse fraction for part 2, df_2 , can now be calculated as:

$$df_2 = d_{df}df_{\text{before}} \quad (8)$$

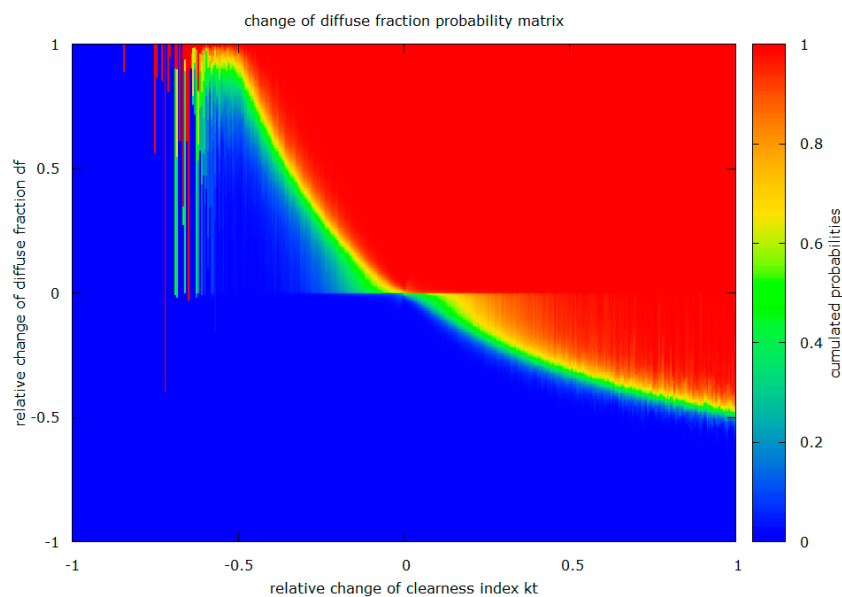


Figure 6. The same relation between changes of df and changes of kt as in Figure 5, here as the probability matrix that is used in the model, corresponding to Figure 4. In the model, only relative kt changes of -0.5 to 1 are computed with this matrix. In the matrix shown here, measurement values from the same locations and years as in Figure 4 were incorporated.

3.3. Part Three. Geometric Calculation for Days with Clear Sky

3.3.1. Calculation of the Daily Course of df

In the case of clear sky, df is mainly dependent on the air mass relative to its daily minimum. For that reason, in this part of the model a geometric approach has been chosen capable of reproducing the characteristic daily course of the diffuse fraction for clear sky days. The diffuse fraction of this part is calculated as:

$$df_3 = \frac{AM}{AM_{\min}} df_{\min} \quad (9)$$

The air mass can be modelled as a function of the elevation of the sun. The minimal air mass AM_{\min} is calculated for each day by using the maximum elevation angle $\gamma_{S, \max}$:

$$AM_{(\min)} = \frac{1}{\sin(\gamma_{S,(\max)})^{1.15}} \quad (10)$$

Figure 7 displays the measured (blue) and modelled (green dashed) course of the diffuse fraction over an exemplary day in Tateno, Japan (13 February 2006). While the clearness index kt (black) is relatively stable around 1, the diffuse fraction is around 0.5 shortly after sunrise and before sunset and is falling down to a minimal diffuse fraction df_{\min} at noon, to 0.136 in this example.

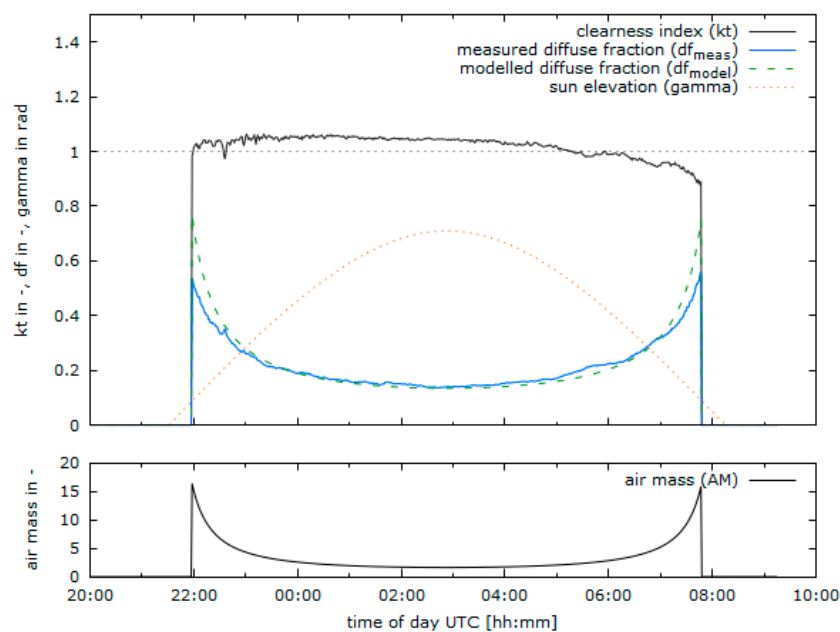


Figure 7. Example for the geometric approach used to model clear sky diffuse fraction. The data shown is from Tateno, Japan, for 13 February 2006. While kt (**top** plot, black) remains relatively constant, the measured diffuse fraction (blue) follows a typical scheme, starting with high df values in the morning, falling to a minimum at noon and rising again in the evening. This behaviour shows a strong correlation with the change of the air mass during the day (**bottom** plot, black). The clear sky diffuse fraction (green) is modelled as presented in Equation (9). The most important factor in this part of the model is the smallest value of df during the day, df_{\min} . Modelling df_{\min} correctly is crucial for good algorithm results.

However, the main challenge in modelling the diffuse fraction over the course of a clear sky day is to find a good approximation for the minimal diffuse fraction of the day, since this factor is subject to strong variations in every possible respect: from location to location, from season to season and even from day to day.

3.3.2. Daily Variation of df_{\min}

In order to illustrate the daily variation of df_{\min} , seven consecutive days in Tamanrasset, Algeria, are shown in Figure 8. Even for this non-cloudy site df_{\min} may vary significantly from day to day: The minimal value of the diffuse fraction (grey, bottom plot) of each day is varying between 0.328 on the first day (21 March 2006) and 0.062 on the third day (23 March 2006).

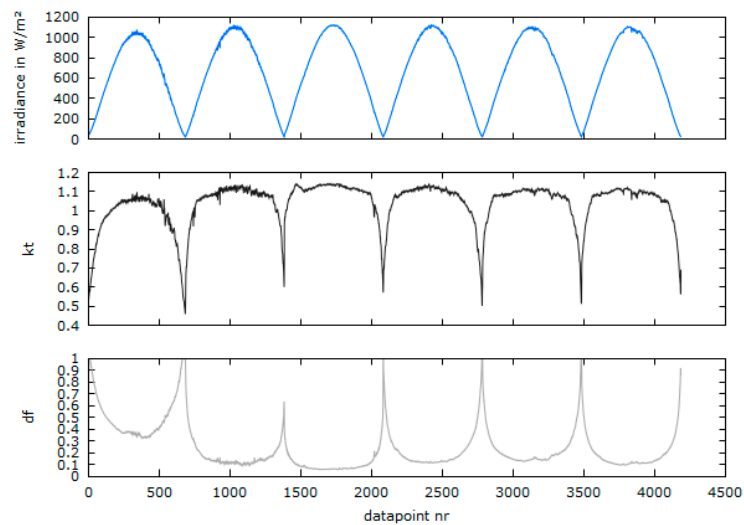


Figure 8. Measurement values for global irradiance (blue, **top**), kt (black, **center**) and df (grey, **bottom**) for Tamanrasset, Algeria, from 21 to 26 March 2006. This plot illustrates the variation of the minimum daily df value (df_{\min}) for consecutive clear sky days. df_{\min} values for March 21 to 26 are: 0.328, 0.101, 0.062, 0.123, 0.139 and 0.105. One factor of influence seems to be the averaged maximum value of kt around noon. Another indicator is the shape of the kt curve during day: A slow rise of kt in the morning and slow fall in the evening indicate a high df_{\min} like on 21 March, whereas steep ramps in the morning and evening with flat trends during the day indicate low df_{\min} value (e.g., 26 March).

3.3.3. Seasonal Variation of df_{\min}

In addition to daily variations, df_{\min} also shows seasonal variation on some locations. Figure 9 displays the minimal diffuse fractions of all clear days in Tamanrasset, Algeria, in 2006 (black plus symbols) over the course of a year. While in wintertime df_{\min} ranges mostly between 0.05 and 0.15, it almost never falls below 0.1 in summertime and features values between 0.15 and 0.5. When looking at the daily mean kt values (grey crosses), no significant correlation can be observed which implies that other factors must have influence on the minimal daily diffuse fraction. The monthly means of aerosol optical depth (red) and the water vapor (blue dashed) taken from the NASA Terra/MODIS satellite [29,30] however feature a seasonal behavior similar to df_{\min} .

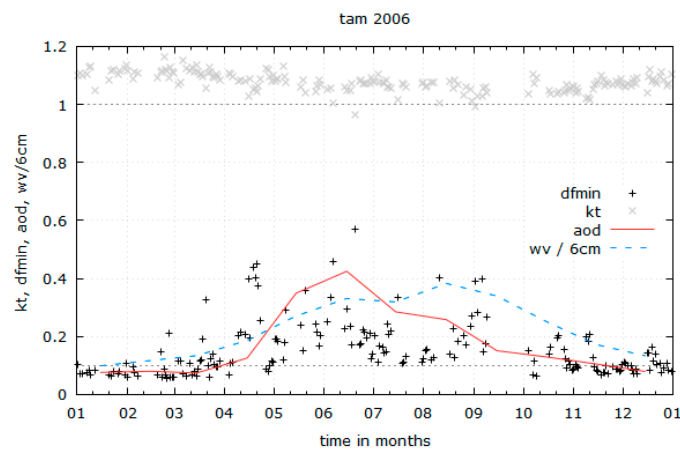


Figure 9. Variation of df_{\min} (black) of days with clear skies over a year in Tamanrasset, 2006. While df_{\min} is mostly close to 0.1 in wintertime, it varies strongly from spring to autumn, with no clear relation to the mean clearness index of the corresponding day (grey). It was found that changing levels of aerosols (red) and water vapour (dotted blue) may cause this effect.

3.3.4. Summary of Factors Influencing df_{\min}

This leads to the conclusion that df_{\min} is dependent on a series of factors. A list of factors that proved influential on df_{\min} is given below:

- (1) The clearness index kt . The values of kt are averaged in a range of 120 min around noon:

$$\overline{kt} = \frac{1}{t_{\text{range}}} \sum_{i=t_{\text{noon}} - \frac{t_{\text{range}}}{2}}^{t_{\text{noon}} + \frac{t_{\text{range}}}{2}} kt_i \quad (11)$$

- (2) The variability of the clearness index, kt_{Var} . For the same period of time, the changes of kt are registered:

$$kt_{\text{Var}} = \sum_{i=t_{\text{noon}} - \frac{t_{\text{range}}}{2}}^{t_{\text{noon}} + \frac{t_{\text{range}}}{2}} \left| \frac{kt_i}{kt_{i-1}} - 1 \right| \quad (12)$$

- (3) The maximum elevation of the sun during the day, $\gamma_{S,\text{max}}$ and the minimum air mass during the day, AM_{\min} , compare to top of this section.
- (4) The aerosol optical depth (AOD) and the water vapour (wv) of the respective month. These values are taken from the NASA Terra/MODIS satellite [29,30] and averaged on a month per month basis between 2001 and 2015. Figure 10 gives an impression of the worldwide seasonal characteristics of AOD and wv.
- (5) The up and down time of kt in the morning and in the evening. As a measure of the steepness of the kt curve, the time span is determined between sunrise and when kt first reaches the threshold of 1 in the morning. A second time span between the moment when kt is at last above 1 in the evening and sunset is measured as well. The two values are averaged and are a good indicator for df_{\min} in places with high day-to-day variation of df_{\min} : The longer the up/down time, the higher df_{\min} will be.

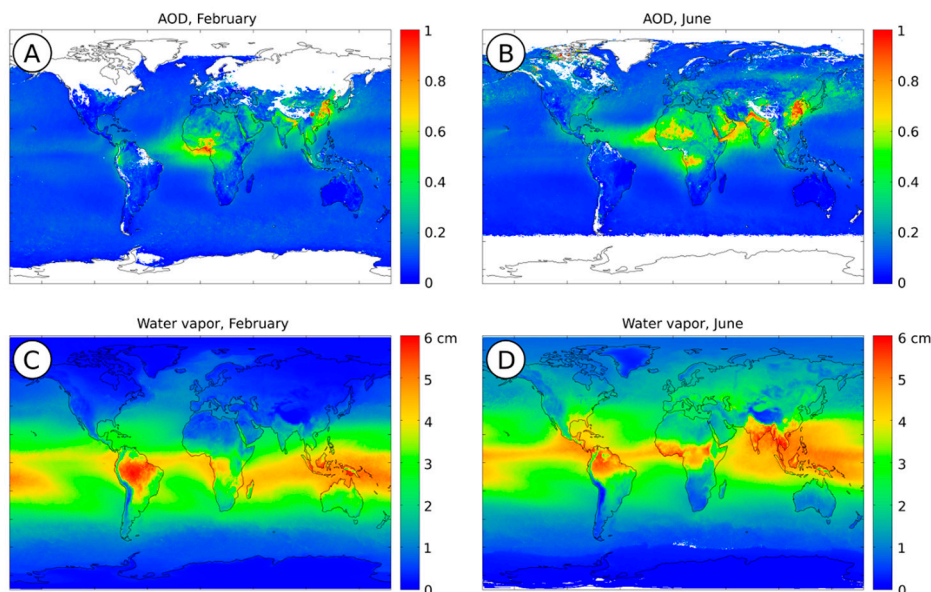


Figure 10. Monthly means of aerosol optical depth (AOD) (plots A and B) and water vapour (C,D) for February (A,C) and June (B,D), from 2001 to 2015. Data taken from NASA Terra/MODIS satellite [29,30].

3.3.5. Resulting Equations for df_{\min}

The factors that influence df_{\min} mentioned in the above section are combined in a series of posynomials, depending on the location and availability of data. The coefficients and exponents

of the following posynomials were fitted with the help of the Levenberg-Marquardt algorithm implementation of the software gnuplot 5.0 [31].

The datasets used for the posynomial fits are taken from the same locations as in Table 2, but for different years of measurement: *asp 2009, bil 2005, bou 2010, brb 2011, cab 2011, cam 2002, clh 2014, cnr 2010, coc 2007, daa 2003, dar 2010, fua 2013, gob 2013, iza 2010, lau 2007, ler 2002, lin 2002, pal 2010, pay 2010, reg 2011, sap 2013, sbo 2011, sms 2006, sov 2002, tam 2003, tat 2003, tor 2005, xia 2006*. For Case 1 only the subset *bou 2010, iza 2010, sbo 2011, sov 2002, tam 2003* and *xia 2006* was used.

Case 1: AOD and water vapor data available, location features strong seasonal changes of AOD (indicator for seasonal aerosol concentrations e.g., due to sandstorms in desert regions, see Table 3 the values for factors *a*, *b* and *c*).

$$df_{\min} = a_0 kt^{b_0} + a_1 kt_{\text{var}}^{b_1} + a_2 AM^{b_2} + a_3 AOD^{b_4} + a_4 wv^{b_4} + a_5 t_{\text{up/down}}^{b_5} + c \quad (13)$$

Table 3. Values for *a*, *b* and *c* factors of the df_{\min} fit, used to model df_{\min} for given *kt*, kt_{var} , AM, AOD, water vapour and up/down time. The RMS of residuals is 0.0528.

Factors	0	1	2	3	4	5
<i>a</i>	−4.29127	0.09656	−1.26822	0.05940	−0.30991	0.00043
<i>b</i>	0.19589	0.93797	0.03795	1.48181	0.08588	0.79801
<i>c</i>	6.01645	-	-	-	-	-

Case 2: AOD and water vapor data available, no strong seasonal changes of AOD (see Table 4 the values for factors *a*, *b* and *c*).

$$df_{\min} = a_0 kt^{b_0} + a_1 kt_{\text{var}}^{b_1} + a_2 AM^{b_2} + a_3 AOD^{b_4} + a_4 wv^{b_4} + a_5 t_{\text{up/down}}^{b_5} + c \quad (14)$$

Table 4. Values for *a*, *b* and *c* factors of the df_{\min} fit, used to model df_{\min} for given *kt*, kt_{var} , AM, AOD, water vapour and up/down time. The RMS of residuals is 0.0427.

Factors	0	1	2	3	4	5
<i>a</i>	−2.49013	0.08345	0.00673	0.14107	−0.05853	0.00158
<i>b</i>	0.15065	0.72204	2.25298	0.75615	0.37413	0.67690
<i>c</i>	2.58895	-	-	-	-	-

Case 3: AOD and water vapor data are not available (see Table 5 the values for factors *a*, *b* and *c*):

$$df_{\min} = a_0 kt^{b_0} + a_1 kt_{\text{var}}^{b_1} + a_2 AM^{b_2} + a_5 t_{\text{up/down}}^{b_5} + c \quad (15)$$

Table 5. Values for *a*, *b* and *c* factors of the df_{\min} fit, used to model df_{\min} for given *kt*, kt_{var} , AM and up/down time. The RMS of residuals is 0.0480.

Factors	0	1	2	3	4	5
<i>a</i>	−0.75568	0.10744	0.02533	-	-	0.01203
<i>b</i>	0.16313	0.58318	1.26937	-	-	0.45174
<i>c</i>	0.71854	-	-	-	-	-

Case 4: AOD, water vapor and up/down time data are not available (see Table 6 the values for factors *a*, *b* and *c*).

$$df_{\min} = a_0 kt^{b_0} + a_1 kt_{\text{var}}^{b_1} + a_2 AM^{b_2} + c \quad (16)$$

Table 6. Values for a , b and c factors of the df_{\min} fit, used to model df_{\min} for given kt , kt_{var} , AM and up/down time. The RMS of residuals is 0.0542.

Factors	0	1	2	3	4	5
a	-2.28942	0.23589	0.02445	-	-	-
b	0.27308	0.19371	1.26262	-	-	-
c	2.23274	-	-	-	-	-

3.4. Combination of the Three Parts

The three parts of the algorithm generate the values df_1 , df_2 and df_3 . Depending on the current weather situation, expressed by characteristics and statistical features of kt , they are combined to one single, resulting df :

$$df = w_1df_1 + w_2df_2 + w_3df_3 \tag{17}$$

The mean absolute deviation of kt at a given time of day t_x that is used as condition above is calculated as follows:

$$mad_{kt} = \frac{1}{t_{\text{range}}} \sum_{i=t_x-t_{\text{range}}}^{t_x} \left| \frac{kt_i}{kt_{i-1}} - 1 \right| \tag{18}$$

with $t_{\text{range}} = 30$ min. For illustration of the weighing conditions mentioned in Table 7, Figure 11 displays all-sky camera images from the Institute of Meteorology and Climatology of the Leibniz University Hannover [32,33]. Picture A shows a moment where no clouds are visible. It is classified as “Clear Sky” since $kt = 1.03$ and $mad_{kt} = 0.0025$. Picture B shows a moment where $kt = 0.147$ and $mad_{kt} = 0.107$, hence being classified as “Standard”. In picture C some light clouds are visible around the sun. This moment is classified as “Transition” as $kt = 1.01$ and $mad_{kt} = 0.028$. The “Transition” condition can be interpreted as clear sky with only few light clouds.

The generated matrices and other model data can be obtained from the authors upon request.

Table 7. Weighing factors for the combination of df_1 , df_2 and df_3 to one single df , depending on kt characteristics.

Name	Condition	w_1	w_2	w_3
Clear Sky	$mad_{kt} < mad_{kt, \text{lower}}$ $kt_{\text{clear, lower}} < kt < kt_{\text{clear, upper}}$	0	0.2	0.8
Transition	$mad_{kt, \text{lower}} < mad_{kt} < mad_{kt, \text{upper}}$ $kt_{\text{clear, lower}} < kt < kt_{\text{clear, upper}}$	0.2	0.2	0.6
Standard	Else	0.2	0.8	0

With $kt_{\text{clear, lower}} = 0.95$, $kt_{\text{clear, upper}} = 1.2$, $mad_{kt, \text{lower}} = 0.005$ and $mad_{kt, \text{upper}} = 0.05$.

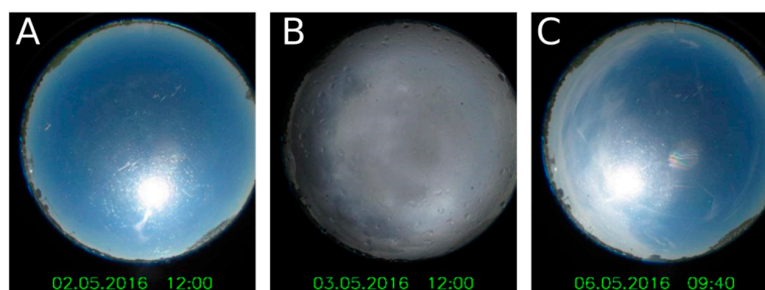


Figure 11. Three pictures made by an Hemispherical Sky Imager in Hannover (at the Institute for Meteorology and Climatology of the Leibniz University Hannover) in order to illustrate the three different weighing conditions presented in Table 7. Time in UTC. (A) 02 May 2016 12:00–Clear Sky: $kt = 1.03$, $mad_{kt} = 0.0025$; (B) 03 May 2016 12:00–Standard: $kt = 0.147$, $mad_{kt} = 0.107$; (C) 06 May 2016 09:40–Transition: $kt = 1.01$, $mad_{kt} = 0.028$.

4. Results

In this section, the results of the validation of the new algorithm are presented. As mentioned in Section 2.1, the validation is conducted for 28 locations with one year of one-minute values each, basing the validation on more than seven million data points worldwide.

The overall results are then compared to the results of three existing models for the diffuse fraction: the model of Orgill and Hollands [18] (OH), a one-parameter model, the reduced version of the two-parameter model of Reindl et al. [3] (RR), and the model by Perez and Ineichen [23] (PZ), all introduced in Section 2.3. The first two models were also identified as two of the three best performing models among the eight investigated approaches by Dervishi [27]. The model by Perez and Ineichen [23] is still popular in the community and widely made use of. The model by Skartveit [12] was not used for the model comparison since no indications were found that show a significant advantage of this model over Orgill and Hollands [18], Reindl et al. [3] or Perez and Ineichen [23].

Figure 12 displays two weeks in Alice Springs, Australia, 2005. The measured global horizontal irradiance is plotted on top (green); the resulting clearness index kt is plotted for reference underneath (black). In the three following plots, the measured diffuse fraction (black) is displayed, together with the diffuse fraction that was modelled with the new approach (blue), with the model from Orgill and Hollands [18] (grey), the model from Reindl et al. [3] (orange) and the model from Perez and Ineichen [23].

While the new model is able to reproduce the diffuse fraction in good accordance to the measurement values most of time, the inherent problem of models with static one- or two-parameter relationships between the clearness index and the diffuse fraction becomes apparent. Especially on clear sky days the existing models fail to reproduce the characteristic behavior of the diffuse fraction.

In order to evaluate the performance of the new model in statistical terms, the root mean squared errors (RMSEs) are calculated for the new model as well as for the three reference models. Figure 13 shows the RMSE for the four models over all test data sets. The RMSE produced by the new model is smaller than those produced by the models of Orgill and Hollands [18], Reindl et al. [3] and Perez and Ineichen [23], in parts significantly, except for one case in Izaña, Spain, 2011 (*iza 2011*). The overall RMSE, averaged over all test data sets, can be reduced from 0.138 (OH), 0.134 (RR) and 0.139 (PZ) to 0.116 for the new model, which equals an amelioration of 16%–20%.

A further validation is conducted by comparing the annual diffuse irradiation values that are estimated by the models with the measured value. Figure 14 lists the relative deviations of the modelled from the measured annual diffuse irradiation. In most of the cases, the deviation resulting from the new model is significantly smaller than the deviation resulting from the models of OH, RR or PZ. There are few cases where the model leads to higher deviations than the existing ones, e.g., for Billings, USA (*bil 2003*), Solar Village, Saudi Arabia (*sov 2001*) or Tamanrasset, Algeria (*tam 2006*). Extreme deviations of more than 20%, however, as apparent in some of the test cases for the two existing models, do not occur when using the new model. The average of the absolute (i.e. unsigned) relative deviations for all test cases can be reduced by nearly 50% from 11.9% for OH, 12.7% for RR and 10.9% for PZ to only 6.4% for the new model.

The histogram of the mean absolute deviations of the annual diffuse irradiation displayed in Figure 15 illustrates the frequency of the deviations each model produces. While the model of Reindl et al. [3] (RR) has its peak in the class of 0 to 5%, it still has several outliers of 35%–55%. The model of Orgill and Hollands [18] (OH) features only one extreme outlier at 35%–40%, but has most of its results lying in the class of 10 to 15%. The model by Perez and Ineichen [23] shows no outliers of more than 25% but has its results evenly distributed between 0 and 15%. The new model does not produce any outliers and has its peak in the class of 0%–5%, covering 50% of the test cases alone.

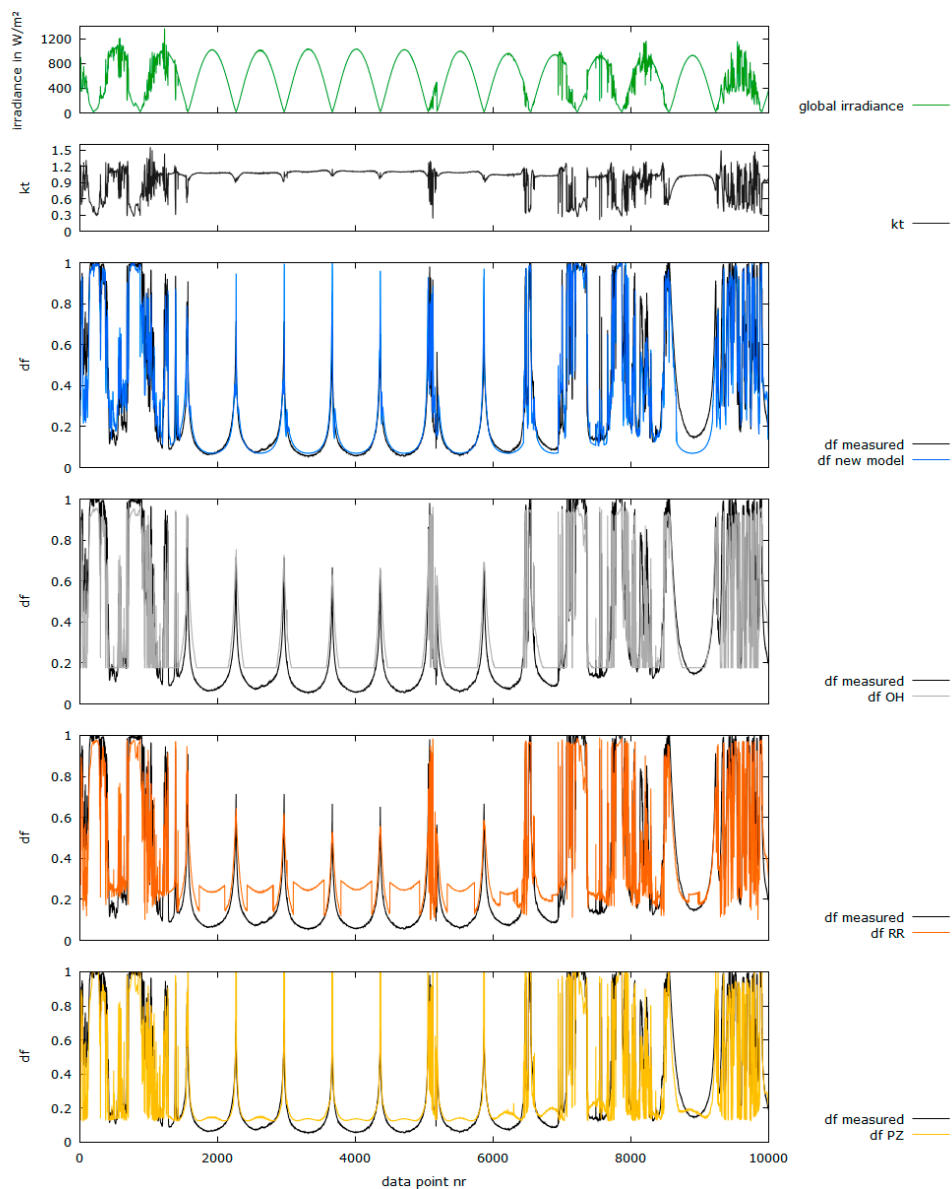


Figure 12. Plot of measured and modelled irradiance values for 14 consecutive days in Alice Springs, Australia, 2005, as an example. The total amount of analysed data sets comprises one year in minutes for each of the 28 test cases (refer to Section 2.1), equaling to seven million datapoints. Values at night are omitted in this plot. The measured global irradiance (green) is shown on top, the resulting clearness index kt (black) for reference in the middle. The bottom part of the diagram displays measured (black) and modelled diffuse fractions (blue for the new model, grey for Orgill and Hollands [18], orange for Reindl et al. [3], yellow for Perez and Ineichen [23]). Most of the time, the output of the new model leads to good conformity for clear sky days as well as for days with broken clouds. The inherent problem of static one- or two-parameter models becomes apparent when comparing the measurement values to the output of the models by Orgill and Hollands [18], Reindl et al. [3] and Perez and Ineichen [23], especially for clear sky days.

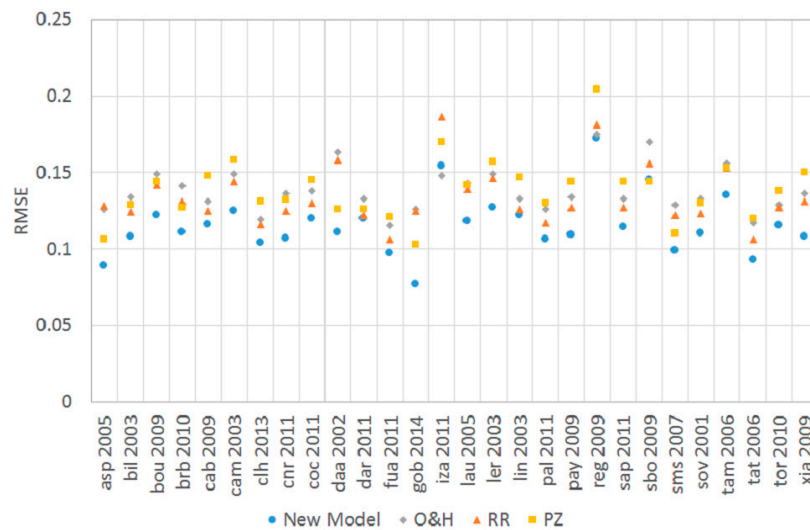


Figure 13. The root mean squared errors (*RMSE*) for all analysed datasets of the modelled versus the measured diffuse fraction. The *RMSE* of the new model is in all cases smaller than the *RMSE* of the model by Orgill and Hollands [18] (OH, grey), Reindl et al. [3] (RR, orange) or Perez and Ineichen [23] (PZ, yellow), except for the location of Izaña, Spain (*iza 2011*), where the OH model produces a slightly smaller *RMSE*. The mean *RMSE* over all test cases is at 0.116 for the new model, 0.138 for OH, 0.134 for RR and 0.139 for PZ, which implies an amelioration of the *RMSE* of 16%–20%.

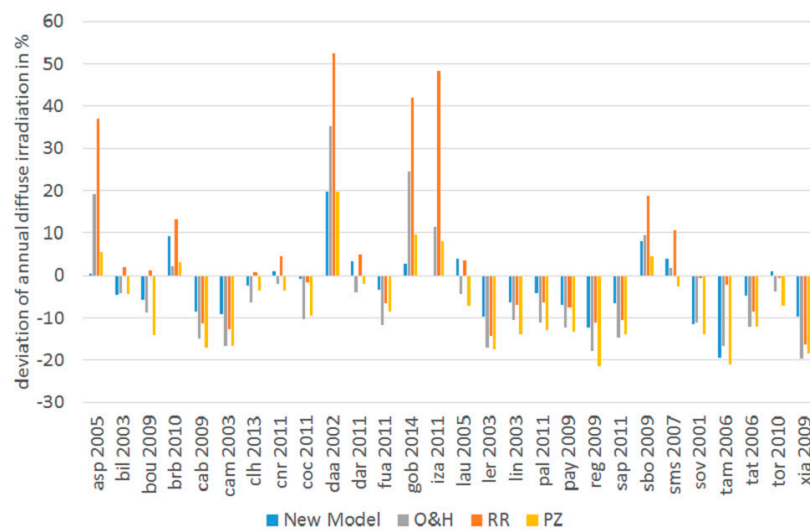


Figure 14. Relative deviation of the modelled annual diffuse irradiation from the measured diffuse irradiation for all analysed datasets. The new model performs better than the three reference models by Orgill and Hollands [18] (OH, grey), Reindl et al. [3] (RR, orange) and Perez and Ineichen [23] in nearly all cases, except for desert-like locations such as Solar Village, Saudi Arabia (*sov*) or Tamanrasset, Algeria (*tam*). None of the test cases shows deviations of more than $\pm 20\%$ for the new model. The mean absolute deviation over all test cases for the new model is 6.4%, whereas it reaches 11.9% for OH, 12.7% for RR and 10.9% for PZ. The mean absolute deviation can thus approximately be halved when using the new model.

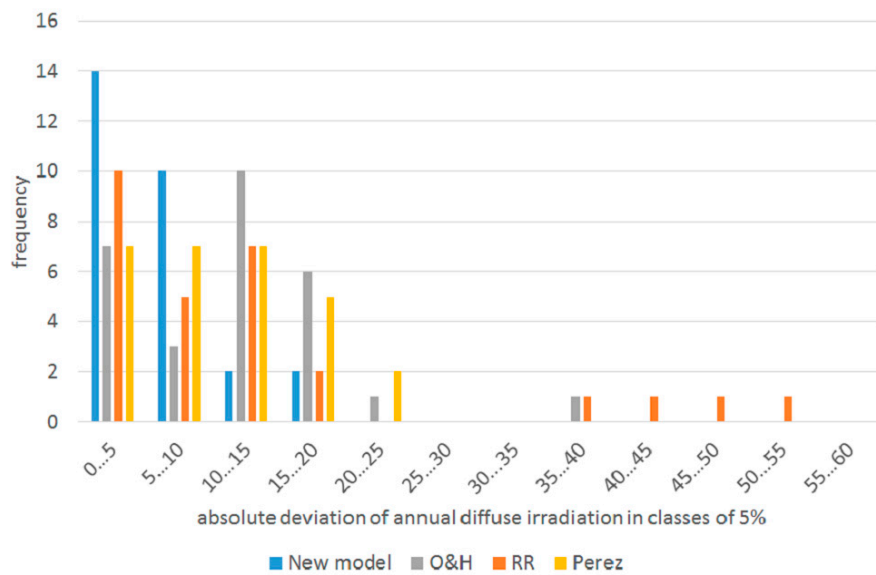


Figure 15. Histogram of the mean absolute deviations of the annual diffuse irradiation in classes of 5%. Most of the deviations produced by the new model are smaller than 10% (compare Figure 16). In none of the test cases deviations of more than 20% can be observed. While the model by Reindl et al. [3] (RR, orange) has most of its test cases in classes <15%, it still produces in some cases results of more than 40%. The model of Orgill and Hollands [18] (OH, grey) features less extreme deviations but shows a strong frequency of deviations between 10% and 20%. The model by Perez and Ineichen [23] (PZ, yellow) does not produce outliers and has its results distributed evenly between 0 and 15%.

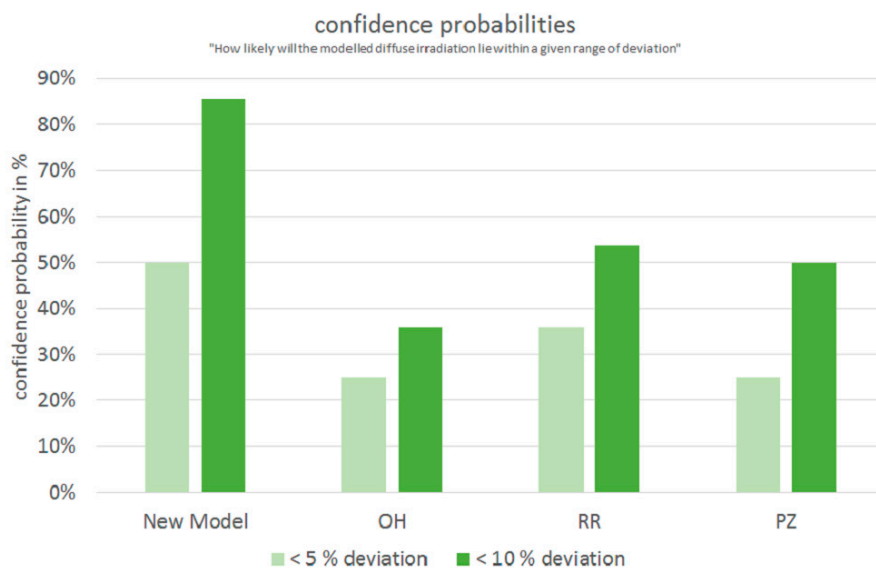


Figure 16. When using the new model for calculating the diffuse irradiance, the annual deviation of the modelled irradiation will be smaller than 5% in more than 40% of the cases, and smaller than 10% in over 80% of the cases. When using the model of Orgill and Hollands [18] (OH), these confidence probabilities reduce to 25% and 36%, while using the model of Reindl et al. [3] (RR) reduces the probabilities to 36% and 54% respectively. The use of the model of Perez and Ineichen [23] (PZ) results in probabilities of 25% and 50%.

This histogram can be converted into confidence probabilities, depicted in Figure 16. The new model results in mean absolute deviations of less than 5% in 50% of the cases. In more than 80% of the cases, the deviation is less than 10%. Compared to the other three models this is a significant

improvement, where the probability of producing less than 5% deviation is only 25% (OH), 36% (RR) and 25% (PZ) and the probability of producing less than 10% deviation is 36% (OH), 54% (RR) and 50% (PZ).

5. Conclusions

The newly developed model for the diffuse fraction of solar irradiance on PV systems provides significantly better agreement with measurements than the other models published so far. This is achieved by the following features: the first part utilizes the dependency of the diffuse fraction df on the clearness index kt , in analogy to existing one-parameter models. In the new model, the correlation is expressed as probability matrices rather than single functions, leading to realistic, more natural diffuse fraction characteristics. Also taking advantage of probability matrices, the second part uses the relation of the relative changes of df over the relative changes of kt . The third part takes into account the diffuse fraction characteristics of days with clear sky only using a geometrical approach. The crucial factor for the third part is the minimum daily diffuse fraction for which a posynomial model has been introduced.

The presented new model was analyzed and compared to two other models for 28 locations worldwide with one year of one-minute measurement data each. It was shown that the new model has a high quality of modeling the diffuse irradiance. The mean *RMSE* over all test cases was reduced by 16%–20%, whereas the mean absolute deviation of the annual diffuse irradiation was found to be nearly 50% smaller compared to the reference models. In more than 80% of the test cases, the deviation of the annual diffuse irradiation is smaller than 10%, with an overall maximum deviation of 20%.

With the new model, the diffuse irradiance can be calculated with much lower uncertainty, hence significantly reducing the uncertainty of PV energy yield simulations. Possible future work for the improvement of the model will include further investigations on the minimal daily diffuse fraction that has a very decisive influence on the model quality for clear sky days. Such days may be identified by cloud cameras that will allow for a much better estimation of the cloud fraction compared to satellite images [33].

Acknowledgments: The publication of this article was funded by the Open Access Fund of the Leibniz Universität Hannover.

Author Contributions: The research and development of the algorithm, as well as the algorithm comparisons and the writing of the paper was conducted by Martin Hofmann. Gunther Seckmeyer gave valuable input to former work on the topic (see Section 2.3), discussed the results and revised the manuscript critically.

Conflicts of Interest: The authors declare no conflict of interest.

References

1. Spencer, J.W. A comparison of methods for estimating hourly diffuse solar radiation from global solar radiation. *Solar Energy* **1982**, *29*, 19–32. [CrossRef]
2. König-Langlo, G.; Sieger, R. *Report of the 12th Baseline Surface Radiation Network (BSRN) Scientific Review and Workshop*; WCRP Report No. 20/2012; Alfred Wegener Institute (AWI): Potsdam, Germany, 1–3 August 2012.
3. Reindl, D.T.; Beckman, W.A.; Duffie, J.A. Diffuse fraction correlations. *Solar Energy* **1990**, *45*, 1–7. [CrossRef]
4. Hay, J.E.; Davies, J.A. Calculations of the solar radiation incident on an inclined surface. In *Proceedings—First Canadian Solar Radiation Data Workshop*; Hay, J.E., Won, T.K., Eds.; Ministry of Supply and Services Canada: Ottawa, ON, Canada, 1980; p. 59.
5. PV*SOL 2017 R5. Valentin Software GmbH, Berlin, Germany. 2016. Software. Available online: <http://www.valentin-software.com> (accessed on 21 December 2016).
6. Feldman, D.; Bolinger, M. *On the Path to SunShot: Emerging Opportunities and Challenges in Financing Solar*; NREL/TP-6A20-65638; National Renewable Energy Laboratory: Golden, CO, USA, 2016.
7. Köppen, W. Klassifikation der Klimate nach Temperatur, Niederschlag und Jahreslauf. *Petermanns Geogr. Mitt.* **1918**, *64*, 193–203, 243–248.

8. Reda, I.; Andreas, A. Solar position algorithm for solar radiation applications. *Solar Energy* **2004**, *76*, 577–589. [[CrossRef](#)]
9. Bourges, G. *Reconstitution Des Courbes de Fréquence Cumulées de L'irradiation Solaire Globale Horaire Reçue Par Une Surface Plane*; Report CEE 295-77; ESF of Centre d'Energétique de l'Ecole Nationale Supérieure des Mines de Paris, Tome II: Paris, France, 1979. (In French)
10. Maxwell, E.L. A Quasi-Physical Model for Converting Hourly Global Horizontal to Direct Normal Insolation. Available online: <http://redc.nrel.gov/solar/pubs/PDFs/TR-215-3087.pdf> (accessed on 21 December 2016).
11. Hofmann, M.; Riechelmann, S.; Crisosto, C.; Mubarak, R.; Seckmeyer, G. Improved synthesis of global irradiance with one-minute resolution for PV system simulations. *Int. J. Photoenergy* **2014**, *2014*, 808509. [[CrossRef](#)]
12. Skartveit, A.; Olseth, J. A model for the diffuse fraction of hourly global radiation. *Solar Energy* **1987**, *38*, 271–274. [[CrossRef](#)]
13. Nack, M.; Green, A. Influence of clouds, haze, and smog on the middle ultraviolet reaching the ground. *Appl. Opt.* **1974**, *13*, 2405–2415. [[CrossRef](#)] [[PubMed](#)]
14. Seckmeyer, G.; Mayer, B.; Bernhard, G.; Erb, R.; Albold, A.; Jäger, H.; Stockwell, W.R. New maximum UV irradiance levels observed in Central Europe. *Atmos. Environ.* **1997**, *31*, 2971–2976. [[CrossRef](#)]
15. Liu, B.; Jordan, R. The interrelationship and characteristic distribution of direct, diffuse and total solar radiation. *Solar Energy* **1960**, *4*, 1–19. [[CrossRef](#)]
16. Carroll, J.J. Global transmissivity and diffuse fraction of solar radiation for clear and cloudy skies as measured and as predicted by bulk transmissivity models. *Solar Energy* **1985**, *35*, 105–118. [[CrossRef](#)]
17. Zernikau, F. Vergleich und Bewertung von Diffusstrahlungsmodellen. Master's Thesis, Institut für Energietechnik, Technical University of Berlin, Berlin, Germany, 2015.
18. Orgill, J.F.; Hollands, K.G.T. Correlation equation for hourly diffuse radiation on a horizontal surface. *Solar Energy* **1976**, *19*, 357–359. [[CrossRef](#)]
19. Erbs, J.A.; Klein, S.A.; Duffie, J.A. Estimation of the diffuse radiation fraction for hourly, daily and monthly average global radiation. *Solar Energy* **1982**, *18*, 293–302. [[CrossRef](#)]
20. Boland, J.; Ridley, B. Modelling of diffuse solar fraction with multiple predictors. *Renew. Energy* **2010**, *35*, 478–483.
21. Oliveira, A.; Escobedo, J.; Machado, A.; Soares, J. Correlation models of diffuse solar-radiation applied to the city of São Paulo, Brazil. *Appl. Energy* **2002**, *71*, 59–73. [[CrossRef](#)]
22. Furlan, C.; Oliveira, A.; Soares, J.; Codato, G.; Escobedo, J. The role of clouds in improving the regression model for hourly values of diffuse solar radiation. *Appl. Energy* **2012**, *92*, 240–254. [[CrossRef](#)]
23. Perez, R.; Ineichen, P.; Maxwell, E.; Seals, R.; Zelenka, A. Dynamic global-to-direct irradiance conversion models. *ASHRAE Trans. Res. Ser.* **1992**, *98*, 354–369.
24. Kambezidis, H.D.; Psiloglou, B.E.; Gueymard, C. Measurements and models for total solar irradiance on inclined surface in Athens, Greece. *Solar Energy* **1994**, *53*, 177–185. [[CrossRef](#)]
25. Jacovides, C.; Tymvios, F.; Assimakopoulos, V.; Katsounides, N. Comparative study of various correlations in estimating hourly diffuse fraction of global solar radiation. *Renew. Energy* **2006**, *31*, 2492–2504. [[CrossRef](#)]
26. Wong, L.T.; Chow, W.K. Solar radiation model. *Appl. Energy* **2001**, *69*, 191–224. [[CrossRef](#)]
27. Dervishi, S.; Mahdavi, A. Computing diffuse fraction of global horizontal solar radiation: A model comparison. *Solar Energy* **2012**, *86*, 1796–1802. [[CrossRef](#)] [[PubMed](#)]
28. Markov, A. *Extension of the Limit Theorems of Probability Theory to a Sum of Variables Connected in a Chain. Appendix B of: Howard R. Dynamic Probabilistic Systems, 1: Markov Chains*; John Wiley and Sons: New York, NY, USA, 1971.
29. MODIS Atmosphere L2 Water Vapor Product. Available online: http://modis-atmos.gsfc.nasa.gov/MOD05_L2/doi.html (accessed on 21 December 2016).
30. Levy, R.; Hsu, C. *MODIS Atmosphere L2 Aerosol Product*; NASA MODIS Adaptive Processing System; Goddard Space Flight Center: Greenbelt, MD, USA, 2015.
31. Williams, T.; Kelley, C. Gnuplot 5, An Interactive Plotting Program. Available online: <http://www.gnuplot.info/> (accessed on 21 December 2016).

32. Tohsing, K.; Schrepf, M.; Riechelmann, S.; Seckmeyer, G. Validation of spectral sky radiance derived from all-sky camera images—A case study. *Atmos. Meas. Tech.* **2014**, *7*, 2137–2146. [[CrossRef](#)]
33. Werkmeister, A.; Lockhoff, M.; Schrepf, M.; Tohsing, K.; Liley, B.; Seckmeyer, G. Comparing satellite- to ground-based automated and manual cloud coverage observations—A case study. *Atmos. Meas. Tech.* **2015**, *8*, 2001–2015. [[CrossRef](#)]



© 2017 by the authors; licensee MDPI, Basel, Switzerland. This article is an open access article distributed under the terms and conditions of the Creative Commons Attribution (CC BY) license (<http://creativecommons.org/licenses/by/4.0/>).

3.3 Influence of meteorological models on PV system simulations

The model chain used for PV system simulations is outlined in 2.1. For each model block presented there exists a number of approaches that vary highly in their quality and how intensely they were validated over time. All of these models influence the output of the PV system simulation directly, but so far it was unclear how deviations of a single model propagate through the model chain and how the interplay and various combinations of models interfere with each other.

In general, the influence of the selection of irradiance models on the simulated electrical output of a PV system is not very well analyzed and documented. The importance of high resolution irradiance data input was highlighted already in the first publication of this thesis and before that by [51] and [52]. Balafas [73] presented a study on the diffuse irradiance on the inverter output of a PV system. Some studies have been published that analyze the effect of various combinations of decomposition and transposition models on the irradiance on the tilted plane, e.g. for Aldergrove (Northern Ireland) [74], Corsica (France) [75] or Valladolid (Spain) [76], but they rely on measurement data with one-hour resolution and for one location only.



In order to cope with this situation and shed some light on the matter, the third publication of this thesis presents a matrix simulation approach, where eight selected diffuse fraction models, along with measured diffuse irradiance values, 5 transposition models, two sun position models and three types of time resolution (measured one-minute values, hourly averages and synthesized one-minute values) were cross combined to build 270 different model chains for 30 different locations from the BSRN dataset. The PV simulations were furthermore repeated for three different module tilt or tracking modes, totaling in 24300 simulations.

To further analyze the importance of high resolution data, a study of inverter clipping losses and their dependence on the simulation time step is included.

It is shown that the quality for both decomposition and transposition models varies strongly from location to location. The modelled PV energy output varies between -5% and $+8\%$ for PV systems with a fixed module inclination and between -26% and $+14\%$ for modules with two-axis tracking. It is demonstrated that the usage of the new diffuse model leads to the smallest variability in the results. The necessity to use one-minute time series for PV simulations is highly indicated by the results, especially with regard to the inverter clipping losses.

Article

Influence of Various Irradiance Models and Their Combination on Simulation Results of Photovoltaic Systems

Martin Hofmann ^{1,2,*}  and Gunther Seckmeyer ² 

¹ Valentin Software GmbH, Stralauer Platz 34, 10243 Berlin, Germany

² Institute for Meteorology and Climatology, Leibniz Universität Hannover, Herrenhäuser Straße 2, 30419 Hannover, Germany; seckmeyer@muk.uni-hannover.de

* Correspondence: martin.hofmann@valentin-software.com; Tel.: +49-30-588-4390

Academic Editor: Senthilarasu Sundaram

Received: 10 August 2017; Accepted: 31 August 2017; Published: 26 September 2017

Abstract: We analyze the output of various state-of-the-art irradiance models for photovoltaic systems. The models include two sun position algorithms, three types of input data time series, nine diffuse fraction models and five transposition models (for tilted surfaces), resulting in 270 different model chains for the photovoltaic (PV) system simulation. These model chains are applied to 30 locations worldwide and three different module tracking types, totaling in 24,300 simulations. We show that the simulated PV yearly energy output varies between -5% and $+8\%$ for fixed mounted PV modules and between -26% and $+14\%$ for modules with two-axis tracking. Model quality varies strongly between locations; sun position algorithms have negligible influence on the simulation results; diffuse fraction models add a lot of variability; and transposition models feature the strongest influence on the simulation results. To highlight the importance of irradiance with high temporal resolution, we present an analysis of the influence of input temporal resolution and simulation models on the inverter clipping losses at varying PV system sizing factors for Lindenberg, Germany. Irradiance in one-minute resolution is essential for accurately calculating inverter clipping losses.

Keywords: photovoltaics; simulation; irradiation; BSRN; diffuse; diffuse fraction; irradiance; model; transposition; high resolution; tilted; inclined

1. Introduction

Irradiance models are among the most important elements of the complex model chain for simulations of photovoltaic systems. In an ideal case, the irradiance incident on the module plane is measured beforehand in-situ in high resolution, so that this time series can directly be used as an input for the electrical PV simulation. In standard use cases however, only the time series of the global horizontal irradiance in one-hour resolution at the nearest location and the location coordinates are available as input for time-step simulations. The models have to deliver estimates for the sun position, for the diffuse fraction of the horizontal irradiance and, most importantly, for the global irradiance on the plane of the module.

The output of the irradiance processor model chain, the global irradiance on the tilted plane of the PV module, is the most important input parameter for the subsequent model chain that is responsible for the electrical simulation of the modules, as the output current of any PV cell has an approximately linear dependency from the incident irradiance, while the output voltage shows a dependency that resembles logarithmic functions. Hence, the output power of PV modules is almost linearly dependent on the irradiance at moderate to high values, which implies a nearly linear

dependency of the yearly PV energy yield on the irradiation—as the integral of the irradiance over time—on the module surface.

In this study, we want to focus on the irradiance model chain as a whole and systematically analyze the interplay of the different models and their influence on the global tilted irradiance (GTI) and the PV energy as the outputs of the model chain. We use high quality global horizontal irradiance (GHI) measurement data from the Baseline Surface Radiation Network (BSRN) [1] of 30 locations worldwide to estimate the model quality under various conditions. By altering the model chain, we combine all selected models of one category with the all models of the other categories, which leads to a considerable amount of simulations. With this analysis, we are able to answer questions about the importance of choosing the right sun position algorithm, the required temporal resolution or the best model for the diffuse fraction. Additionally, we can make statements about the variability of the simulation results under given conditions.

2. Methodology

2.1. Input Data

To base the analysis on a broad and stable data basis, 30 locations were selected from the Baseline Surface Radiation Network (BSRN) [1], as listed in Table 1. Selection criteria were the availability of one-minute measurement data of global and diffuse horizontal irradiance with a high annual completeness and a latitude between -60° and 60° .

Table 1. Overview of the selected measurement datasets. It comprises 30 locations of the Baseline Surface Radiation Network (BSRN) [1], spread over the whole globe between 60° North and South. Height above sea level, surface, topography and climate zones (according to Köppen [2]) show a high level of variation. The optimal tilt angle for each location is determined according to Section 2.3.

ID (Location and Year)	City, Country	Latitude in $^\circ$ N	Longitude in $^\circ$ E	Height in m	Time Zone	Surface	Climate	Yearly Clearness Index <i>KT</i>	Yearly Diffuse Fraction <i>DF</i>	Optimal Tilt Angle in $^\circ$
ber 2006	Bermuda	32.267	-64.667	8	-4	water, ocean	Cfa	0.53	0.44	25
bou 2009	Boulder, US	40.05	105.007	1577	-7	grass	BSk	0.578	0.367	36
brb 2010	Brasilia, BR	-15.601	-47.713	1023	-3	concrete	Aw	0.574	0.341	22
brb 2011	Brasilia, BR	-15.601	-47.713	1023	-3	concrete	Aw	0.548	0.345	23
cab 2009	Cabauw, NL	51.971	4.927	0	1	grass	Cfb	0.462	0.542	35
car 2014	Carpentras, FR	44.083	5.059	100	1	cultivated	Csa	0.565	0.336	36
chl 2013	Chesapeake Light, US	36.905	-75.713	37	-5	water, ocean	Cfa	0.551	0.383	31
cnr 2011	Cener, ES	42.816	-1.601	471	1	asphalt	Cfb	0.542	0.381	34
daa 2002	De Aar, ZA	-30.667	23.993	1287	2	sand	BSk	0.671	0.195	29
fua 2011	Fukuoka, JP	33.582	130.375	3	9	asphalt	Cfa	0.428	0.532	27
gob 2014	Gobabebe, NA	-23.561	15.042	407	1	n.a.	BWh	0.721	0.188	23
ilo 1997	Ilorin, NG	8.533	4.567	350	1	shrub	Aw	0.498	0.557	9
ish 2011	Ishigakijima, JP	24.337	124.163	5.7	9	asphalt	Cfa	0.439	0.531	12
iza 2011	Izaña, ES	28.309	-16.499	2372.9	0	rock	Csb	0.753	0.201	26
kwa 1999	Kwajalein, MH	8.72	167.731	10	12	water, ocean	Af	0.548	0.387	7
kwa 2005	Kwajalein, MH	8.72	167.731	10	12	water, ocean	Af	0.573	0.399	9
lin 2003	Lindenberg, DE	52.21	14.122	125	1	cultivated	Cfb	0.495	0.471	39
man 2009	Momote, PG	-2.058	147.425	6	10	grass	Af	0.461	0.502	2
mnm 2011	Minamitorishima, JP	24.288	153.983	7.1	9	water, ocean	Af	0.569	0.369	19
nau 2007	Nauru Island, NR	-0.521	166.917	7	12	rock	Af	0.579	0.377	3
nau 2010	Nauru Island, NR	-0.521	166.917	7	12	rock	Af	0.589	0.369	3
pal 2011	Palaiseau, FR	48.713	2.208	156	1	concrete	Cfb	0.481	0.486	35
pay 2009	Payerne, CH	46.815	6.944	491	1	cultivated	Cfb	0.501	0.473	32

Table 1. Cont.

ID (Location and Year)	City, Country	Latitude in ° N	Longitude in ° E	Height in m	Time Zone	Surface	Climate	Yearly Clearness Index <i>KT</i>	Yearly Diffuse Fraction <i>DF</i>	Optimal Tilt Angle in °
reg 2011	Regina, CA	50.205	−104.713	578	−6	cultivated	Bsk	0.593	0.401	41
sap 2011	Sapporo, JP	43.06	141.328	17.2	9	asphalt	Dfb	0.442	0.549	35
sbo 2009	Sede Boqer, IL	30.905	34.782	500	2	desert rock	Cwb	0.665	0.261	27
sov 2001	Solar Village, SA	24.91	46.41	650	3	desert, sand	BWh	0.705	0.278	23
tat 2006	Tateno, JP	36.05	140.133	25	9	grass	Cfa	0.413	0.558	35
tor 2006 (*)	Toravere, EE	58.254	26.462	70	2	grass	Dfb	0.481	0.446	41
xia 2006 (*)	Xianghe, CN	39.754	116.962	32	8	desert, rock	Dwa	0.468	0.576	34

For all locations except the last two (marked with (*)), there are also measured time series of the ambient temperature with a resolution of one, five, ten or sixty minutes, that are used afterwards for the models that calculate the temperature of the PV modules. Some locations (Brasilia, Brazil; Kwajalein, Marshall Islands; and Nauru Island) are taken twice with different years in order to assess the inter-annual stability of the results for exemplary locations.

The yearly clearness index *KT* and the yearly diffuse fraction are determined by

$$KT = \frac{GHI_{\text{year}}}{G_{\text{clear-sky, year}}} \text{ and } DF = \frac{DHI_{\text{year}}}{GHI_{\text{year}}} \quad (1)$$

where the clear-sky irradiance $G_{\text{clear-sky}}$ is calculated from the extraterrestrial irradiance G_{ext} and the elevation of the sun γ_s with a modification of the approach by Bourges [3]

$$G_{\text{clear-sky}} = 0.78 G_{\text{ext}} \sin(\gamma_s)^{1.15} \quad (2)$$

2.2. Data Preparations

Before conducting the simulations, the following data preparations are made. One-hour averages are generated from the one-minute values of the global and diffuse horizontal irradiance (GHI and DHI) and the ambient temperature. From the one-hour averages of the global horizontal irradiance, one-minute values are synthesized using a recently developed and published algorithm [4] that has been independently evaluated by Remund this year [5] and attested to be the best-performing algorithm for synthesizing one-minute time series from one-hour averages of GHI.

For the synthesized one-minute values of GHI, a virtual diffuse horizontal irradiance is generated using the measured diffuse fraction:

$$DHI_{\text{syn}, i} = GHI_{\text{syn}, i} * df_{\text{measured}} = GHI_{\text{syn}, i} * \frac{DHI_{\text{measured}, i}}{GHI_{\text{measured}, i}} \quad (3)$$

The calculation of the optimal tilt angle for all locations was conducted using the one-minute measurement values of the global and diffuse irradiance and the transposition model of Hay and Davies [6].

2.3. Matrix Simulations

For each of the 30 locations, a complete time-step simulation of one year is conducted using the PV*SOL simulation core [7]. For each location, all elements of each matrix dimensions (models and modes) are combined with all others to form 810 unique model chains per location. In total, 24,300 time-step simulations with a resolution of one-hour or one-minute are executed. Figure 1 gives a schematic overview over the various dimensions of the matrix simulations. The global horizontal irradiance (GHI), the diffuse horizontal irradiance (DHI) and the ambient temperature (T_{amb}) are

measurement values form the BSRN database and come in one-minute resolution. These input values are then processed by diffuse fraction models that also need the output from solar position algorithms as input. The output of the diffuse fraction models, the diffuse and direct horizontal irradiance, is then used as input for the transposition models. Their output, the global and diffuse irradiance on the tilted plane, GTI and DTI, is then used as input for the subsequent model chain for the simulation of the PV module.

The mainly electrical PV module and inverter model chain that is connected to the irradiance model chain is simplified in this overview with the grey block on the right. Table 2 lists all the models and modes in detail. The selection was made by concentrating on the most commonly used models by the energy meteorology community.

Regarding the sun position algorithms, the selection aimed to include the fastest, i.e., computationally most light-weight, algorithm taken from the German Standard Din5034-2 [8], and the most accurate known candidate, the Solar Position Algorithm from NREL [9].

The amount of models to calculate the diffuse fraction of the global irradiance renders it more difficult to make a representative selection. In a recent evaluation study, Gueymard and Ruiz-Arias [10] presented a classification and validation of 140 separation models against measurement data with one-minute resolution of 54 locations worldwide, using BSRN and NREL databases. Unfortunately, our newly developed model [11] could not be integrated due to the publishing date. The validation was conducted with the help of numerous statistical indicators and climate groups and showed heterogeneous results. The mean average deviation of the best models lies within 10% and 20% when omitting high albedo locations.

Another approach of a worldwide validation was conducted by Zernikau [12], who chose 24 locations from the BSRN database and validated eight diffuse fraction models against their data. The average MAD per model over all locations was also found to lie around 10%. One-location validation studies include the work by Kambezidis [13], Wong [14] and Dervishi [15], who validated various models for the locations of Athens, Greece; Hong Kong; and Vienna, Austria, respectively. In our selection we wanted to include established algorithms like, amongst others, Reindl [16], Erbs, Klein and Duffie [17] or Orgill and Hollands [18], as well as more recently developed models like Boland, Ridley and Laurent [19,20] and our new algorithm [11].

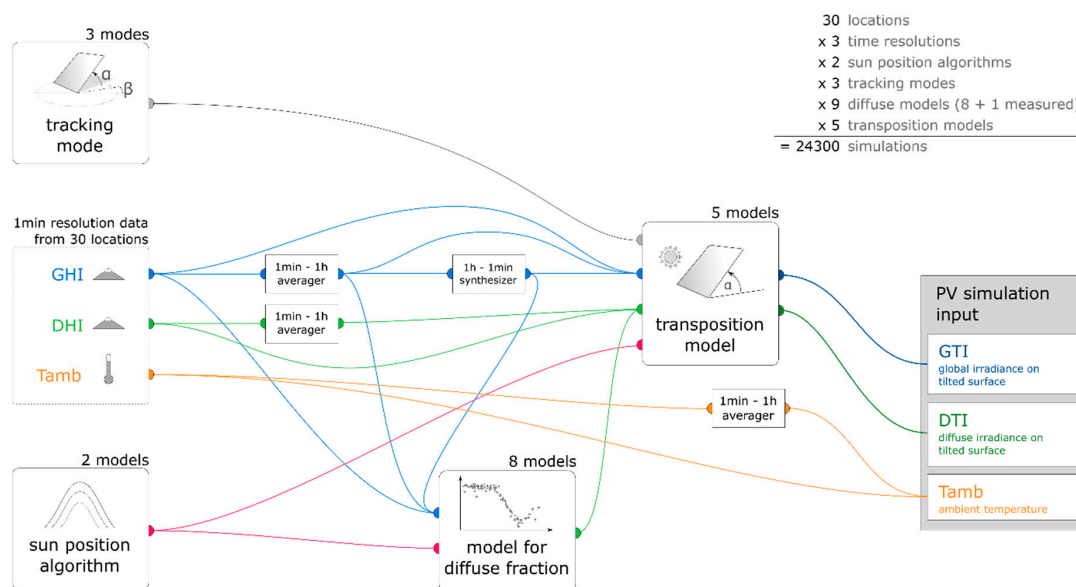


Figure 1. Schematic overview over the matrix simulations. The model chain for the electrical simulation of the PV system is simplified with the grey block on the right. The combination of all models and inputs leads to a total of 24,300 simulations.

Table 2. Overview over the dimensions of the matrix simulation.

Dimension	Models/Modes	Amount
Locations	See Table 1	30
Input data/time resolution	<ul style="list-style-type: none"> • 1-min measurement values • 1-min synthesized values [4] • 1-h averaged values 	3
Sun position	<ul style="list-style-type: none"> • Din5034-2 [8] • NREL SPA [9] 	2
Tracking mode	<ul style="list-style-type: none"> • Fixed tilt at 40°, facing south on northern hemisphere, north on southern hemisphere • Optimal tilt angle for each location, see Table 1 • Two-axis tracking with 180° East-West rotation limit 	3
Diffuse fraction	<ul style="list-style-type: none"> • Measurement values • Models <ul style="list-style-type: none"> ○ Reindl reduced [16] ○ Boland, Ridley and Laurent (BRL) [19] ○ Boland, Ridley and Laurent 2010 (BRL 2010) [20] ○ Erbs, Klein and Duffie (EKD) [17] ○ Orgill and Hollands (OH) [18] ○ Skartveit [21] ○ Perez and Ineichen (PI) [22] ○ Hofmann [11] 	9
Transposition models (irradiance on module plane)	<ul style="list-style-type: none"> • Liu and Jordan [23] • Hay and Davies [6] • Klucher [24] • Perez [25] • Reindl [26] 	5
Total		24,300

A multitude of transposition models to calculate the irradiance on tilted surfaces has been developed in the past 60 years, and many validation studies have been presented. The first model to name is the isotropic approach of Liu and Jordan [23], other well-known and widely used models are Hay and Davies [6], Klucher [24], Perez [25] and Reindl [26]. These five models constitute our choice for the matrix simulations. There exist a lot more transposition models, where the approaches by Temps and Coulson [27], Muneer [28], Olmo [29], Gueymard [30] and Badescu [31] are probably the most well-known and validated except the models listed above.

Notable recent validation studies include the work by Yang [32], who lists and compares 26 models against one-minute measurement data from four locations with two to eight sensor orientations each, see values in brackets: Eugene, OR, USA (3); Oldenburg, Germany (2); Singapore (8); and Golden, CO, USA (5); the normalized MBD was found to lie between -11% and $+12\%$ for tilt angles up to 45° and between -45% and $+20\%$ for vertical surfaces. Another comprehensive contribution is made by Ineichen [33], who validates eight models against one-minute and one-hour data of two locations and the studies of Loutzenhiser [34], Gueymard [35], Demain [36] and Gulin [37], who compare seven to 14 models against the measurement data of one location. In these studies, measurement data were from Geneva and Duebendorf, Switzerland; Denver and Golden, CO, USA; Uccle, Belgium; and Zagreb, HR.

Other parameters and models used in the simulation of the PV system are listed in Table 3. These values and models represent the default setting in most simulation software like PV*SOL. The albedo value of 0.2 represents a ground reflectance of, e.g., sand, grass or asphalt. The reflection model and the Incidence Angle Modifier (IAM) define how much irradiance is reflected on the glass surface of the PV module. The spectral losses consider the fact that the spectral distribution of the irradiance might not be equal to the AM1.5 solar spectrum on which the PV modules are tested.

Table 3. Other parameters and models used in the model chain for the PV system simulations.

Parameter/Model	Value
Albedo	0.2
Reflection model	ASHRAE [38,39]
Incidence Angle Modifier (IAM)	0.95
Spectral losses	0.01
PV modules	8 kWp nominal power, 40 × 200 Wp polycrystalline standard module, modeled with the two-diodes model
Inverter	7 kVA standard inverter, max. efficiency 94.6% at 50% load
Sizing factor	114%
Electrical modeling	Based on IV characteristics superposition, PV-MPPT-Inverter feedback loop
Grid voltage	230 V
Cable resistance	0 Ω

The electrical modeling of the PV modules and the DC/AC inverter with maximum power point tracking (MPPT) is based on detailed superposed IV characteristics and real MPP tracking behavior with feedback loop to the PV generator. This means that like in real PV plants, the PV generator provides a full IV characteristic to the MPP tracker in each time step. The tracker then selects the MPP voltage and current, and converts them to AC energy at grid voltage. The selected MPP current is fed back to the PV generator and the energetic losses caused thereby are calculated. The ohmic resistance of the DC and AC cabling is set to 0.

To give an idea of how these matrix simulations look and how the results of one model chain differs from the other, an example of a very small matrix simulation is given in Figure 2. Here, only one day is simulated instead of a whole year, and only for the location of Lindenberg, Germany. The rows represent the three types of input data (one-minute measured, one-minute synthesized and one-hour averages). The first column shows the pure input data as a function of local time. In the second column, the output of the diffuse models is plotted in yellow to red color. Already here, significant differences can be observed between the different models. On the third column, the simulated PV energy for the exemplary 8 kWp plant is displayed for three different combinations of diffuse fraction and transposition model.

2.4. Clipping Losses Analysis

In addition to the matrix simulations, the inverter clipping losses are analyzed with a further set of simulations. In a previous publication [4] we already examined the clipping losses for Lindenberg, Germany, for an exemplary simulation setup. In this contribution we want to analyze the influence of the models and input data types on the clipping losses more in detail.

Out of the matrix subset listed in Table 2, only the model chains of the location of Lindenberg, Germany, are selected. As additional dimension, the sizing factor, i.e., the ratio of installed PV power on the DC side and AC inverter rating, is increased from 100% to 200%. To achieve this, the AC inverter rating is reduced from 8 kVA to 4 kVA in 0.5 kVA steps. This leads to a total of 2970 simulations. These are conducted twice: First with a realistic inverter efficiency curve with a maximum efficiency of 94.6%, and second with an ideal efficiency curve of 100% over the whole inverter range.

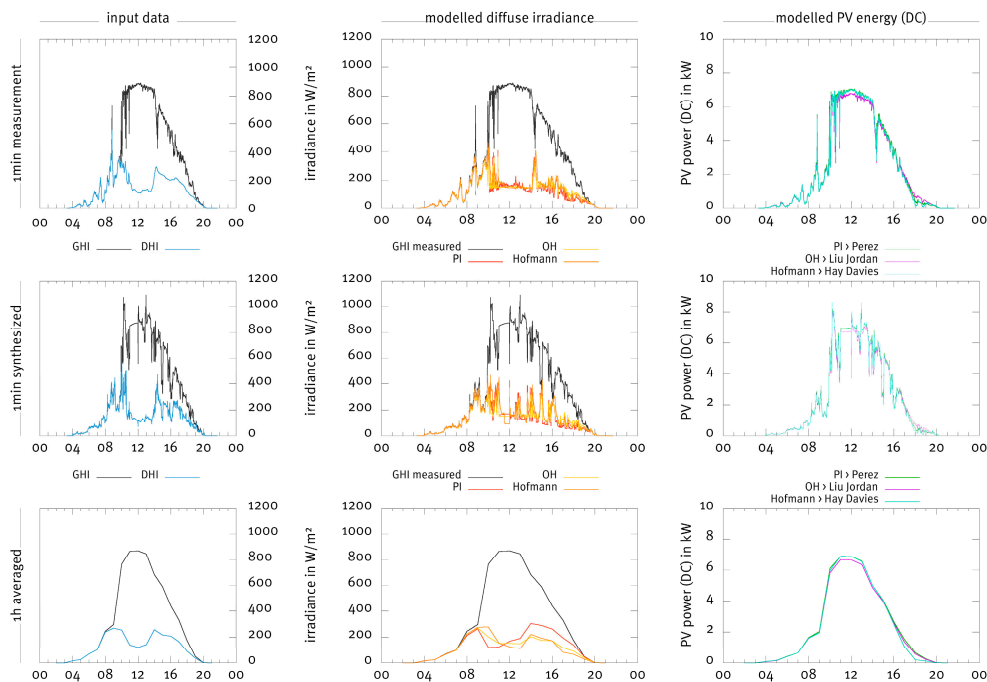


Figure 2. Simplified example of the matrix simulations for one day (5 June 2003) and one location (Lindenberg, Germany). Selected diffuse and transposition models only. In the left column, the three different input types are plotted: measurement one-minute values on the top, synthesized one-minute values in the middle and averaged one-hour values below. The second column displays the diffuse irradiance modeled by three different diffuse fraction models (OH, Orgill and Hollands [18]; PI, Perez and Ineichen [22]; and Hofmann [11]). The column on the right shows the resulting PV power (DC) for three different combinations of diffuse fraction and transposition models: PI with Perez [25], OH with Liu and Jordan [23] and Hofmann with Hay and Davies [6]. Sun position algorithm is Din5034-2 [8], tracking mode is fixed tilt at 40° .

3. Results

In this section, the results of the matrix simulations and the clipping losses analysis are presented. The amount of simulation runs requires a compact and grouped presentation of the results in subsections. In most cases, the simulation results are displayed in forms of boxes and whiskers that contain various results from different model chain combinations.

3.1. Influence of Sun Position Models

The difference of irradiance and PV energy output over all simulations varies between -0.1% and 0% for one-hour values, while it can be found to be within -0.07% to -0.01% for measured and synthesized one-minute values. Due to this negligible spread in the results, the impact of sun position models is negligible. All following results are based on the Din5034-2 algorithm [8].

3.2. Influence of Input Data

To assess the influence of the input data, the synthesized one-minute values and the averaged one-hour values are compared against the measured one-minute values. For each model chain combination, the resulting GTI and AC PV energy output of the synthesized one-minute values and the one-hour averages are compared to the results when using measured one-minute values as input.

Figure 3 shows the deviations for each location concentrated in boxes and whiskers on the left. On the right, the average over all absolute (unsigned) deviations is shown. In this plot, only results of simulations with optimal module tilt are displayed.

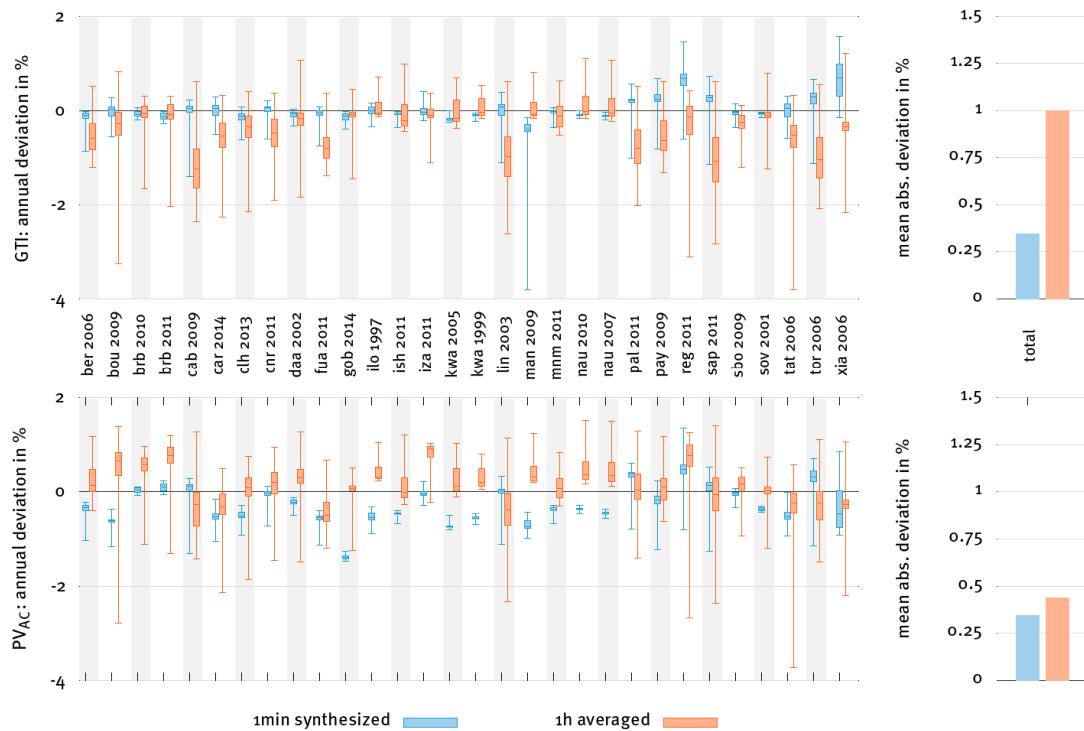


Figure 3. Influence of input data on the global horizontal irradiance (GTI, top) and the AC PV energy output (PCAC, bottom). The results of all model chains with one-minute measurement data are compared to one-minute synthesized data (blue) and one-hour averaged data (red). The boxes and whiskers contain 45 results each (nine diffuse fraction models by five transposition models). On the right, the absolute value of all single deviations is calculated and averaged over all locations.

The first important fact to notice is the strong difference of the results between locations. This underlines the findings of precedent studies that models have to be developed and validated for as many locations as possible to adequately assess their quality and applicability for various locations.

Secondly, for GTI the results are significantly closer to the results of measured one-minute values with synthesized one-minute values than with averaged one-hour values. The mean absolute deviation for GTI is significantly smaller when using synthesized one-minute values compared to one-hour averages. These differences can be explained by the highly volatile nature of the solar irradiance that is not sufficiently modeled with one-hour averages, as diffuse fraction, transposition effects and the sun position are subject to substantial changes during one-minute time frames.

These differences decrease when looking at the AC output of the PV system (bottom plots), since the PV energy on the DC side at the inverter input is lower when using one-hour averages. However, the spread and the accuracy of synthesized one-minute data clearly outperform the one-hour averages.

3.3. Diffuse Irradiance

In this section, the eight diffuse fraction models are compared against the measured one-minute values for all locations. For each location, the relative deviations of the diffuse irradiation values modeled by the eight models from the measured annual diffuse irradiation is calculated. Figure 4 displays the deviations at the bottom, each box and whisker contains the results from 30 locations. For the top plot, the absolute value of the relative deviations is taken and averaged per model.

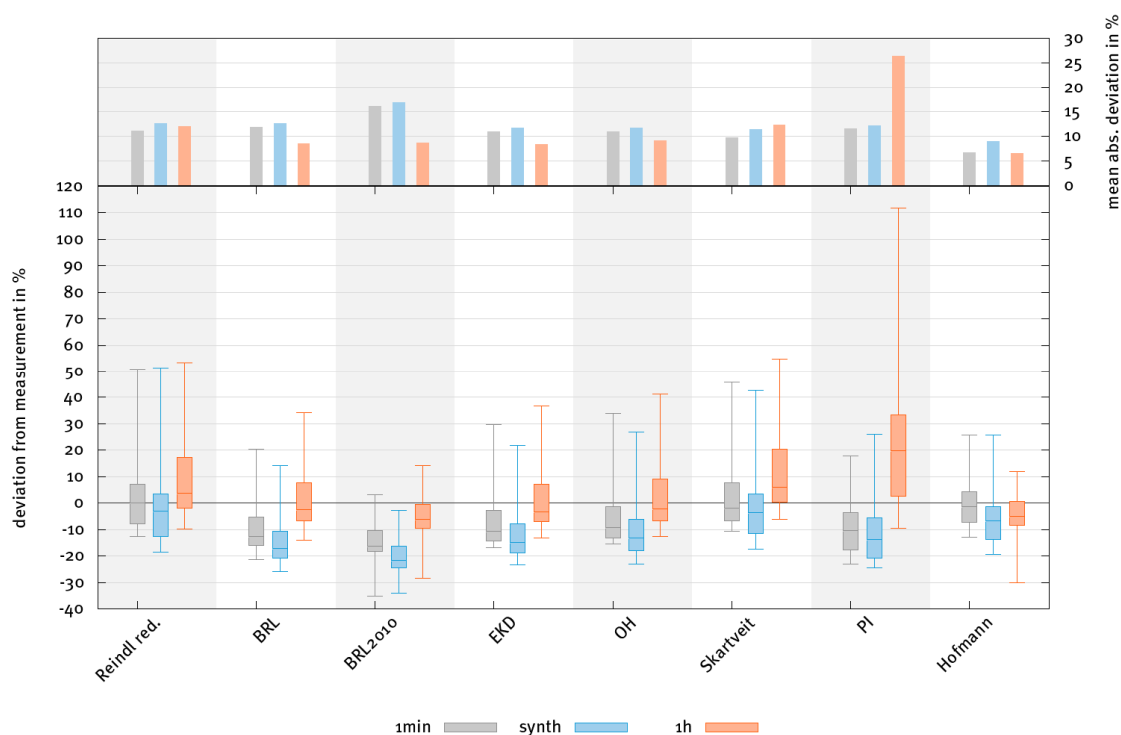


Figure 4. Deviation of the modeled annual diffuse irradiation (irradiance integrated over one year) from the measured irradiation. The bottom plot displays the deviations over all locations and model combinations grouped by the diffuse fraction model. Each box and whisker contains results from 30 simulations at different locations. The top plot displays the average over all absolute (unsigned) deviations in the boxes and whiskers at the bottom.

As recently shown in the presentation of our new diffuse fraction model [11], our approach (Hofmann) is capable of producing mean absolute deviations (MAD) of around 6% for one-minute values (grey). The other models produce MAD of 10% to 16%, which also corresponds to the findings in previous analyses. For synthesized one-minute values the results are similar, the Hofmann model produced the smallest deviation slightly elevated MAD. For one-hour averages, the Hofmann model still produces the smallest MAD, but other models are also featuring MAD of less than 10%.

The bottom part of the plot reveals deeper insight in the quality of the diffuse fraction models and the spread of their results. While, e.g., the “Reindl red.” and the “BRL” model lead to similar MAD in the top plot, the boxes and whiskers in the bottom plot show significant differences. The spread is higher for the “Reindl red.” model, from -12% to $+50\%$ but the box remains between -9% and $+8\%$ with the median at 0% , i.e., 50% of all simulation results lead to deviations of less than $\pm 10\%$. The “BRL” model however has its median at -13% with the box only covering the range from -16% to -6% which reveals a systematic underestimation of the diffuse fraction by this model.

The distribution of the results of the “Hofmann” model confirms the superiority of the MAD analysis: The median values lie close to 0% , the boxes do not exceed a range of 12% and the whiskers remain relative short in comparison to the other models.

3.4. Transposition Models

In this section, we want to present the main conclusions that can be extracted from a wide range of simulation results for modeling the PV energy for tilted surfaces. First, it is important to notice that, in this case, we do not have a “truth” to compare against as we have for the diffuse irradiance. In the validation data set, there is no measured irradiance for the tilted plane which is why we are unable to validate the performance of the models in this study as we did for the horizontal plane.

However, other studies have analyzed and validated a subset of these transposition models in the past, most notably by Yang [32] and Gueymard [35], for selected locations and tilt angles.

In the absence of validation data, we focus on the analysis of the qualitative differences of the five transposition models and give an idea on their influence on PV system simulations.

In Figure 5, the annual irradiation gains for the tilted modules are plotted over the tilt angle of the module for the five analyzed transposition models. The irradiation gains were calculated with one-hour data of Berlin, Germany, from Meteonorm [40]. Significant differences in the model output can be observed throughout the tilt angle range. While the Klucher model [24] even produces irradiation gains of $>0\%$ for horizontal modules due to a term on the diffuse irradiation that is not fully dependent on the tilt angle, the isotropic model by Liu and Jordan [23] calculates the lowest irradiation gains over the whole tilt angle range. For tilt angles for over 28° , the model by Perez [25] produces the highest gains.

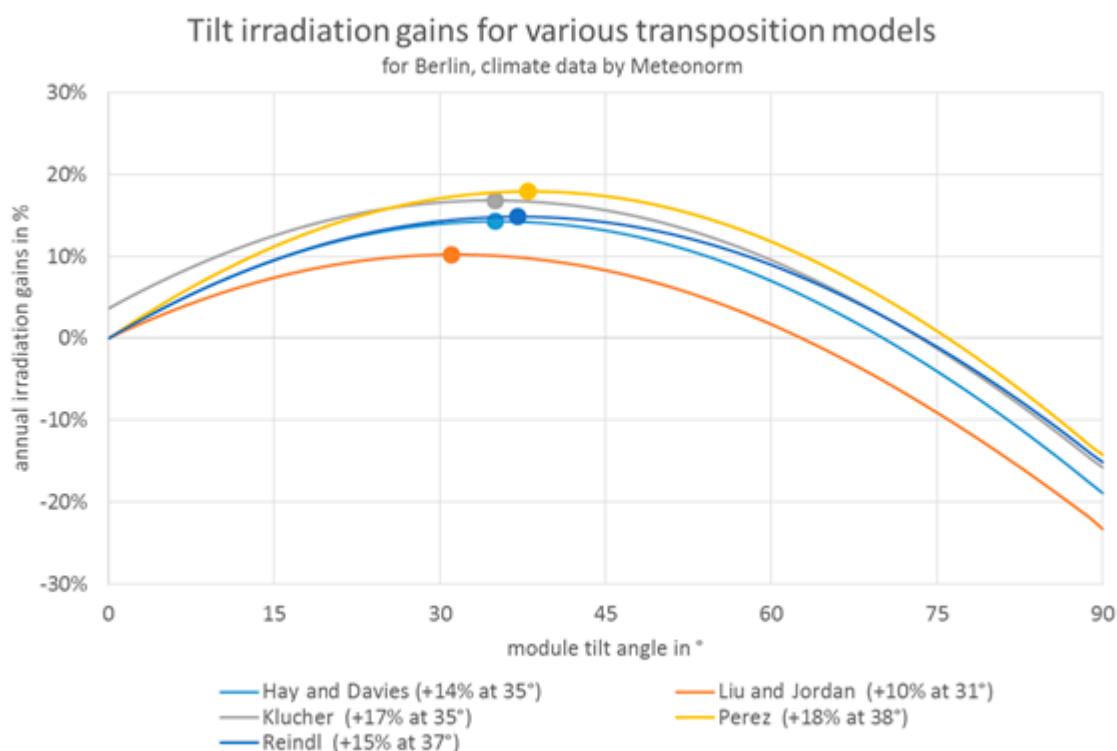


Figure 5. Annual tilt irradiation gains for various transposition models, calculated for Berlin, Germany, with one-hour climate data from Meteonorm [40]. The optimum tilt angles calculated by the models lie in the range from 31° to 38° . The Liu and Jordan model [23] produces the lowest irradiance gains while the model by Perez [25] produces the highest gains for tilt angles higher than 28° . Remarkably, the Klucher models [24] produces an irradiation gain of $>0\%$ for horizontal modules. It also produces highest gains for tilt angles up to 28° .

The calculated optimum tilt angle ranges between 31° for the Liu and Jordan model [23] (maximum tilt gain of 10%) and 38° for the Perez model [25] (maximum tilt gain of 18%). These significant differences can be observed in similar intensity over the whole tilt angle range: The irradiation loss for vertical modules (90°) ranges from -14% for the Perez model [25] to -23% for the Liu and Jordan model [23].

These results are in good agreement with the results of the reviews by Yadav [41] and Hafez [42] that also find the optimal tilt angle to vary significantly depending on the method used for determining it. The differences in energy gains presented in [41] between optimal yearly, seasonal and monthly tilt angles are found to be in the same range that is perceivable in Figures 5 and 6.

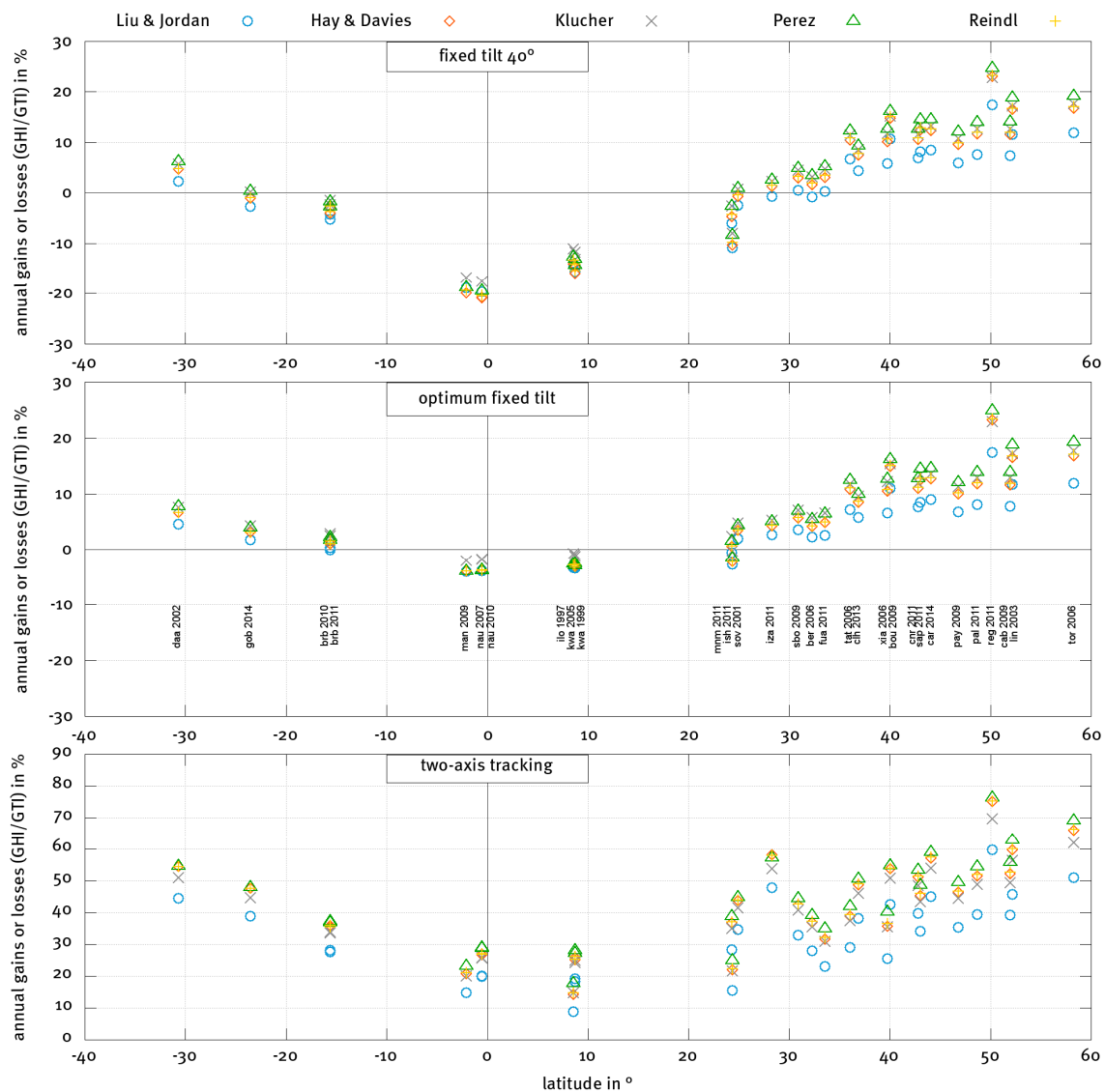


Figure 6. Annual irradiation gains and losses for the analyzed locations and three different module tilt modes: Fixed tilt at 40°, optimum fixed tilt (refer to Table 1 for location tilt angles) and two-axis tracking. A significant spread of the irradiation gains can be observed in all cases. The spread grows with increasing distance from the equator. For two-axis tracking systems, the spread is generally very high and reaches maximum differences between the lowest and highest modeled value per location of around 20% in Toravere, Estonia.

The study of Beringer [43] also compares measurements of tilt angle energy gains with modeled values for Hannover, Germany, and presents variations of the energy gain over the tilt angles that are comparable to the results presented here. The conclusion drawn in that study is fundamentally different, however, as it considers a difference of the annual PV energy yield of up to 6% as negligible.

Figure 6 displays the irradiation gains for all 30 locations over the latitude for three module mounting modes: With a fixed tilt of 40°, with a location-dependent optimum tilt (see Table 1) and with two-axis tracking. Each data point is calculated as the average of all model chains containing the respective transposition model. As expected, a clear dependency of the irradiation gains from the latitude is apparent for all three tracking modes. The longer the distance to the equator, the higher the irradiation gains will be. The small offsets to 0 for locations near the equator (man 2009 and nau 2007/2010) can be explained by reflection losses.

In general, a wide spread between calculated irradiation gains can be observed. The model by Liu and Jordan [23] leads to the lowest gains whereas the models by Klucher [24] and Perez [25] lead to the highest gains depending on the location and tilt mode. The maximum spread between the models is about 20% for two-axis tracking systems in Toravere, Estonia. For two-axis tracking systems in general, a spread of 10% to 15% can be observed.

3.5. Variance of Calculated PV Energy

For systems with a fixed tilt at 40° and optimum tilt the simulated PV energy varies between −5% and +8% (grey boxes and whiskers on the left and middle). For two-axis tracking systems, the results lie between −11% and +12% (left grey box and whisker). For synthesized one-minute values as input (blue), the distribution is of the same quality but shows slightly higher values. One-hour averages as input data lead to a narrower distribution of the values for fixed tilt at 40° and optimum tilt, but also to a significantly wider distribution for two-axis tracking systems.

The median for all simulations is close to 0. In the case of the two-axis tracking systems, the box of the synthesized one-minute values has a tendency to positive deviations, whereas the results tend to be distributed more on the negative side for one-hour values.

These results have to be interpreted in context of the inter-annual variability and the economic impact of energetic losses or gains on the internal rate of return (IRR). The inter-annual variability of the results for the exemplary locations (Brasilia, Brazil; Kwajalein, Marshall Islands; and Nauru Island) lies between −2.6% and +2.0% with median values of −2.2% to 1.8%, which is comparable to the results presented in Figure 7. Detailed data of the inter-annual deviation is listed in Table 4.

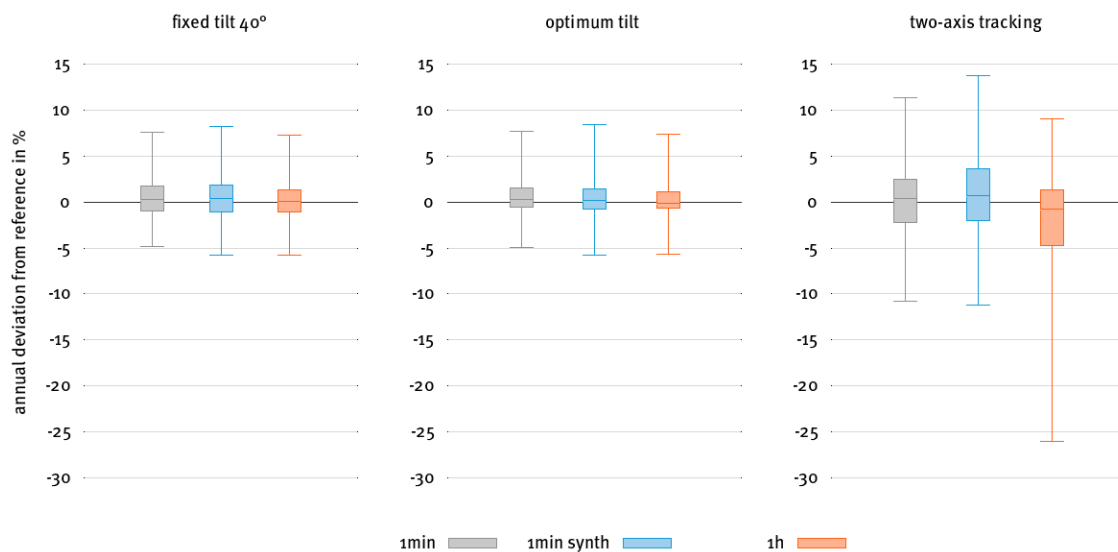


Figure 7. The annual deviation of the modeled PV energy from the reference model chain, grouped by tilt mode and input data type. The reference is calculated from the output of the model chains that contain one-minute measurement data for both global and diffuse irradiation. Each box and whisker contains results from all model chains that can be assigned to the corresponding tilt mode and input data type, i.e., 1200 results per box and whisker (30 locations, eight diffuse fraction models, and five transposition models).

Table 4. Inter-annual variability of the results for fixed-tilt systems for the locations of Brasilia, Brazil (BRB), Kwajalein (KWA) and Nauru Island (NAU).

Location	Deviation	Min	Q2	Median	Q3	Max
BRB (2010 and 2011)	dev _{GPI}	−0.0109	−0.0070	−0.0062	−0.0055	−0.0042
	dev _{PV}	−0.0081	−0.0055	−0.0047	−0.0041	−0.0020
KWA (1999 and 2005)	dev _{GPI}	−0.0260	−0.0235	−0.0222	−0.0207	−0.0162
	dev _{PV}	−0.0189	−0.0164	−0.0157	−0.0148	−0.0103
NAU (2007 and 2010)	dev _{GPI}	0.0150	0.0166	0.0172	0.0176	0.0189
	dev _{PV}	0.0153	0.0169	0.0175	0.0184	0.0199

For PV system simulations, three main statements can be extracted from these results:

1. Positive: For most of the combinations of models for different locations, the simulated PV energy differs only by a few percent from the reference.
2. Negative: For some combinations, however, the deviation can be as high as −5% to 8% for fixed tilt systems and up to ±12% for two-axis tracking systems.
3. Negative: There is a very high uncertainty of the model quality when using one-hour averages on two-axis tracking systems.

The effect of energy losses on the IRR of a solar power investment is influenced by numerous variables and has to be analyzed on a case-by-case basis. For a simple grid feed-in PV system in Berlin, Germany, for example, with a feed-in tariff according to the EEG 2017 [44], no loan financing and without the consideration of taxes, the IRR decreases by 2.5% for every energy loss of 1%. That means that an energy loss of 8%, which is within the scope of the variability, can lead to a reduction of the IRR of 20% and can render a PV project uneconomical.

In order to analyze the influence of the model combinations in more in detail, the annual deviations from the reference are displayed in Figure 8. Only the results from systems with optimum tilt are used, grouped by diffuse fraction model, transposition model and input data type. Each box and whisker contains results from 30 locations.

In analogy to Figure 8, the results for systems with a fixed tilt angle of 40°, for systems with the optimum tilt angle for the respective location (same data as in Figure 8), two-axis tracking systems and the overall results for all three tracking types are shown in the Appendix A, Figures A1–A4. The general character of the results is the same for all tracking types, with some extreme outliers for the Perez and Ineichen transposition model for two-axis tracking system, which is why the analysis is based only on the optimal tilt systems and the other results are shown in the Appendix A for reference.

When comparing the first group per row with the rest, it becomes apparent that diffuse models in general add a lot of spread to the results. While the results vary clearly and systematically as a function of the transposition model (comparing box and whiskers within a group), the influence of the diffuse fraction models on the distribution of the annual deviations is less prominent.

We would like to emphasize here that the deviation shown in Figures 7 and 8 is calculated against a reference that consists of simulated data only. The reference is the average of all simulation results in the black frame in Figure 8, i.e., with one-minute measurement values of global and diffuse horizontal irradiance. This is not to be understood as validation of transposition models against measurement values.

Nevertheless, we conclude that the transposition model by Liu and Jordan [23] leads to the smallest variation, but also to the lowest results, as seen above. The models by Hay and Davies [6] and Reindl [26] produce results that lie close around the reference in most of the cases. The models by Perez [25] and Klucher [24] produce the results with the highest deviation from the reference. Simulations using the model by Klucher [24] also feature a high variation of the results.

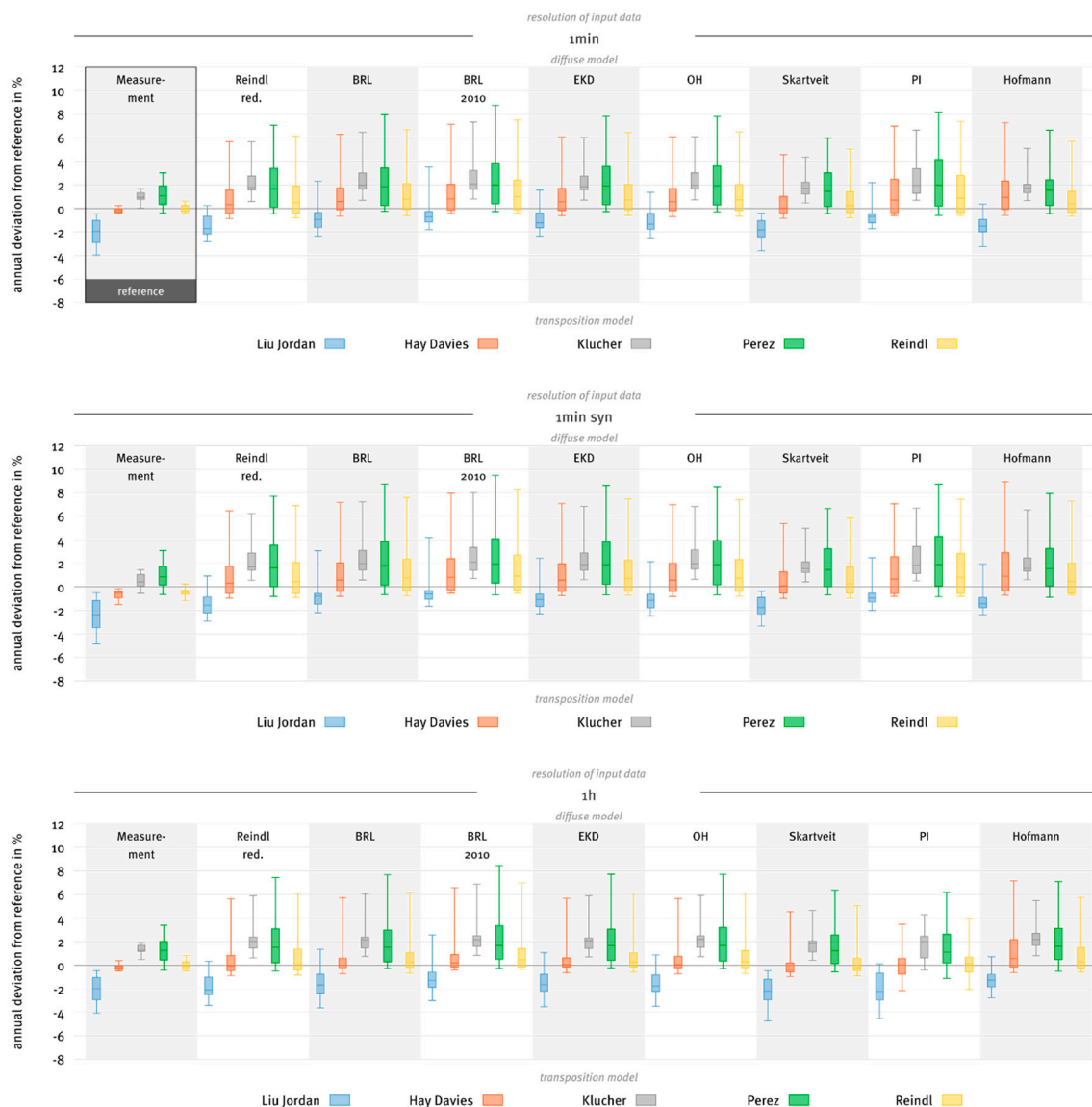


Figure 8. The annual deviation of the modeled PV energy from the reference model chain, grouped by diffuse fraction model, transposition model and input data type. The reference is calculated from the output of the model chains that contain one-minute measurement data for both global and diffuse irradiation (black frame). Each box and whisker contains results from 30 locations. Here, only the results of the optimal tilt mode are displayed. See Appendix A Figures A1–A4 for other tilt modes and overall results.

3.6. Inverter Clipping Losses

In this section, we present the results of the analysis of the inverter clipping losses for the location of Lindenberg, Germany, 2003. As described in Section 2.4, the inverter AC rating is decreased from 8 kVA to 4 kVA in steps of 0.5 kVA, which leads to sizing factors that increase from 100% to 200%. The PV plant is simulated with every combination of diffuse fraction and transposition models, and for all three types of input data: one-minute measurement, one-minute synthesized and one-hour averages.

The entirety of the results is displayed in the Appendix A, in Figure A5, for DC/AC inverters with realistic efficiency characteristics at the lower end, with a maximum efficiency of 95% at 50% load. In Figure 9, three selected model combinations illustrate the main aspects of the analysis.

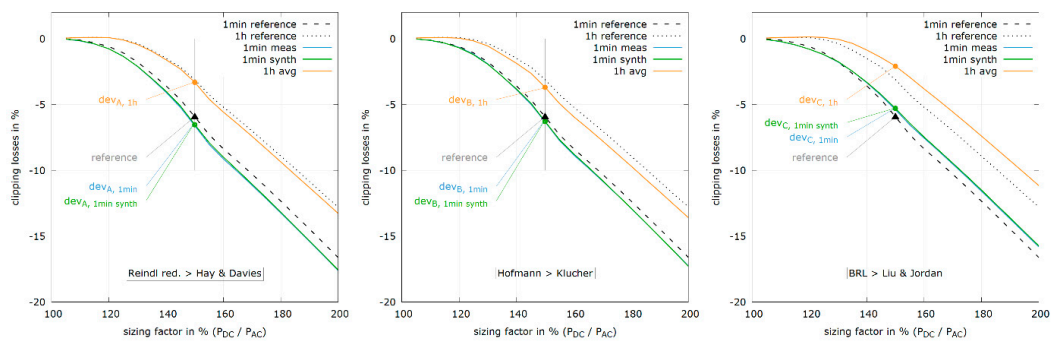


Figure 9. Inverter clipping losses as a function of the sizing factor of the PV plant, for one-minute measurement and synthesized data and one-hour averages. Three different combinations of diffuse fraction and transposition models as example. The clipping losses at 150% sizing factor for all model combinations are displayed in Figure 10.

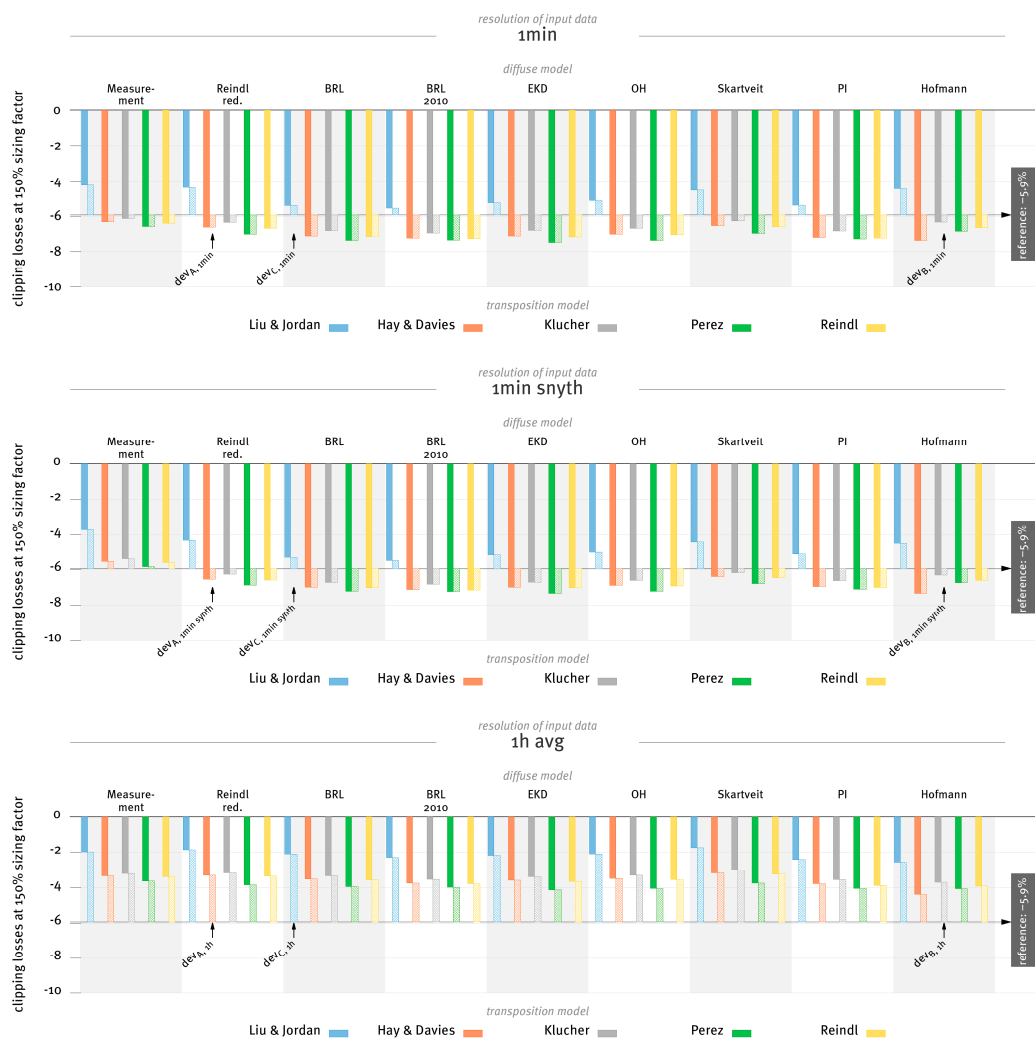


Figure 10. All inverter clipping losses simulated with a sizing factor of 150%. Selected data points (dev_A , dev_B and dev_C) can be compared to Figure 9. The main bars in full color represent the absolute clipping loss as a result of the simulation with the respective choice of models and input data type. The side bars in light color represent the deviation from the reference. The reference is calculated as the average of the model chains using one-minute data for global and diffuse irradiance.

For comparison, the results of simulations with ideal inverters are displayed in the Appendix A, Figure A6.

In all of the analyzed cases, the clipping losses are significantly higher when using one-minute data compared to one-hour averages. When using one-hour averages as input data, the simulated clipping losses remain at 0% up until sizing factors of 120%, where one-minute data already show significant losses of 1% and more. The underestimation of the inverter clipping losses continues to rise until around 160% sizing factor, where the simulated losses using one-minute data lie around 8%, with losses using one-hour averages at around 5%, an underestimation of over 60%.

The absolute value of the clipping loss also depends on the selected models for the diffuse fraction and transposition. Figure 10 displays the clipping losses for all model combination and input data types for a sizing factor of 150%. There is no significant difference in clipping losses when using synthesized one-minute data instead of measured (compare top plot against middle plot). When using one-hour averages, the clipping losses lie between 2% and 4%, while the reference calculated from one-minute data of global and diffuse irradiance lies at 5.9%.

The influence of the models for the diffuse fraction cannot be clearly answered again, as the main drivers for simulation differences remain the transposition models. Again, the model by Liu and Jordan [23] leads to underestimated clipping losses, while the model by Klucher [24] leads to the highest values in most of the cases.

To simulate PV plants with sizing factors of more than 110%, one-minute values are needed. This corresponds to the findings by Burger and R  ther [45] and Ransome [46]. If measured values are not available, the use of synthetic values is highly recommended.

4. Conclusions

From the above analyses and results, the following main conclusions can be extracted. Based on our results, we derived recommendations for models used in PV system simulations to put the conclusions in a practical context for PV system modeling and compiled them in Table 5.

Table 5. Main results of this study and their consequences on PV modeling.

No.	Result	Recommendation for PV System Modeling
1.	Results of PV system simulations vary strongly from one location to another.	No model should be validated using only one location. Results from models developed for a specific location should be used with great care only
2.	The simulated PV energy varies between -5% and $+8\%$ from the reference for fixed tilt (40° or optimum) and between -10% and $+15\%$ for two-axis tracking systems.	Diffuse fraction and transposition models have to be carefully selected and should be improved. Further validation for transposition models to the full extent is urgently needed.
3.	The sun position algorithm is of minor importance	Usage of faster DIN5034-2 algorithm over NREL Spa is reasonable.
4.	Synthesized one-minute values lead to results of comparable quality as measured values.	Either measured or synthesized one-minute values should be used for PV system simulations. One-hour averages are only utilizable for PV systems with sizing factors of less than 110%.
5.	The superior performance of the previously presented diffuse fraction model could be confirmed in this study.	The Hofmann diffuse fraction model may be used as a state-of-the-art model.
6.	Diffuse models lead to wider spread of simulation results.	Where available, diffuse irradiance measurement should be used. Influence of diffuse fraction models is highly location-dependent. Further analysis of the performance of the diffuse fraction models as function of climatic parameters is required.
7.	Transposition models have a high impact on simulation results.	Further validation studies for different locations and tilt angles are required.

It should be emphasized that the present study does not reveal the impact of spectral effects, which become more important for tilted surfaces. In addition, we investigate the effect on yearly sums only. Even if this is presently the most relevant feature for PV systems, effects on the diurnal variation will become more important for the use of renewable energies in the future in the absence of large and cheap energy storage systems. One aspect that deserves more attention than was possible in the scope of this paper is the dependency of the performance of diffuse models on the climatic conditions at a location. This study also highlights the importance to intensify the effort to validate transposition models in order to minimize the uncertainties of PV system simulations. In the absence of globally available high-resolution measurement data of the irradiance on tilted planes, however, this task incorporates a complexity that is not to be underestimated. Future work must include thorough meta-study analyses on the topic, data collection of high quality measurement setups and intense validation.

Acknowledgments: The publication of this article was funded by the Open Access Fund of the Leibniz Universität Hannover.

Author Contributions: Martin Hofmann designed the study, implemented the simulations, analysed the data and edited the manuscript. Gunther Seckmeyer helped editing the manuscript.

Conflicts of Interest: The authors declare no conflict of interest.

Appendix A

Fixed 40°:

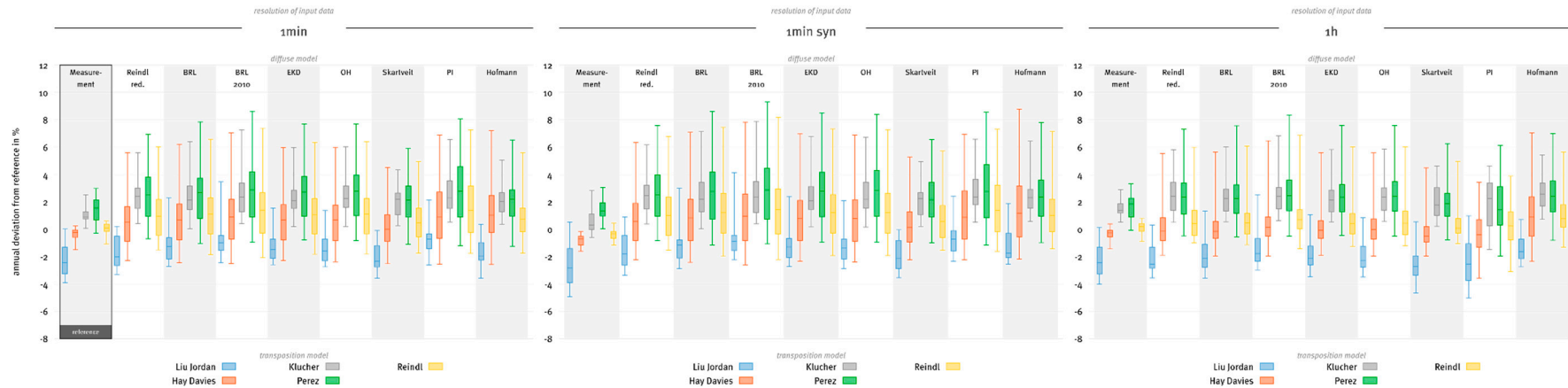


Figure A1. The annual deviation of the modeled PV energy from the reference model chain, grouped by diffuse fraction model, transposition model and input data type. The reference is calculated from the output of the model chains that contain one-minute measurement data for both global and diffuse irradiation (black frame). Each box and whisker contains results from 30 locations.

Optimum Tilt:

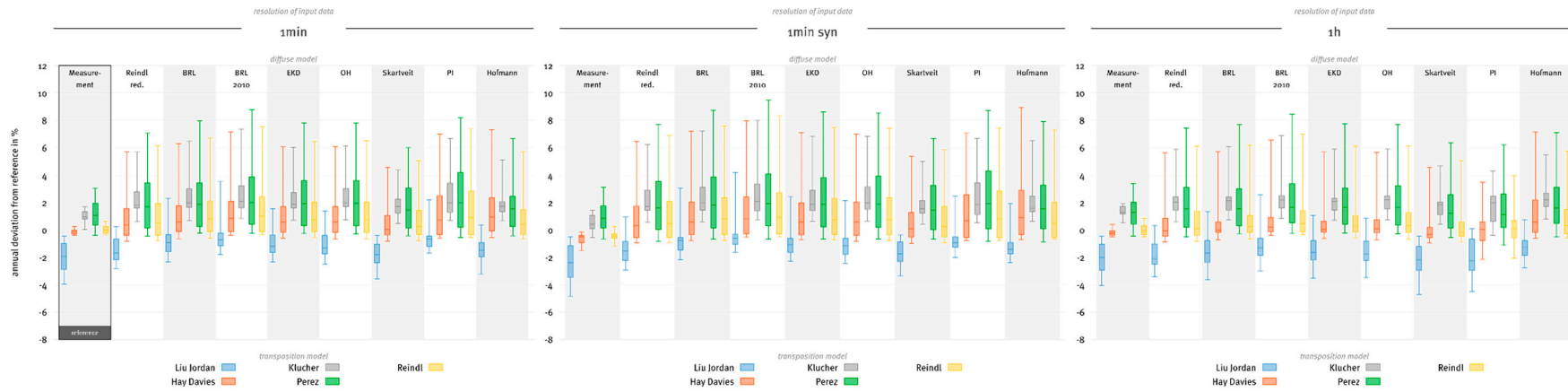


Figure A2. Same plot type as Figure A1, but for modules with optimal tilt. Corresponds to Figure 8.

Two Axis Tracking:

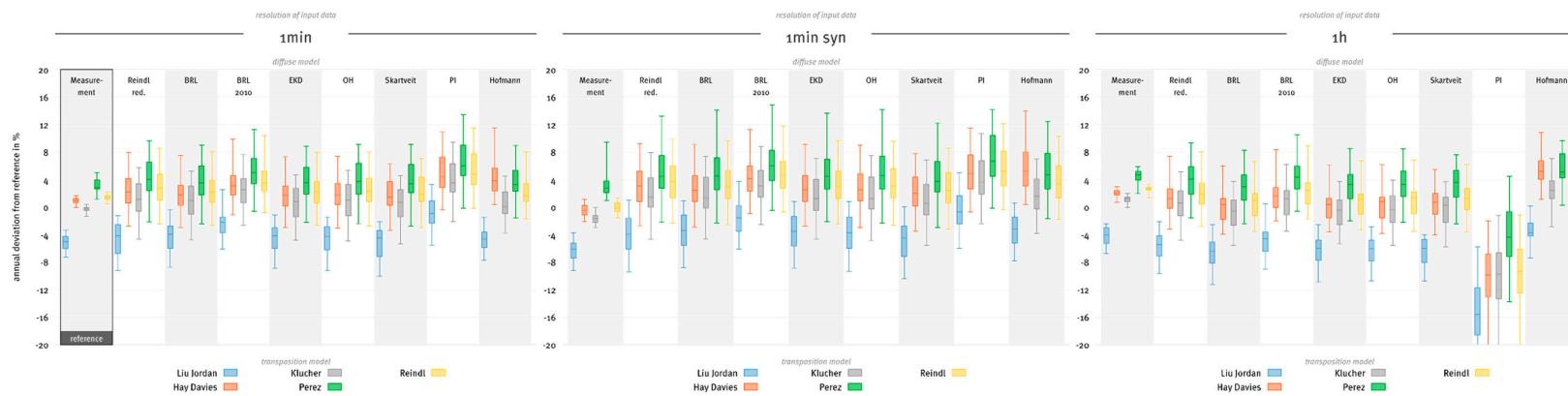


Figure A3. Same plot type as Figure A1, but for modules with two-axis tracking. Note the different y scale in comparison to Figures A1 and A2.

All

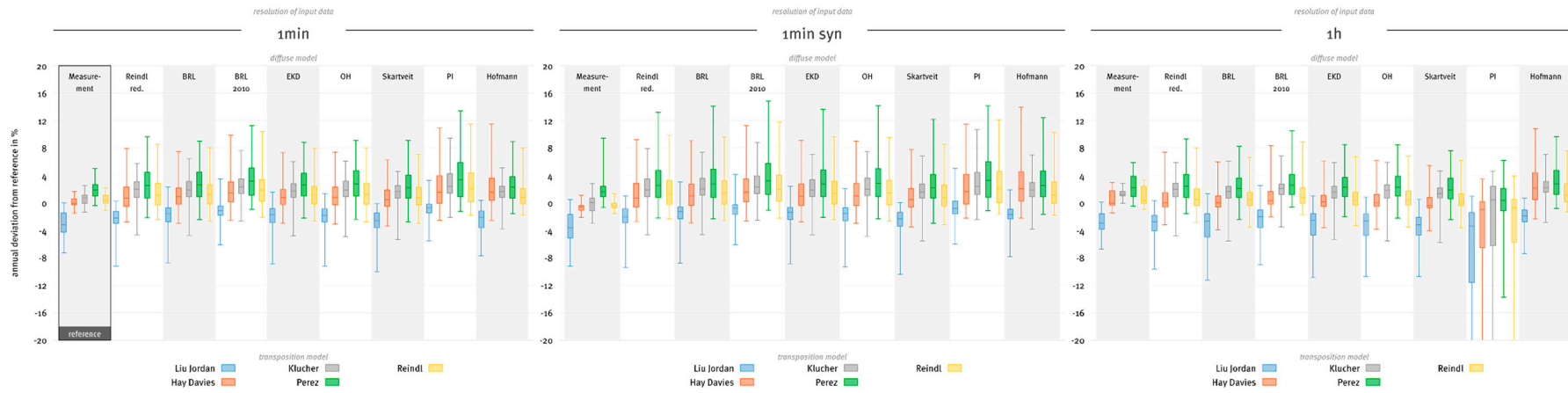


Figure A4. Same plot type as Figure A1, but with all results from all three module tilt modes. Note the different y scale in comparison to Figures A1 and A2.

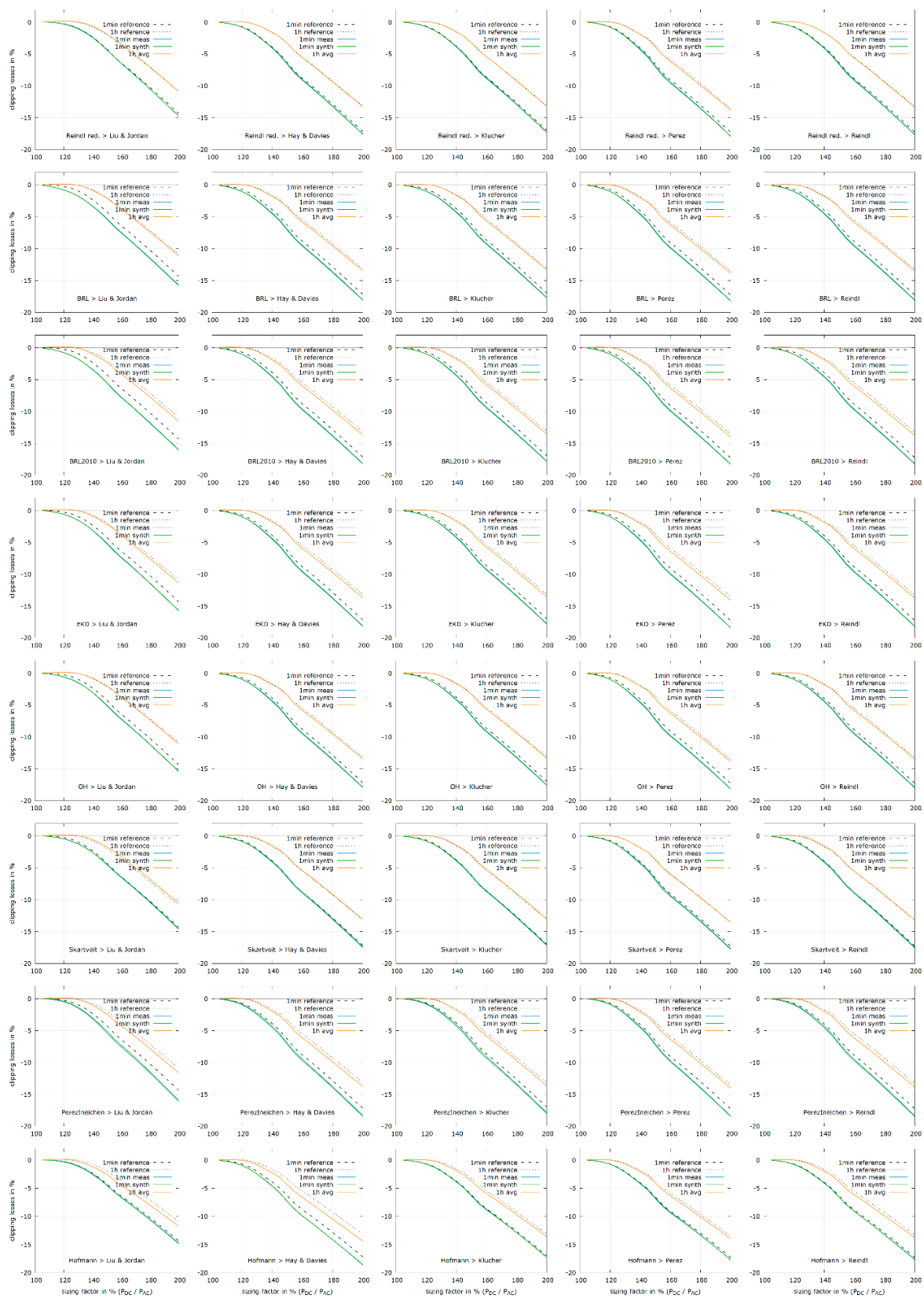


Figure A5. Inverter clipping losses as a function of the sizing factor of the PV plant, for one-minute measurement and synthesized data and one-hour averages. Rows refer to different diffuse fraction models, whereas columns refer to the five transposition models.

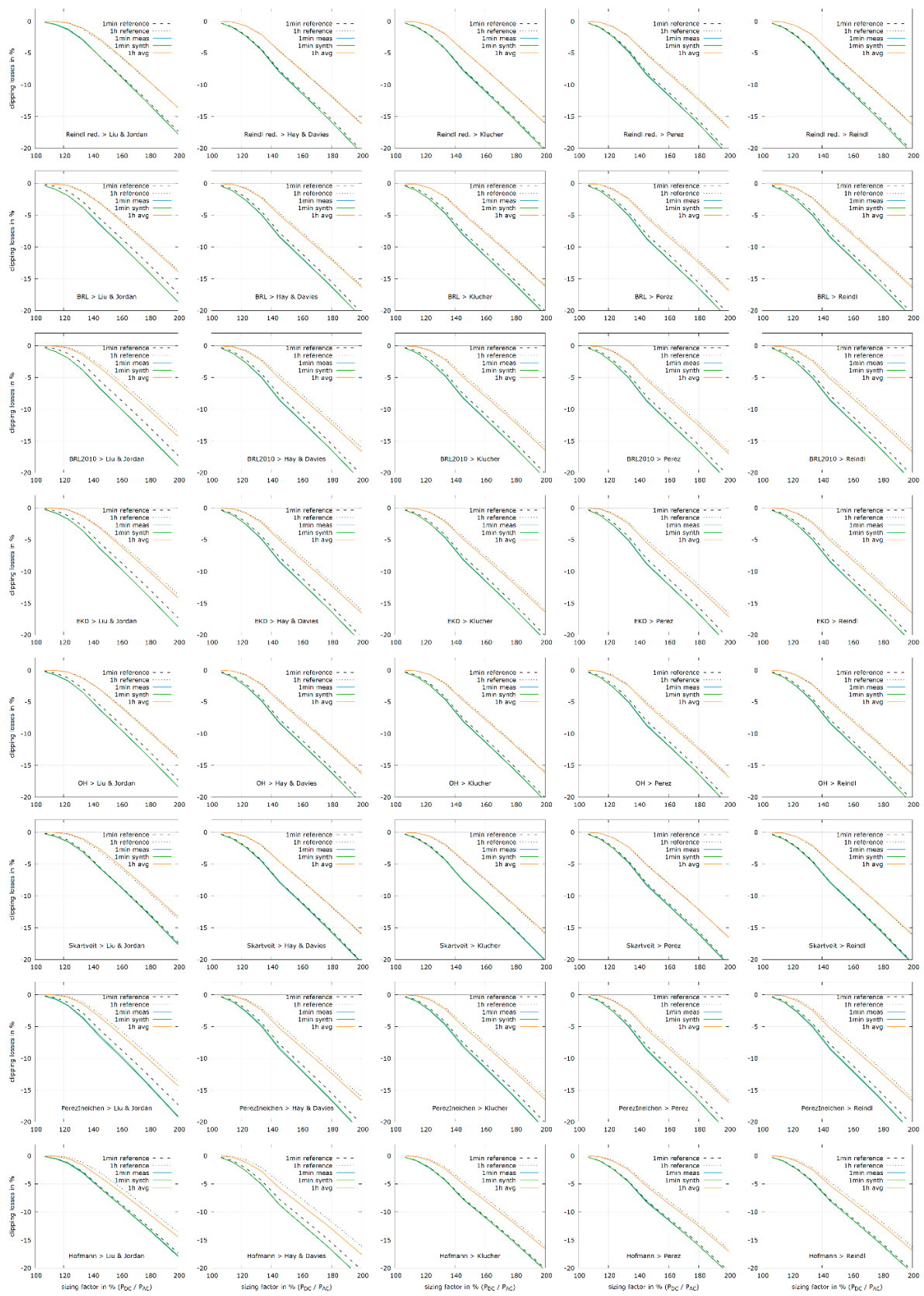


Figure A6. Same plot as Figure A5, but for inverter with an ideal efficiency of 100% over the whole operating range.

References

1. König-Langlo, G.; Sieger, R. Report of the working group BSRN—Baseline Surface Radiation Network. *AIP Conf. Proc.* **2013**, *1531*, 668–671.
2. Köppen, W. Klassifikation der Klimate nach Temperatur, Niederschlag und Jahresablauf (Classification of climates according to temperature, precipitation and seasonal cycle). *Petermanns Geogr. Mitt.* **1918**, *64*, 193–203.
3. Bourges, B. Improvement in solar declination computation. *Sol. Energy* **1985**, *35*, 367–369. [CrossRef]
4. Hofmann, M.; Riechelmann, S.; Crisosto, C.; Mubarak, R.; Seckmeyer, G. Improved synthesis of global irradiance with one-minute resolution for PV system simulations. *Int. J. Photoenergy* **2014**, *2014*. [CrossRef]
5. Remund, J. Neue Modelle für die Realistische Generierung von Minutenwerten. Available online: https://www.researchgate.net/publication/315767163_Neue_Modelle_fur_die_realistische_Generierung_von_Minutenwerten (accessed on 25 September 2017).
6. HAY, J.E.; Davies, J.A. Calculation of the Solar Radiation Incident on an Inclined Surface. In Proceedings of the First Canadian Solar Radiation Data Workshop, Toronto, ON, Canada, 17–19 April 1978.
7. Hofmann, M.; Hunfeld, R. *PV*SOL Simulation Core*; Valentin Software: Berlin, Germany, 2017.
8. German Institute for Standardisation. *Daylight in Interiors; Principles*; DIN: Berlin, Germany, 1985.
9. Reda, I.; Nrel, A.A. Solar Position Algorithm for Solar Radiation Applications (Revised). *Sol. Energy* **2004**, *76*, 577–589. [CrossRef]
10. Gueymard, C.A.; Ruiz-Arias, J.A. Extensive worldwide validation and climate sensitivity analysis of direct irradiance predictions from 1-min global irradiance. *Sol. Energy* **2016**, *128*, 1–30. [CrossRef]
11. Hofmann, M.; Seckmeyer, G. A New Model for Estimating the Diffuse Fraction of Solar Irradiance for Photovoltaic System Simulations. *Energies* **2017**, *10*, 248. [CrossRef]
12. Quaschnig, V. Vergleich und Bewertung Verschiedener Verfahren zur Solarstrahlungsbestimmung. Available online: https://volker-quaschnig.de/downloads/Sofo2002_1.pdf (accessed on 25 September 2017).
13. Kambezidis, H.D.; Psiloglou, B.E.; Gueymard, C. Measurements and Models for Total Solar Irradiance on Inclined Surface in Athens, Greece. *Sol. Energy* **1994**, *53*, 177–185. [CrossRef]
14. Wong, L.T.; Chow, W.K. Solar radiation model. *Appl. Energy* **2001**, *69*, 191–224. [CrossRef]
15. Dervishi, S.; Mahdavi, A. Computing diffuse fraction of global horizontal solar radiation: A model comparison. *Sol. Energy* **2012**, *86*, 1796–1802. [CrossRef] [PubMed]
16. Reindl, D.T.; Beckman, W.A.; Duffie, J.A. Diffuse fraction corrections. *Sol. Energy* **1990**, *45*, 1–7. [CrossRef]
17. Erbs, D.G.; Klein, S.A.; Duffie, J.A. Estimation of the diffuse radiation fraction for hourly, daily and monthly-average global radiation. *Sol. Energy* **1982**, *28*, 293–302. [CrossRef]
18. Orgill, J.F.; Hollands, K.G.T. Correlation equation for hourly diffuse radiation on a horizontal surface. *Sol. Energy* **1977**, *19*, 357–359. [CrossRef]
19. Boland, J.; Ridley, B. Models of diffuse solar fraction. In *Modeling Solar Radiation at the Earth's Surface*; Springer: Berlin/Heidelberg, Germany, 2008; pp. 193–219.
20. Ridley, B.; Boland, J.; Lauret, P. Modelling of diffuse solar fraction with multiple predictors. *Renew. Energy* **2010**, *35*, 478–483. [CrossRef]
21. Skartveit, A.; Olseth, J.A. A model for the diffuse fraction of hourly global radiation. *Sol. Energy* **1987**, *38*, 271–274. [CrossRef]
22. Perez, R.; Ineichen, P.; Seals, R.; Michalsky, J.; Stewart, R. Modeling daylight availability and irradiance components from direct and global irradiance. *Sol. Energy* **1990**, *44*, 271–289. [CrossRef]
23. Liu, B.Y.H.; Jordan, R.C. The interrelationship and characteristic distribution of direct, diffuse and total solar radiation. *Sol. Energy* **1960**, *4*, 1–19. [CrossRef]
24. Klucher, T.M. Evaluation of models to predict insolation on tilted surfaces. *Sol. Energy* **1979**, *23*, 111–114. [CrossRef]
25. Perez, R.; Seals, R.; Ineichen, P.; Stewart, R.; Menicucci, D. A new simplified version of the perez diffuse irradiance model for tilted surfaces. *Sol. Energy* **1987**, *39*, 221–231. [CrossRef]
26. Reindl, D.T.; Beckman, W.A.; Duffie, J.A. Evaluation of hourly tilted surface radiation models. *Sol. Energy* **1990**, *45*, 9–17. [CrossRef]
27. Temps, R.C.; Coulson, K.L. Solar radiation incident upon slopes of different orientations. *Sol. Energy* **1977**, *19*, 179–184. [CrossRef]

28. Muneer, T. Solar radiation model for Europe. *Build. Serv. Eng. Res. Technol.* **1990**, *11*, 153–163. [[CrossRef](#)]
29. Olmo, F.; Vida, J.; Foyo, I.; Castro-Diez, Y.; Alados-Arboledas, L. Prediction of global irradiance on inclined surfaces from horizontal global irradiance. *Energy* **1999**, *24*, 689–704. [[CrossRef](#)]
30. Gueymard, C. An anisotropic solar irradiance model for tilted surfaces and its comparison with selected engineering algorithms. *Sol. Energy* **1987**, *38*, 367–386. [[CrossRef](#)]
31. Badescu, V. 3D isotropic approximation for solar diffuse irradiance on tilted surfaces. *Renew. Energy* **2002**, *26*, 221–233. [[CrossRef](#)]
32. Yang, D. Solar radiation on inclined surfaces: Corrections and benchmarks. *Sol. Energy* **2016**, *136*, 288–302. [[CrossRef](#)]
33. Ineichen, P. *Global Irradiance on Tilted and Oriented Planes: Model Validations*; Technical Report; University Geneva: Geneva, Switzerland, October 2011.
34. Loutzenhiser, P.G.; Manz, H.; Felsmann, C.; Strachan, P.A.; Frank, T.; Maxwell, G.M. Empirical validation of models to compute solar irradiance on inclined surfaces for building energy simulation. *Sol. Energy* **2007**, *81*, 254–267. [[CrossRef](#)]
35. Gueymard, C.A. From Global Horizontal to Global Tilted Irradiance: How Accurate Are Solar Energy Engineering Predictions in Practice? Available online: <http://www.solarconsultingservices.com/Gueymard-Tilted%20radiation%20models%20performance-ASES08.pdf> (accessed on 25 September 2017).
36. Demain, C.; Journée, M.; Bertrand, C. Evaluation of different models to estimate the global solar radiation on inclined surfaces. *Renew. Energy* **2013**, *50*, 710–721. [[CrossRef](#)]
37. Gulin, M.; Vašak, M.; Baotic, M. Estimation of the Global Solar Irradiance on tilted Surfaces. Available online: http://www.apr.fer.hr/old/papers/EDPE2013_solar.pdf (accessed on 25 September 2017).
38. Souka, A.F.; Safwat, H.H. Determination of the optimum orientations for the double-exposure, flat-plate collector and its reflectors. *Sol. Energy* **1966**, *10*, 170–174. [[CrossRef](#)]
39. Laboratories, S.N. ASHRAE Model—PV Performance Modeling Collaborative. Available online: <http://pvpmc.org/modeling-steps/shading-soiling-and-reflection-losses/incident-angle-reflection-losses/ashre-model/> (accessed on 25 September 2017).
40. Meteonorm: Irradiation Data for Every Place on Earth. Available online: <http://www.meteonorm.com/images/uploads/downloads/broschuere-mn-7.1.pdf> (accessed on 25 September 2017).
41. Yadav, A.K.; Chandel, S.S. Tilt angle optimization to maximize incident solar radiation: A review. *Renew. Sustain. Energy Rev.* **2013**, *23*, 503–513. [[CrossRef](#)]
42. Hafez, A.Z.; Soliman, A.; El-Metwally, K.A.; Ismail, I.M. Tilt and azimuth angles in solar energy applications—A review. *Renew. Sustain. Energy Rev.* **2017**, *77*, 147–168. [[CrossRef](#)]
43. Beringer, S.; Schilke, H.; Lohse, I.; Seckmeyer, G. Case study showing that the tilt angle of photovoltaic plants is nearly irrelevant. *Sol. Energy* **2011**, *85*, 470–476. [[CrossRef](#)]
44. 2017 German Renewable Energy Law (EEG 2017). Available online: https://www.gesetze-im-internet.de/eeg_2014/BJNR106610014.html (accessed on 10 August 2017).
45. Burger, B.; Rüther, R. Inverter sizing of grid-connected photovoltaic systems in the light of local solar resource distribution characteristics and temperature. *Sol. Energy* **2006**, *80*, 32–45. [[CrossRef](#)]
46. Ransome, S.; Funtan, P. Why Hourly Averaged Measurement Data Is Insufficient to Model PV Performance Accurately. Available online: http://www.steveransome.com/PUBS/2005Barcelona_6DV_4_32.pdf (accessed on 25 September 2017).



3.4 Transposition models for the solar irradiance on tilted surfaces

Transposition models are used in the irradiance model chain to calculate the irradiance incident on a tilted surface. The direct fraction of the global irradiance can be transferred to the tilted plane with simple geometrical calculations. The diffuse fraction however is distributed anisotropically over the sky dome. To obtain the diffuse fraction of the global irradiance that reaches the inclined surface, i.e. the PV modules, estimations of this hemispherical distribution are needed. There are a number of approaches that aim to model the distribution of the diffuse irradiance with varying complexity.

The approach of Liu and Jordan [53] dates back to 1960 and assumes a simple isotropic distribution of the diffuse irradiance over the sky dome. Klucher [77] found the model of Liu and Jordan to be only of satisfying accuracy for overcast skies and added zones of horizontal and circumsolar brightening. A similar approach was presented by Hay and Davies [78], but without horizontal brightening. Instead, they introduced the anisotropy index as the relation of the beam irradiance to the extraterrestrial irradiance that was used to modify the amount of the circumsolar diffuse irradiance. Reindl et al. [79] presented a model that can be understood as an extension of the model by Hay and Davies with horizontal brightening. A more sophisticated model that was based on a multitude of measurements was presented by Perez [57]. It features empirical modelling of the clearness index and circumsolar and horizontal brightening coefficients that are stored in look-up tables and used depending on the sky cloudiness. The list of published transposition models up to date is extensive and continues to grow. Among the notable contributions are the models by Gueymard [80], Muneer [81], [82], Skartveit and Olseth [83].

Over time a lot of evaluation studies were published to estimate the model performance for varying locations and time resolutions. Recent studies try to take into account a wide variety of locations and PV module orientations as well as input data with a resolution of one minute. The most extensive study by Yang [84] included measurements of four locations in the USA, Singapore and Germany and validated 26 transposition models. Gueymard [85] validated 10 transposition models against measurement data for various PV module orientations for the location of Golden, Colorado, USA. Other notable evaluation studies include the work from Loutzenhiser [86], Kambezidis [87] and Notton [75].

In most of the mentioned evaluation studies however, the amount of available PV module orientations is limited. Also, the measurement data used for the validation is rarely resolved in intervals of one minute and does not cover a time range of more than a year. The influence of differing spectral and cosine responses and temperature behavior between horizontally installed pyranometers and the PV module surface is another aspect that was found to be not yet answered sufficiently.

In the study that forms the fourth part of the thesis, a total of 14 orientations of PV modules at the location of Hannover, Germany, was analyzed, seven facing south with elevation angles between 10° and 70°, six vertically mounted PV modules facing south, south-east, east, north, west and south-west as well as one horizontally installed module. The location of Golden, Colorado, USA is included in the analysis with five more orientations and both pyranometer and silicon-based sensors. The time range of the measurements comprises three years for Hannover and 22 months for Golden, with a resolution of one minute. Against this comprehensive dataset the models of Liu and Jordan, Klucher, Hay and Davies and Perez are validated.

It is found that the models of Hay and Davies and Perez produce the best overall results if horizontal pyranometer data and a constant albedo of 0.2 is applied. For the sunny location of Golden the model by Perez produces the best results with measured albedo values. Anisotropic models tend to overestimate the irradiance on tilted surfaces while the isotropic models underestimate it in most cases. In general, the model quality is directly dependent on the elevation angle of the analyzed PV module. The systematic uncertainties introduced by using horizontal pyranometer measurements to model the irradiance incident on PV modules has – depending on the model – little to no effect on the model output. The relative mean

absolute deviation (rMAD) between model and measurement lies between 5 and 9% for south facing PV modules inclined by 40° in Hannover Germany and between 4 and 6% in Golden, Colorado, USA. For vertically installed PV modules facing south the rMAD ranges from 4 to 11% in Hannover and from 6 to 9% in Golden. Vertical PV modules facing north show the largest rMAD of between 6 and 21% in Hannover and between 14 and 29% in Golden.

Article

Comparison of Modelled and Measured Tilted Solar Irradiance for Photovoltaic Applications

Riyad Mubarak ^{1,*}, Martin Hofmann ^{1,2} , Stefan Riechelmann ³ and Gunther Seckmeyer ¹ 

¹ Institute for Meteorology and Climatology, Leibniz Universität Hannover, Herrenhäuser Straße 2, 30419 Hannover, Germany; martin.hofmann@valentin-software.com (M.H.); Seckmeyer@muk.uni-hannover.de (G.S.)

² Valentin Software GmbH, Stralauer Platz 34, 10243 Berlin, Germany

³ Physikalisch-Technische Bundesanstalt (PTB), Bundesallee 100, 38116 Braunschweig, Germany; stefan.riechelmann@ptb.de

* Correspondence: mubarak@muk.uni-hannover.de

Received: 9 August 2017; Accepted: 16 October 2017; Published: 25 October 2017

Abstract: This work assesses the performance of five transposition models that estimate the global and diffuse solar irradiance on tilted planes based on the global horizontal irradiance. The modelled tilted irradiance values are compared to measured one-minute values from pyranometers and silicon sensors tilted at different angles at Hannover (Germany) and NREL (Golden, CO, USA). It can be recognized that the deviations of the model of Liu and Jordan, Klucher and Perez from the measurements increases as the tilt angle increases and as the sensors are oriented away from the south direction, where they receive lower direct radiation than south-oriented surfaces. Accordingly, the vertical E, W and N planes show the highest deviation. Best results are found by the models from Hay and Davies and Reindl, when horizontal pyranometer measurements and a constant albedo value of 0.2 are used. The relative root mean squared difference (rRMSD) of the anisotropic models does not exceed 11% for south orientation and low inclination angles ($\beta = 10\text{--}60^\circ$), but reaches up to 28.9% at vertical planes. For sunny locations such as Golden, the Perez model provides the best estimates of global tilted irradiance for south-facing surfaces. The relative mean absolute difference (rMAD) of the Perez model at NREL ranges from 4.2% for 40° tilt to 8.7% for 90° tilt angle, when horizontal pyranometer measurements and a measured albedo value are used; the use of measured albedo values instead of a constant value of 0.2 leads to a reduction of the deviation to 3.9% and 6.0%, respectively. The use of higher albedo values leads to a significant increase of rMAD. We also investigated the uncertainty resulting from using horizontal pyranometer measurements, in combination with constant albedo values, to estimate the incident irradiance on tilted photovoltaic (PV) modules. We found that these uncertainties are small or negligible.

Keywords: incident solar radiation; transposition models; isotropic models; anisotropic models; tilted surface

1. Introduction

To estimate the expected energy output of a PV system, yield estimation models are used which need specific input parameters such as global solar irradiance. Since small uncertainties in the model parameters can lead to large deviations from the expected returns on investment, uncertainties resulting from model input should be reduced as much as possible.

Estimating solar irradiation incident on tilted surfaces of various orientations is essential to estimate the electric power generated by PV, to design solar energy systems and to evaluate their long-term average performance [1]. However, the available measurement data are suboptimal, since global horizontal or diffuse horizontal irradiance measurements provided by pyranometers are often

the only available measurements at most locations. Even if tilted measurements are performed, the tilt angle chosen for the measurement is not necessarily the optimal tilt angle for the location. Consequently, the tilted solar irradiance must be determined by converting the solar irradiance on a horizontal surface to that incident on the tilted surface of interest [2].

Transposition models based on global and diffuse horizontal irradiance have been widely used in the solar energy industry to estimate the solar irradiance incident on tilted PV panels. The transposition models parametrize the irradiance on a tilted plane to three components: direct, diffuse and ground reflected radiation. The direct radiation can be computed by the geometrical relationship between the horizontal and tilted surfaces. The ground reflected radiation can be estimated with the aid of an isotropic model by using simple algorithms. The assumption of isotropy may be justified for estimating the influence of the albedo but is problematic for the diffuse component. This is due to the complexity of the angular dependence of the diffuse component, which depends on many factors such as solar zenith angle and clouds [3]. The continuing evolution and diversity of transposition models illustrates the complexity of the task.

Early models converted the horizontal diffuse radiation to the tilted plane by assuming that the total sky diffuse radiation is distributed isotropically over the sky dome [4–6]. However, this assumption is too simple and is inconsistent with reality. Newer transposition models treat the diffuse component as anisotropically distributed. Several anisotropic models only consider an isotropic background and an additional circumsolar region; others also take the horizon-brightening into account. However, this assumption is only valid in the absence of clouds as in overcast situations the horizon tends to be darker than the zenith [7].

Many authors have studied the accuracy of transposition models by comparing the modelled irradiance with measured values in different climate conditions. Kambezidis et al. [8] used twelve sky diffuse models to calculate the global irradiance on a south-facing surface tilted at 50° in Athens, Greece. Furthermore, four albedo models were used to assess the albedo of the measurement location. The performance of models was evaluated against hourly measurements of global solar irradiance. The transposition models proposed by Gueymard [9], Hay [10], Reindl [11], and Skartveit and Olseth [12] were found to have the best overall performances, in conjunction with either one of three albedo sub-models.

Notton et al. [13] evaluated the performance of 15 transposition models against measured hourly data for two tilted surface angles (45° and 60°) in Ajaccio, France. Among the tested models, the Perez model shows the best accuracy. The authors chose a constant value of 0.2 for the albedo as the most commonly used value in the literature for visible radiation. Gueymard et al. [14] have shown that the deviation between measured and modelled irradiance depends on the uncertainty of the global horizontal irradiance, ground albedo and other factors. Gueymard [15] compared ten transposition models that were appraised against one-minute global irradiance measured on fixed-tilt, south-facing planes (40° and 90°) and a two-axis tracker at NREL's Solar Radiation Research Lab. in Golden (CO, USA). They found that the Gueymard and Perez models provide the best estimates of global irradiance incident on tilted surfaces for sunny sites only when optimal input data (measured direct, diffuse and albedo) are used. When only global irradiance is known, the accuracy of the predicted tilted irradiance degrades significantly. Yang [16] compared the performance of 26 transposition models using 18 case studies from four sites in the USA, Germany and Singapore. Various error metrics, linear ranking, and hypothesis testing were employed to quantify the model performance. Results of the pairwise Diebold-Mariano tests concluded that no single model was universally optimal. However, he found that according to the linear ranking results on rRMSE the top four families of models are Perez, Muneer, Hay, and Gueymard.

Furthermore, there are several studies that have concentrated on the solar radiation on vertical surfaces for building application. Li et al. [17], Cuomo et al. [18], and Chirarattananon et al. [19] evaluated various models to estimate the global solar radiation on vertical surfaces. These studies have indicated that the Perez model delivers better predictions for all orientations. Loutzenhiser et al. [20]

assessed seven radiation models on inclined surfaces that were implemented in building energy simulation codes. Among the models tested in this study are the models of Hay [10] and Perez [21]. These studies revealed that even in the same region, the uncertainties of the solar radiation model were found to vary according to the direction and slope of the surface. Many other studies [22–26] have been conducted in the last two decades to evaluate transposition models and the results show that the performance of models varies, depending on the quality of the input data, the surface orientation and the measurement location.

However, no significant research has been found on how the model sensitivity is affected by using horizontal pyranometer irradiance to estimate the irradiance incident on tilted PV modules, which have different spectral and angular responses, and non-negligible temperature responses. There are also little published research about the systematic error that can be introduced.

In this study, five irradiance transposition models [4,10,11,21,27] are used to calculate the irradiance received on tilted surfaces with various tilt elevation and azimuth angles. We examined model performance for seven south-facing PV surfaces tilted at 10° intervals from 10° to 70°, six vertical tilted surfaces facing north, east, southeast, south, southwest, and west and a horizontally oriented surface. The models were chosen because they are widely used and their required input data are readily available. The validation is conducted with measurement data derived from tilted irradiance sensors, located at two different locations to derive results that hold a more general significance and are more spatially applicable. Furthermore, we investigate the uncertainties caused by the use of horizontal pyranometer measurements to compute the irradiance absorbed by the tilted PV array and the uncertainty from the use of constant albedo value in the calculations.

2. Instruments and Methods

The input data used in this study are one-minute irradiance data measured in two independent locations.

2.1. IMUK Measurements

Various irradiance measurements were performed for three years (January 2014–December 2016) on the roof of the Institute for Meteorology and Climatology (IMUK) of the Leibniz Universität Hannover (Hannover, Germany; 52.23° N, 09.42° E and 50 m above sea level).

The following irradiance measurements were conducted:

1. Global Horizontal Irradiance (GHI) from January 2014 to December 2016, measured by a CMP11 pyranometer (Kipp & Zonen, Delft, The Netherlands),
2. Diffuse Horizontal Irradiance (DHI) from January 2014 to December 2016, measured by a CMP11 pyranometer with a shadow ball (Figure 1a),
3. Global Tilted Irradiance (GTI) measured at a 40° inclined plane facing south by a CM11 pyranometer from January to December 2016,
4. Global Tilted Irradiances from January 2014 to December 2016 measured by at various orientations by 14 crystalline silicon PV device with individual temperature sensors (Mencke & Tegtmeyer GmbH, Hameln, Germany). Seven of those silicon sensors (SiS) were facing south, tilted at 0°, 10°, 20°, 30°, 40°, 50°, 60°, 70°, six sensors were tilted vertically facing N, S, E, W, SE and SW and a single sensor was oriented horizontally (Figure 1b).

All sensors are cleaned regularly to prevent the accumulation of dirt and dust. The silicon sensors have been calibrated by the manufacturer in November 2013. In addition, all SiS's at IMUK are compared after one year of measurements by placing them side by side horizontally. These comparisons were performed under different weather conditions and have showed an agreement within ±3%.



Figure 1. (a) Pyranometers and other instruments available and operational at Institute for Meteorology and Climatology (IMUK); (b) Set of solar sensors based on silicon detectors mounted in several different tilt angles and orientations, operational at the IMUK (IMUK 2017).

2.2. NREL Measurements

The NREL irradiance measurements were acquired at NREL's Solar Radiation Research Laboratory in Golden, CO, USA (latitude 39.74° N, longitude 105.18° W, elevation 1829 m). This NREL site is located on a mesa that overlooks the western side of the urban agglomeration of Denver. The data have been obtained from SRRL's download tool, http://www.nrel.gov/midc/srrl_bms for the period from March 2015 to December 2016. The NREL data includes the following values:

- 1 Global Horizontal Irradiance (GHI) measured by a CMP11 pyranometer,
- 2 Diffuse Horizontal Irradiance (DHI), measured by a CMP11 pyranometer,
- 3 Global Tilted Irradiance (GTI) measured at a 40° inclined plane facing south by a CMP11 pyranometer,
- 4 Global Tilted Irradiances measured by a silicon pyranometer LI-200 (LI-COR Inc., Lincoln, NE, USA), facing S, tilted at 40° and vertically tilted sensors facing N, S, E and W,
- 5 Albedo measurements, measured by two silicon pyranometers LI-200.

2.3. Preprocessing and Quality Control

The following quality control procedure was applied to the IMUK data: Using Equation (1) we corrected the irradiance measured with the SiS's at IMUK based on their temperature coefficient to take in account the drop of sensor signal due to temperature and to correct the testing conditions:

$$I = U_{sen} \times 1000 / U_{cal} / (1 + \alpha \times (T - 25^\circ \text{C})), \quad (1)$$

where I is the corrected solar irradiance, U_{sen} is the signal in (mV), U_{cal} is the calibrated value in $\text{mV}/(1000 \text{ W}/\text{m}^2)$, T is the sensor temperature, and α represents the temperature coefficient.

In addition to the temperature correction, the cosine error of the silicon sensors is determined and the optical reflectance losses were corrected by using the model of Martin and Ruiz [28]. Only GHI and DHI values recorded at solar zenith angles (SZA) less 85° were used. All GHI and DHI values less than $0 \text{ W}/\text{m}^2$ were removed from the analysis, since these values were likely erroneous measurements. Furthermore, any DHI measurement that exceeded the concurrent GHI measurement was set equal to the GHI measurement because it is not physically possible for DHI to exceed GHI [29]. NREL radiation values have been processed with the SERI-QC quality control software developed by NREL. SERI QC assesses the quality of solar radiation data by comparing measured values with expected values. This procedure is based on the relationship between global and direct solar radiation [30].

2.4. Transposition Models

The global tilted irradiance I_T is estimated by the sum of the beam tilted $I_{t,b}$, sky diffuse tilted $I_{t,d}$, and ground-reflected I_g irradiances:

$$I_T = I_{t,b} + I_{t,d} + I_g \quad (2)$$

Five models are selected in this study to estimate the global and diffuse solar irradiance on tilted planes based on the global and diffuse horizontal irradiance. The models are from Liu and Jordan, Klucher, Hay and Davies, Reindl and Perez. Those models have been selected since they are widely used, the necessary input data are available at the examined measurement site, and because they present the three most common model types: isotropic, anisotropic with two components and anisotropic with three components. A brief description of the selected models is given below.

2.4.1. Liu and Jordan Model

The Liu and Jordan model [4] is a simple model that assumes all diffuse sky radiation is uniform over the sky dome and that reflection on the ground is diffuse. For surfaces tilted by an angle β from the horizontal plane, total solar irradiance can be written as:

$$I_T = I_{h,b}R_b + I_{h,d}\left(\frac{1 + \cos \beta}{2}\right) + I_h\rho\left(\frac{1 - \cos \beta}{2}\right) \quad (3)$$

where I_T is the tilted irradiance, $I_{h,b}$ the beam irradiance on a horizontal surface, R_b the ratio of beam radiation on the tilted surface to that on a horizontal, $I_{h,d}$ the diffuse horizontal irradiance, β the tilt angle, I_h the global horizontal irradiance, and ρ the ground reflectance.

2.4.2. Klucher Model

Klucher found that Liu and Jordan's isotropic model gave good results only for overcast skies. However, it underestimates the irradiance under clear and partly overcast conditions, when there is increased intensity near the horizon and in the circumsolar region of the sky [27]. He developed therefore an anisotropic model by modifying the isotropic model, to take into account the horizontal and circumsolar brightening:

$$I_T = I_{h,b}R_b + I_{h,d}\left(\frac{1 + \cos \beta}{2}\right) [1 + F \sin^3\left(\frac{\beta}{2}\right)] \times [1 + F \cos^2 \theta \sin^3 \theta_z] + I_h\rho\left(\frac{1 - \cos \beta}{2}\right) \quad (4)$$

$$F = 1 - \left(\frac{I_{h,d}}{I_h}\right)^2 \quad (5)$$

F is the Klucher modulating factor. Under overcast skies, F becomes zero and the model reduces to the Liu & Jordan model.

2.4.3. Hay and Davies Model

The Hay and Davies diffuse model divides the sky diffuse irradiance into isotropic and circumsolar components only [31]. The horizon brightening was not taken into account:

$$I_T = (I_{h,b} + I_{h,d}A)R_b + I_{h,d}(1 - A)\left(\frac{1 + \cos \beta}{2}\right) + I_h\rho\left(\frac{1 - \cos \beta}{2}\right) \quad (6)$$

$$A = \frac{I_{bn}}{I_{on}} \quad (7)$$

A represents the transmittance of beam irradiance through the atmosphere, where I_{bn} is the direct-normal solar irradiance and I_{on} the direct extraterrestrial normal irradiance.

2.4.4. Reindl Model

The Reindl sky diffuse irradiance model represents three components of diffuse irradiance, including isotropic background, circumsolar brightening, and horizon brightening [11]:

$$I_T = (I_{h,b} + I_{h,d}A)R_b + I_{h,d}(1 - A)\left(\frac{1 + \cos \beta}{2}\right) \times \left[1 + \sqrt{\frac{I_{h,b}}{I_h}} \sin^3\left(\frac{\beta}{2}\right)\right] + I_h\rho\left(\frac{1 - \cos \beta}{2}\right) \quad (8)$$

A is the transmittance of beam radiation through the atmosphere defined in Equation (6).

2.4.5. Perez Model

Perez model represents a more detailed analysis of the sky diffuse radiation. The model, like the Klucher and the Reindl models, divided the diffuse irradiance into three components of isotropic background, circumsolar brightening and horizon brightening [21]:

$$I_T = I_{h,b}R_b + I_{h,d}\left[(1 - F_1)\left(\frac{1 + \cos \beta}{2}\right) + F_1\frac{a}{b} + F_2 \sin \beta\right] + I_h\rho\left(\frac{1 - \cos \beta}{2}\right) \quad (9)$$

where, F_1 and F_2 are circumsolar and horizon brightness coefficients, respectively; a and b are solid angles corresponding to the circumsolar part as seen from the inclined plane. The terms a and b are computed as:

$$a = \max(0, \cos \theta) \quad (10)$$

$$b = \max(\cos 85^\circ, \cos \theta_z) \quad (11)$$

F_1 and F_2 in Equation (9) are functions of clearness ϵ , zenith angle θ_z and brightness Δ . These factors are defined as:

$$\epsilon = \frac{\frac{I_{h,d}+I_{bn}}{I_{h,d}} + 5.535 \times 10^{-6} \theta_z^3}{1 + 5.535 \times 10^{-6} \theta_z^3} \quad (12)$$

$$\Delta = m \frac{I_{h,d}}{I_{on}} \quad (13)$$

The coefficients F_1 and F_2 are then computed as:

$$F_1 = \max\left[0, \left(f_{11} + f_{12}\Delta + \frac{\pi\theta_z}{180}f_{13}\right)\right] \quad (14)$$

$$F_2 = f_{21} + f_{22}\Delta + \frac{\pi\theta_z}{180}f_{23} \quad (15)$$

The coefficients f_{11} , f_{12} , f_{13} , f_{21} , f_{22} and f_{23} were derived based on a statistical analysis of experimental data for different locations (Table 1).

Table 1. Perez model coefficients for various values of clearness ϵ .

ϵ	f_{11}	f_{12}	f_{13}	f_{21}	f_{22}	f_{23}
[1, 1.065]	-0.008	0.588	-0.062	-0.06	0.072	-0.022
[1.065, 1.23]	0.13	0.683	-0.151	-0.019	0.066	-0.029
[1.23, 1.5]	0.33	0.487	-0.221	0.055	-0.064	-0.026
[1.5, 1.95]	0.568	0.187	-0.295	0.109	-0.152	-0.014
[1.95, 2.8]	0.873	-0.392	-0.362	0.226	-0.462	0.001
[2.8, 4.5]	1.132	-1.237	-0.412	0.288	-0.823	0.056
[4.5, 6.2]	1.06	-1.6	-0.359	0.264	-1.127	0.131
[6.2, ∞]	0.678	-0.327	-0.25	0.156	-1.377	0.251

The ability of models to estimate the solar irradiance incident on tilted surfaces is analyzed by means of the relative Root Mean Square Difference (rRMSD), relative Mean Absolute Difference (rMAD) and relative Mean Bias Difference (rMBD). These parameters are calculated using Equations (16)–(21):

$$RMSD = \sqrt{\frac{\sum (Mi - Ci)^2}{n}} \quad (16)$$

$$rRMSD = \frac{RMSD}{\bar{M}} 100\% \quad (17)$$

$$MAD = \frac{\sum |(Mi - Ci)|}{n} \quad (18)$$

$$rMAD = \frac{MAD}{\bar{M}} 100\% \quad (19)$$

$$MBD = \frac{\sum (Mi - Ci)}{n} \quad (20)$$

$$rMBD = \frac{MBD}{\bar{M}} 100\% \quad (21)$$

where Mi is the measured irradiance on an inclined plane and Ci the calculated model value.

3. Results and Discussion

3.1. Measurement Validation

The two most devices used by the PV industry for measuring the solar irradiance are thermopile pyranometers and small solar cells (silicon sensors). Of the latter, only crystalline silicon (cSi) sensors provide the required stability [32].

Thermopile pyranometers are devices that consist of junctions of dissimilar metals in contact with a black surface that absorbs solar radiation (the “hot” junction) and a separate surface that does not absorb solar radiation (the “cold” junction). Pyranometers have a uniform spectral response from about 280 to about 2800 nm. They are widely used for meteorological measurements and nearly all existing irradiation databases are validated using these measurements [32].

Unlike pyranometers, silicon sensors convert incident irradiance to electrons through the photovoltaic effect. The silicon sensors are spectrally selective in the range of about 350 to about 1100 nm (Figure 2). The shorter wavelength is determined by the transmission of the front glass and encapsulant, whereas the longer wavelength is determined by the material’s band gap [33]. Table 2 provides a comparison of basic specifications between the sensors used in this study.

Table 2. Comparison of the specifications of the sensors used.

Specifications	Pyranometer CMP11	Silicon Sensor SiS	Silicon Sensor Li-200
Spectral sensitivity range (nm)	285–2800	350–1100	350–1100
Response time (s)	5	<0.001	<0.001
Offset (W/m^2)	2	0	0
Temperature dependence (−10–40 °C) (%)	<1	0.2	±0.15
Uncertainty (W/m^2)	<5	± 5	<5
Non-linearity (100 to 1000 W/m^2) (%)	<0.5	±0.5	<1.0

Due to the different spectral response the highest absolute difference between the signal measured by a silicon sensor and a thermopile pyranometer is at clear sky conditions with a low diffuse to direct ratio [34]. Silicon sensors are fundamentally photovoltaic devices, and as such, standard American Society for Testing and Materials (ASTM) test procedures are applied to calibrate them by using a solar simulator [35].

The difference in cosine error is considered as the second important factor that sets apart the two devices. Silicon sensors have in general a higher cosine error than thermopile pyranometers [36] and therefore underestimate radiance incident from steep angles.

The difference between the sensors (see Table 2) affects the measured irradiance, as shown in Figure 3. The sensitivity of silicon sensors shows an increase during summer months, when SZAs are low compared to the winter months. The ratio of measured irradiance between the pyranometers and silicon the sensors is higher in winter. The right plots of Figure 3 show the ratios of daily horizontal irradiance measured by both sensors. The annual pyranometer irradiance at both sites is higher than the irradiance derived by the silicon sensors. At NREL, the pyranometer irradiance is higher in winter months, while irradiance measured by the Li-200 sensor is higher in summer. However, the behavior of silicon sensors against pyranometer measurements in both locations is the same, the relative sensitivity of the silicon sensors increases during the summer months.

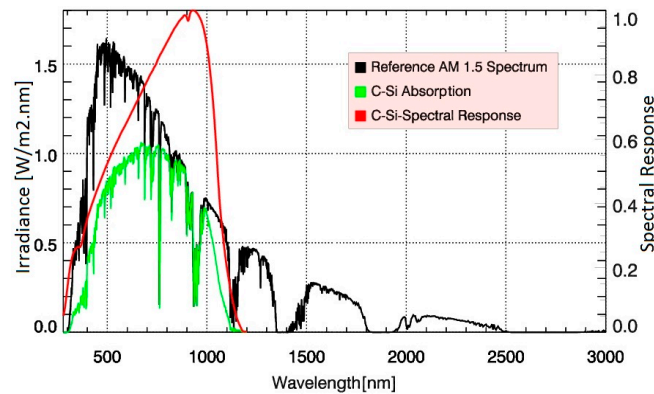


Figure 2. Global solar spectrum at air mass 1.5 (black) and the portion absorbed by a silicon device (green). The silicon sensors (SiS) can measure up to 1200 nm (compare the c-Si spectral response (red)), while the pyranometer measures up to about 2800 nm.

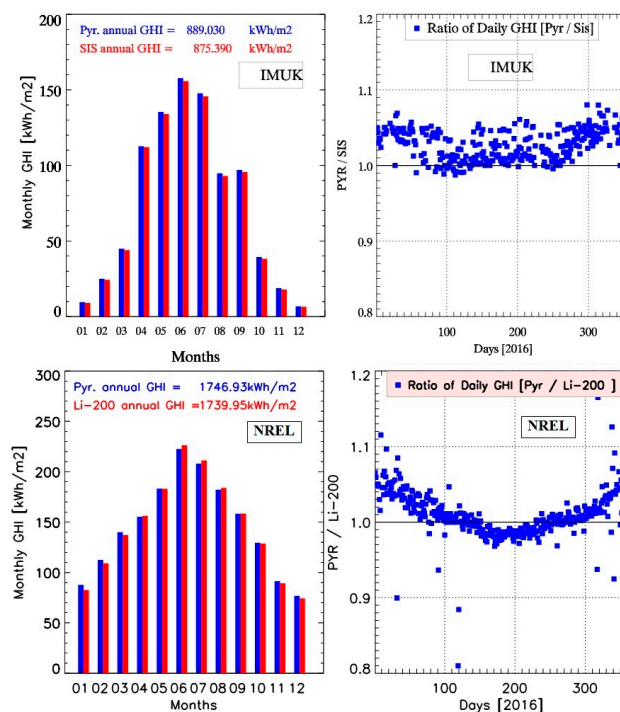


Figure 3. [Top plots] Monthly global horizontal irradiance (GHI) measured by thermopile pyranometers and silicon sensors (SiS) on horizontal surface (left) and the ratios of daily irradiances measured by both sensors (right), for the location of IMuK. [Bottom plots] the same as the top plots but at NREL. The irradiance measured by silicon sensors shows an increase during the summer months.

In the following we investigate the uncertainties associated with the use of different irradiance sensors and assumption of albedo values as the major contributors to the uncertainty.

3.1.1. Uncertainty Resulting from Using Different Sensors

Low uncertainty of the measurements is a key factor for the quality of the data. For many applications, including predictions for a return of investment, it is important to know the uncertainties resulting from using sensors of various types to measure horizontal and tilted irradiance.

In this regard, it makes sense to use the statistical indices to compare the horizontal measurements from different technologies of solar sensors. Figure 4 shows the monthly and the annual rRMSD, rMBD and rMAD between the horizontal irradiances measured by the pyranometer and the silicon sensors at both sites in 2016. The annual rRMSD and the rMBD values at IMUK are 5.2% and 3.5% respectively. The differences are largest in the winter months, as the measured signal is low and are slightly lower with increasing irradiance in the summer months. The differences between the NREL's sensors are smaller, where the annual rRMSD is 3.6% and the rMBD is 1.1%. The monthly average in the left plot shows the same behavior at NREL with negative rMBD values during the summer months (June–September). This agrees with Figure 3, where irradiance measured by the Li-200 sensor is higher in summer than the pyranometer values.

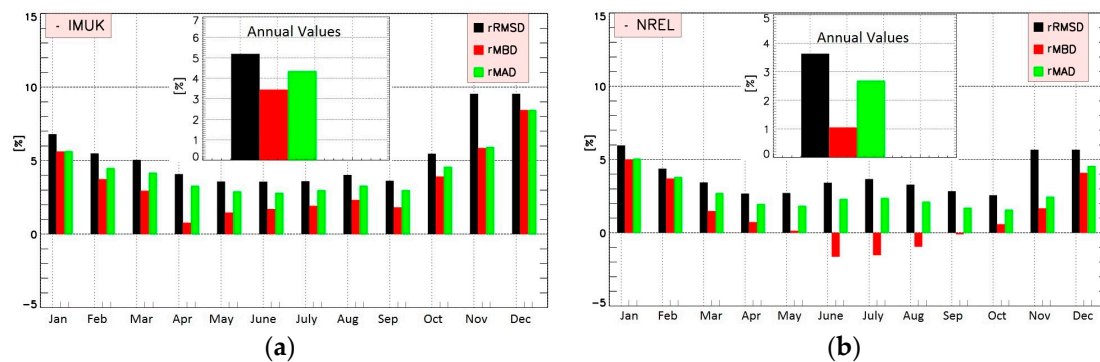


Figure 4. Monthly and annual average of the statistical indices relative Root Mean Square Difference (rRMSD), relative Mean Absolute Difference (rMBD) and relative Mean Bias Difference (rMAD) between pyranometer and silicon sensor measurements at IMUK (a) and at NREL (b). The statistical indices show clear differences in the magnitude and show a seasonal dependence.

Based on these results, it is important to investigate how the differences in the horizontal measurements of different sensors affect the calculated tilted irradiance.

For this purpose, horizontal pyranometer measurements from 2016 were used to calculate the tilted irradiance at 40° S. The results were compared with tilted irradiance measured by: (1) tilted thermopile pyranometer and (2) tilted silicon sensor (SIS) at 40° S. The rMAD resulting from the comparison with SIS values ranges from 5.1% (Reindl) to 8.4% (Liu and Jordan). The comparison with Pyranometer values leads to slightly lower differences of 5.1% and 6.5%, respectively (Figure 5). The Liu and Jordan model and the Perez model are affected more when using different instruments whereas the model of Hay and Davies and Reindl were almost unaffected. These values are for 40° S tilt, the other orientations could not be tested, because there is only one tilted pyranometer (40° S) at IMUK.

Thus, it can be concluded, that a systematic error is introduced when using horizontal pyranometer measurements to compute the irradiance absorbed by tilted PV modules, which have different spectral, angular, and temperature responses. Depending on the used model, this error has only a small or even no influence on the calculated irradiance on a tilted PV surface.

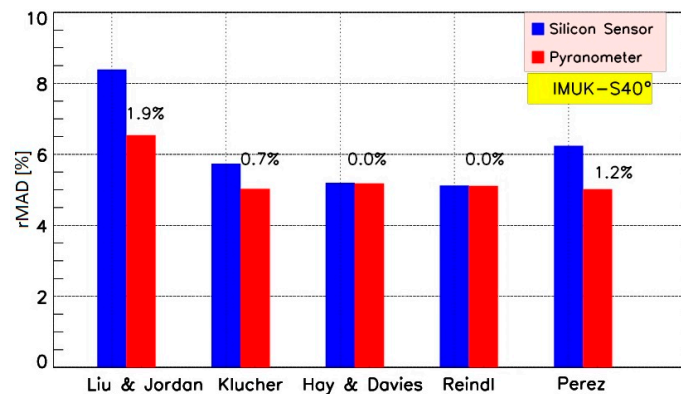


Figure 5. Dependence of the rMAD on the used sensor for the five transposition models. The performance of models is better if the model input data (GHI) and validation data (GTI) are measured by sensors of the same type.

3.1.2. Albedo and Seasonal Effects

The accuracy of ground reflection calculations depends strongly on the knowledge of albedo values used in the models; the dependence becomes stronger as the tilt angle increases [15]. Only in rare cases ground albedo is known accurately; in most cases a constant value for albedo is used by the model.

It is useful to evaluate the uncertainty that results from using a spectrally constant albedo for calculating the tilted irradiance. For this purpose, measured albedo values and different constant values (0.2, 0.4, 0.6 and 0.9) are used to calculate the tilted irradiance on 40° and 90° tilt based on NREL data. The rMAD is used to evaluate the prediction of the models for each albedo value (Figure 6).

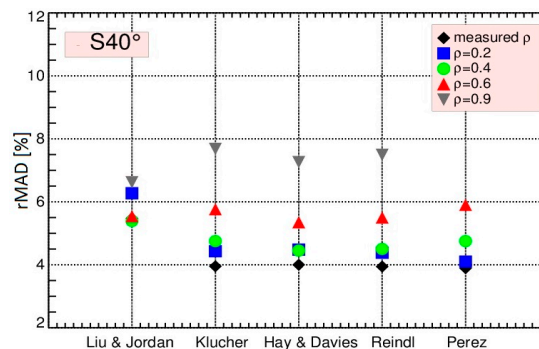


Figure 6. Dependence of the rMAD for the five models on the spectrally constant ground albedo. The tilted irradiance has been calculated based on NREL data for 40° S tilt, using different constant albedo values (0.2, 0.4, 0.6 and 0.9) and measured values at NREL. The models show lower deviations to the measurement if measured albedo values are used.

Figure 6 shows that the models are more accurate if measured albedo values are used. The rMAD increases as the albedo value increases. The use of constant albedo value of 0.2 (the most used value for models) leads to an increase of the rMAD of between 0.2% (Perez) and 0.8% (Liu and Jordan). The Figure 6 also shows that the Liu and Jordan model is less dependent on the albedo. This may be explained by the assumption of isotropic distribution of diffuse irradiance in this model.

The same calculations were done for 90° S tilt (Figure 7). It is easy to recognize that the influence of albedo on the calculated tilt irradiance is much larger. The use of a constant value of 0.2 instead of a measured value increases the rMAD by about 2.5% (Perez model) and 3.8% (Liu and Jordan). The rMAD increases also with increasing albedo values.

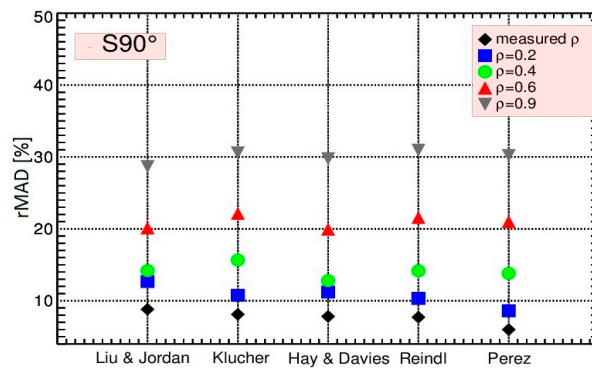


Figure 7. Same as Figure 6, but for 90° S. The rMAD increase as the albedo value increases. The plot illustrates albedo values on vertical tilted irradiance.

3.2. Model Validation

In order to evaluate the model performance and to consider the influence of some input parameters on the results, we use measured horizontal irradiances (global and diffuse) to calculate the tilted irradiance at different orientations and tilt angles. The calculated values are compared with one-minute values from irradiance sensors facing the same orientation and tilt angles. The global and diffuse horizontal input values are measured at both sites by thermopile pyranometers. Furthermore, tilted pyranometers are used to measure the tilted global irradiance at 40°. Tilted irradiance at IMUK has been measured by silicon sensors (SiS) at 14 different orientations and tilt angles. At NREL, the tilted irradiance at 40° and at different vertical planes (E, W, S, N) were measured by another silicon device (Li-200). The measurements and the corresponding instruments are shown in details in Table 3.

Table 3. Components and data used for comparisons between measurements and models.

Measurements			Model			
Parameter	Description	Measuring Sensor	Parameter	Description	Inputs	Measuring Sensor
GTI south facing (IMUK)	Tilt: 10°, 20°, 30°, 40°, 50°, 60°, 70°	SiS	GTI south facing	Tilt: 10°, 20°, 30°, 40°, 50°, 60°, 70°	GHI DHI Albedo	CMP11 CMP11 Const. 0.2
GTI Vertical (IMUK)	E, S, W, N, SE, SW	SiS	GTI Vertical	E, S, W, N, SE, SW	GHI DHI Albedo	CMP11 CMP11 Const. 0.2
GTI south facing (IMUK)	Tilt: 40°	CMP11	GTI south facing	Tilt: 40°	GHI DHI Albedo	CMP11 CMP11 Const. 0.2
GTI south facing (NREL)	Tilt: 40°	Li-200	GTI south facing	Tilt: 40°	GHI DHI Albedo	CMP11 CMP11 Li-200
GTI Vertical (NREL)	E, S, W, N	Li-200	GTI Vertical	E, S, W, N	GHI DHI Albedo	CMP11 CMP11 Li-200
GTI south facing (NREL)	Tilt: 40°	CMP11	GTI south facing	Tilt: 40°	GHI DHI Albedo	CMP11 CMP11 Li-200
GTI south facing (NREL)	Tilt: 40°	Li-200	GTI south facing	Tilt: 40°	GHI DHI Albedo	CMP11 CMP11 Li-200
GTI Vertical (NREL)	S	Li-200	GTI Vertical	S	GHI DHI Albedo	CMP11 CMP11 Li-200

The results of the five models are shown in Table 4, for all available orientations and tilt angles of IMUK. It can be recognized that the deviations of the model of Liu and Jordan, Klucher and Perez from the measurements increases as the tilt angle increases and as the sensors are oriented away from the

south direction, where they receive much less direct radiation than south-facing surfaces. Accordingly, the vertical E, W and N planes show the highest deviation. In general, the best results in terms of rRMSD and rMAD are obtained with the Hay and Davies and Reindl models, while the isotropic model of Liu & Jordan provide the worst agreement for south facing planes (Figure 8).

For the vertical tilt planes, the Hay and Davies model obtains the lowest RMSD. The Klucher transposition model is most affected by errors when facing away from the south direction. The high deviation of the vertical sensors can be related to the significant change in the ratio I_d/I_h for the vertical tilt and also to the incorrect modelling of ground reflection.

It has also been observed that the anisotropic models overestimate the south-tilted irradiances (MBD ranging from -0.52 to -3.63%) and most of the vertical irradiances (MBD ranging from 3.47 to -20.1%). In contrast, the Liu and Jordan model underestimates the tilted irradiance in most directions, but not at very low tilt or on vertical surfaces away from the south quadrant.

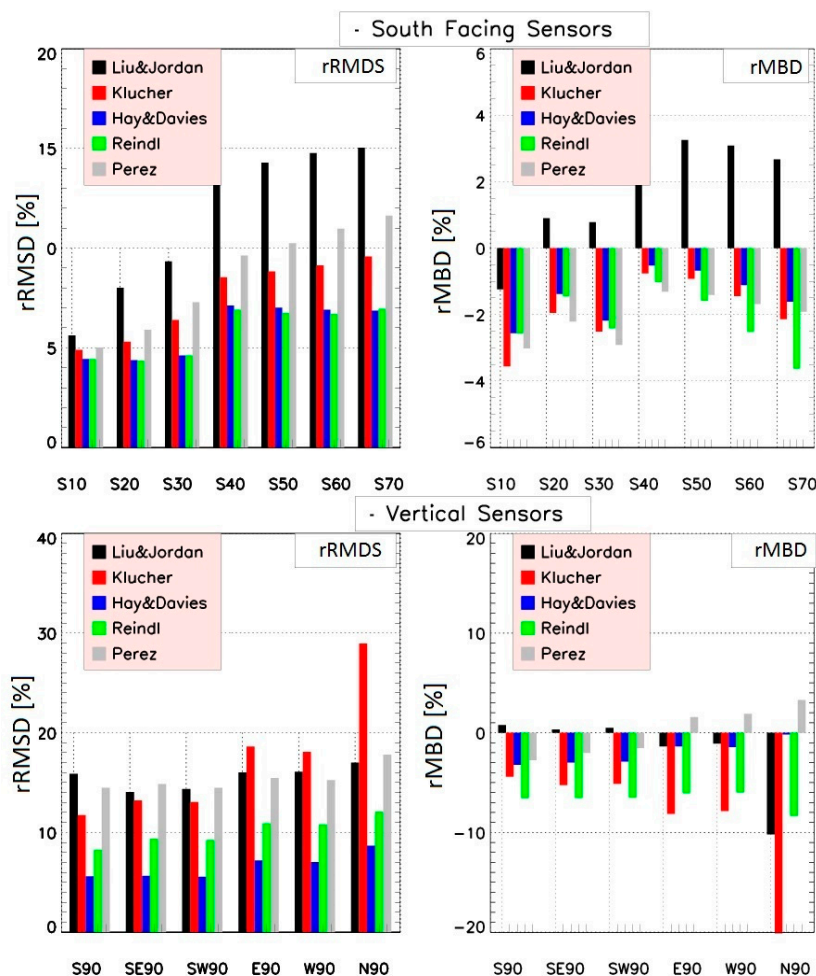


Figure 8. Root mean square difference (left) and mean bias difference (right) between model and measurements at IMUK for all south facing sensors (upper plots) and vertical sensors (lower plots). The difference increases, as the tilt angle increase.

According to the data from NREL (Table 5), the Perez model provides the best results for S and N directions, while the models of Reindl and Hay and Davies provide the lowest rRMSD for E and W orientations, which agrees with the IMUK results. The rMBD of rNREL values show that the models of Klucher and Perez overestimate the calculated irradiance (MBD ranging from -0.45 to -16.7%), while the rMBDs of the other models range between positive and negative, depending on the azimuth angle (Figure 9).

The difference in model performance between IMUK and NREL can be explained by two factors. First, by the different climates of the sites; the sky at IMUK is mostly cloudy, while NREL is a sunny site; Second, the quality of model input data; the GHI and DHI were measured by different sensors and measured albedo values are used for modelling the NREL data, which influences the calculated vertical irradiance significantly.

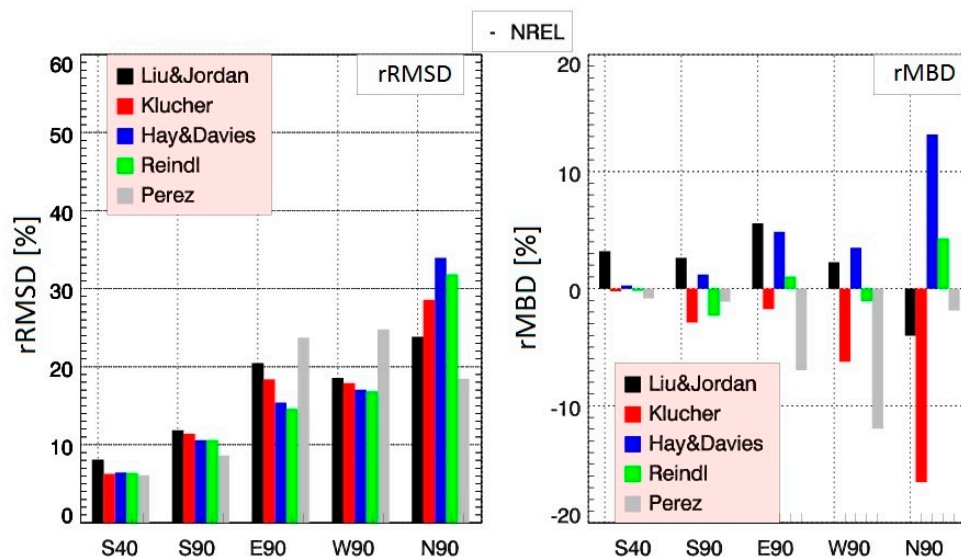


Figure 9. Root mean square difference (left) and mean bias difference (right) between model and measurements at NREL for all available orientations.

The accuracy of the modelled global tilted irradiance depends basically on two things: the availability of measured irradiance, which is a requirement for any model [14] and the accuracy of the model itself, in other words, the ability of the model to simulate the irradiance distribution in the atmosphere. It is therefore important to evaluate the uncertainty resulting from the input data of the model before evaluating the performance of the models. The measured horizontal irradiance components (global, diffuse, direct) constitute the most important input data to compute the tilted irradiance. Modelling of tilted irradiance would be ideal if measurements for all irradiance components, including ground reflectance, were available. This would avoid uncertainties that result from estimation of one component from the other two. The modelling of tilted irradiance would be less ideal but still useful if two of them are available.

All presented models use the same method for calculating beam and ground reflected irradiance on a tilted surface; the differences lie only in the calculation of the diffuse radiation. The statistical analysis showed that the Reindl and Hay and Davies models produce the best agreement with the measured tilted data in Hannover. The results of both models are very similar, even although they differ in their modeling approach for the diffuse sky radiation. This may be because both models use the same anisotropic index to weight the circumsolar and isotropic components. Moreover, the horizon brightening component has a limited effect under cloudy conditions; it is most profound in clear skies [37].

Table 4. Performance of all five transposition models, compared to IMUK measurements.

IMUK	Liu & Jordan			Klucher			Hay & Davies			Reindl			Perez		
Azimuth/Tilt	rMBD	rMAD	rRMSD	rMBD	rMAD	rRMSD	rMBD	rMAD	rRMSD	rMBD	rMAD	rRMSD	rMBD	rMAD	rRMSD
ss10	-1.24	4.32	5.62	-3.56	4.06	4.98	-2.56	3.67	4.44	-2.57	3.67	4.44	-3.02	3.94	5.01
ss20	0.90	5.61	8.01	-1.95	4.08	5.30	-1.38	3.51	4.38	-1.45	3.51	4.36	-2.21	4.19	5.90
ss30	0.78	6.55	9.33	-2.51	4.95	6.39	-2.18	3.75	4.62	-2.41	3.77	4.61	-2.91	5.08	7.28
ss40	3.03	8.71	13.49	-0.76	6.54	8.54	-0.52	5.11	07.12	-1.02	5.04	06.91	-1.31	6.40	09.62
ss50	3.25	9.11	14.29	-0.92	6.20	08.83	-0.68	5.06	07.02	-1.58	5.01	06.74	-1.41	6.88	10.24
ss60	3.08	9.37	14.76	-1.44	6.46	09.13	-1.11	5.04	06.91	-2.52	5.15	06.70	-1.68	7.41	10.97
ss70	2.57	10.96	15.03	-2.14	6.47	09.58	-1.61	5.05	06.86	-3.63	5.16	06.95	-1.93	8.05	11.63
ss90	0.76	08.04	15.89	-4.41	08.04	11.74	-3.22	04.14	05.60	-6.57	6.70	09.27	-2.75	10.25	14.48
se90	0.32	08.56	14.06	-5.26	08.42	13.20	-2.99	04.00	05.64	-6.55	06.65	09.38	-2.02	10.73	14.85
sw90	0.50	08.70	14.36	-5.12	08.43	13.05	-2.98	03.96	05.55	-6.51	06.60	09.26	-1.54	10.43	14.47
ee90	-1.37	10.29	16.02	-8.14	12.66	18.63	-1.38	05.21	07.20	-6.07	07.69	10.92	1.57	11.36	15.46
ww90	-1.09	10.46	16.10	-7.86	12.50	18.09	-1.43	05.13	07.02	-6.01	07.67	10.80	1.98	11.27	15.24
nn90	-10.20	10.48	17.00	-20.13	20.28	28.94	-0.17	06.81	08.67	-8.34	08.97	12.08	3.47	14.45	17.81
pyr40	4.66	6.64	8.69	0.74	5.03	6.74	1.45	5.68	7.59	1	5.49	7.37	0.23	5.08	6.66

Table 5. Performance of all five transposition models, based on NREL data base.

NREL	Liu & Jordan			Klucher			Hay & Davies			Reindl			Perez		
Azimuth/Tilt	rMBD	rMAD	rRMSD	rMBD	rMAD	rRMSD	rMBD	rMAD	rRMSD	rMBD	rMAD	rRMSD	rMBD	rMAD	rRMSD
S 40	2.89	5.47	7.85	-0.45	3.95	6.08	0.08	4.0	6.26	-0.36	3.94	6.18	-0.96	3.98	6.0
S 90	2.40	8.81	11.76	-3.06	8.11	11.46	1.09	7.82	10.63	-2.41	7.72	10.68	-1.13	5.99	8.72
E 90	5.48	13.87	20.5	-1.75	13.1	18.64	4.70	11.18	15.50	0.91	10.5	14.8	-6.88	17.07	24.02
W 90	2.28	13.58	18.8	-6.1	13.25	18.2	3.50	13.49	17.3	-1.02	13.05	17.1	-11.78	17.75	25.15
N 90	-4.60	18.3	24.10	-16.7	21.00	29.05	12.33	28.20	33.78	3.47	25.85	31.8	-2.65	14.31	18.89

As expected, the isotropic Liu and Jordan model underestimates the tilted diffuse irradiance (positive MBD) for the south-facing planes, while it shows relatively good agreement with the measurement for the other orientations, when the irradiance is low. In contrast, the anisotropic models overestimate the irradiance at IMUK, with the three-component anisotropic models tending to overestimate the diffuse irradiance more than the two-component models.

The assumed distributions for diffuse sky irradiance and the nature of the anisotropic factors are what characterizes each of the anisotropic models used in this study. For the models of Klucher and Perez, it is possible that the climate at IMUK has some characteristics that require adjustment of the coefficients used in both model.

It can be concluded that the accurate calculation of the tilted diffuse solar irradiance is what distinguishes models from each other. Moreover, the basic criterion for selecting the most suitable model for simulating the electrical output of a PV module is its ability to simulate the diffuse radiation of the sky under all weather conditions. This can be understood if we consider that an inaccurately calculated diffuse irradiance can lead to significant over- or underestimations in the annual energy yield of a photovoltaic (PV) system by as much as 8% [38] even for horizontal orientations of the PV system.

4. Conclusions

Using one-minute measured GHI and DHI data, modeling was performed to calculate the tilted irradiance for different orientations and tilt angles in Hannover (Germany) and at NREL (Golden, CO, USA). The following conclusions can be drawn from this study:

- Best results are provided by the models from Hay and Davies and Reindl, when horizontal pyranometer measurements and a constant albedo value of 0.2 are used. This agreement of the two may relate to the anisotropic index used by both models to weight the circumsolar and isotropic components.
- The anisotropic models overestimate the south tilted irradiance and most of vertical tilted irradiance. In contrast, the isotropic model underestimates the tilted irradiance in most directions.
- For the NREL location, when measured albedo is used, the Perez model provides the best estimates of global tilted irradiance.
- The deviations of the anisotropic models from the measurements increase with increasing deviation from the south direction. In this case, the ratio of direct to diffuse radiation decreases and the uncertainty in modelling the diffuse irradiance becomes dominant.
- An uncertainty is introduced when using horizontal pyranometer measurements to estimate the irradiance absorbed by tilted PV modules. Depending on the used model, this uncertainty has only a small or even no effect on the calculated irradiance.
- The influence of albedo value on the calculated tilted irradiance increases as the tilt angle increases. The use of a constant albedo value of 0.2, which is widely accepted and used in most applications, leads to an increase in the rMAD that ranges between 0.2% and 0.8% at 40° tilt and reaches up to 3.8% at 90° tilt angle. If there are surfaces with higher reflectance in the vicinity of the PV system, rMAD is significantly higher.
- The models of Hay and Davies and Reindl is recommended to estimate the tilted irradiance for south-facing modules in regions with mainly cloudy conditions and when albedo measurements are not available. The Hay and Davies model would also be useful for vertical surfaces (e.g., facades and glazing) whereas the Perez model is recommended for sunny sites and when albedo measurements are available.

The spectral distribution of sky radiance is affected by clouds and aerosols. This has a significant influence on the performance of silicon sensors, where the spectral response of silicon sensors is wavelength-dependent. Therefore, additional spectral measurements are needed to understand the

behavior of silicon sensors in the different weather conditions. Therefore, advances in the modelling of PV yields require more knowledge about spectral radiance, which is known to be anisotropic.

Acknowledgments: The publication of this article was funded by the Open Access fund of Leibniz Universität Hannover. We are also grateful to Christian Melsheimer from IUP Bremen, Ben Liley, Richard McKenzie and Alex Geddes from NIWA for the useful comments.

Author Contributions: Riyadh Mubarak conceived and designed the study and wrote the draft paper; Martin Hofmann, Stefan Riechelmann and Gunther Seckmeyer contributed in conception and design, analysis and interpretation of the data. All the authors significantly contributed to the final version of the manuscript.

Conflicts of Interest: The authors declare no conflict of interest.

Nomenclature

Δ	sky's brightness, as in Perez model
ρ	ground albedo
β	tilt angle (rad)
θ	incidence angle (rad)
θ_z	solar zenith angle (rad)
ϵ	sky's clearness, as in Perez model [21]
a, b	sky geometry parameters, as in Perez model
A	transmittance of beam irradiance through atmosphere, as in Hay & Davies model
c-Si	crystalline silicon
F	Klucher's modulating factor
F_1, F_2	degree of circumsolar and horizon anisotropy, in the simplified Perez model
$f_{11}, f_{12}, f_{13}, f_{21}, f_{22}, f_{23}$	Perez model coefficients for irradiance
I_{bn}	direct-normal solar irradiance (DNI) (W/m^2)
$I_{h,b}$	beam horizontal irradiance (BHI) (W/m^2)
I_h	global horizontal irradiance (GHI) (W/m^2)
$I_{h,d}$	diffuse horizontal irradiance (DHI) (W/m^2)
$I_{t,b}$	beam tilted irradiance (BTI) (W/m^2)
$I_{t,d}$	diffuse tilted irradiance (DTI) (W/m^2)
I_g	ground-reflected irradiance (W/m^2)
I_{on}	direct extraterrestrial normal irradiance (W/m^2)
I_T	global tilted irradiance (GTI) (W/m^2)
MAD	mean absolute difference
MBD	mean bias difference
PV	photovoltaic
α	temperature coefficient
R_b	factor that accounts for direction of beam radiation,
RMSD	root mean square difference
SiS	silicon sensor

References

1. Mehleri, E.D.; Zervas, P.L.; Sarimveis, H.; Palyvos, J.A.; Markatos, N.C. A new neural network model for evaluating the performance of various hourly slope irradiation models: Implementation for the region of Athens. *Renew. Energy* **2010**, *35*, 1357–1362. [[CrossRef](#)]
2. Kudish, A.I.; Evseev, E.G. Prediction of solar global radiation on a surface tilted to the south. In Proceedings of the Optical Modeling and Measurements for Solar Energy Systems II, San Diego, CA, USA, 11 September 2008; p. 704603.
3. Riechelmann, S.; Schrempf, M.; Seckmeyer, G. Simultaneous measurement of spectral sky radiance by a non-scanning multidirectional spectroradiometer (MUDIS). *Meas. Sci. Technol.* **2013**, *24*, 125501. [[CrossRef](#)]
4. Liu, B.; Jordan, R. Daily insolation on surfaces tilted towards equator. *ASHRAE J.* **1961**, *10*, 526–541.
5. Duffie, J.A.; Beckman, W.A.; Worek, W.M. *Solar Engineering of Thermal Processes*, 2nd ed.; John Wiley & Sons: New York, NY, USA, 1991.

6. Badescu, V. 3D isotropic approximation for solar diffuse irradiance on tilted surfaces. *Renew. Energy* **2002**, *26*, 221–233. [[CrossRef](#)]
7. Grant, R.H.; Heisler, G.M. Obscured Overcast Sky Radiance Distributions for Ultraviolet and Photosynthetically Active Radiation. *J. Appl. Meteorol.* **1997**, *36*, 1336–1345. [[CrossRef](#)]
8. Kambezidis, H.D.; Psiloglou, B.E.; Gueymard, C. Measurements and models for total solar irradiance on inclined surface in Athens, Greece. *Sol. Energy* **1994**, *53*, 177–185. [[CrossRef](#)]
9. Gueymard, C. An anisotropic solar irradiance model for tilted surfaces and its comparison with selected engineering algorithms. *Sol. Energy* **1987**, *38*, 367–386. [[CrossRef](#)]
10. Hay, J.E. Calculation of monthly mean solar radiation for horizontal and inclined surfaces. *Sol. Energy* **1979**, *23*, 301–307. [[CrossRef](#)]
11. Reindl, D.T.; Beckman, W.A.; Duffie, J.A. Evaluation of hourly tilted surface radiation models. *Sol. Energy* **1990**, *45*, 9–17. [[CrossRef](#)]
12. Skartveit, A.; Asle Olseth, J. Modelling slope irradiance at high latitudes. *Sol. Energy* **1986**, *36*, 333–344. [[CrossRef](#)]
13. Notton, G.; Cristofari, C.; Poggi, P. Performance evaluation of various hourly slope irradiation models using Mediterranean experimental data of Ajaccio. *Energy Convers. Manag.* **2006**, *47*, 147–173. [[CrossRef](#)]
14. Gueymard, C.A. Advanced solar irradiance model and procedure for spectral solar heat gain calculation. *ASHRAE Trans.* **2007**, *113 Pt 1*, 149–164.
15. Gueymard, D.R.; Myers, C.A. *Validation and Ranking Methodologies for Solar Radiation Models*; Springer: Berlin/Heidelberg, Germany, 2008.
16. Yang, D. Solar radiation on inclined surfaces: Corrections and benchmarks. *Sol. Energy* **2016**, *136*, 288–302. [[CrossRef](#)]
17. Li, D.H.W.; Lam, J.C.; Lau, C.C.S. A new approach for predicting vertical global solar irradiance. *Renew. Energy* **2002**, *25*, 591–606. [[CrossRef](#)]
18. Cucumo, M.; De Rosa, A.; Ferraro, V.; Kaliakatsos, D.; Marinelli, V. Experimental testing of models for the estimation of hourly solar radiation on vertical surfaces at Arcavacata di Rende. *Sol. Energy* **2007**, *81*, 692–695. [[CrossRef](#)]
19. Chirattananon, S.; Rukkwansuk, P.; Chaiwiwatworakul, P.; Pakdeepol, P. Evaluation of vertical illuminance and irradiance models against data from north Bangkok. *Build. Environ.* **2007**, *42*, 3894–3904. [[CrossRef](#)]
20. Loutzenhiser, P.G.; Manz, H.; Felsmann, C.; Strachan, P.A.; Frank, T.; Maxwell, G.M. Empirical validation of models to compute solar irradiance on inclined surfaces for building energy simulation. *Sol. Energy* **2007**, *81*, 254–267. [[CrossRef](#)]
21. Perez, R.; Ineichen, P.; Seals, R.; Michalsky, J.; Stewart, R. Modeling daylight availability and irradiance components from direct and global irradiance. *Sol. Energy* **1990**, *44*, 271–289. [[CrossRef](#)]
22. De Miguel, A.; Bilbao, J.; Aguiar, R.; Kambezidis, H.; Negro, E. Diffuse solar irradiation model evaluation in the North Mediterranean Belt area. *Sol. Energy* **2001**, *70*, 143–153. [[CrossRef](#)]
23. Pandey, C.K.; Katiyar, A.K. A comparative study of solar irradiation models on various inclined surfaces for India. *Appl. Energy* **2011**, *88*, 1455–1459. [[CrossRef](#)]
24. Demain, C.; Journée, M.; Bertrand, C. Evaluation of different models to estimate the global solar radiation on inclined surfaces. *Renew. Energy* **2013**, *50*, 710–721. [[CrossRef](#)]
25. Khalil, S.A.; Shaffie, A.M. Performance of Statistical Comparison Models of Solar Energy on Horizontal and Inclined Surface. *Int. J. Energy Power* **2013**, *2*, 8–25.
26. Wattan, R.; Janjai, S. An investigation of the performance of 14 models for estimating hourly diffuse irradiation on inclined surfaces at tropical sites. *Renew. Energy* **2016**, *93*, 667–674. [[CrossRef](#)]
27. Klucher, T.M. Evaluation of models to predict insolation on tilted surfaces. *Sol. Energy* **1979**, *23*, 111–114. [[CrossRef](#)]
28. Martin, N.; Ruiz, J.M. Annual angular reflection losses in PV modules. *Prog. Photovolt. Res. Appl.* **2005**, *13*, 75–84. [[CrossRef](#)]
29. Lave, M.; Hayes, W.; Pohl, A.; Hansen, C.W. Evaluation of global horizontal irradiance to plane-of-array irradiance models at locations across the United States. *IEEE J. Photovolt.* **2015**, *5*, 597–606. [[CrossRef](#)]
30. Maxwell, E.; Wilcox, S. *Users Manual for SERI QC Software, Assessing the Quality of Solar Radiation Data*; National Renewable Energy Laboratory: Golden, CO, USA, 1993.

31. Hay, J.E.; Davies, J.A. Calculation of the solar radiation incident on an inclined surface. In Proceedings of the First Canadian Solar Radiation Data Workshop, Toronto, ON, Canada, 17–19 April 1978; pp. 59–72.
32. Woyte, A.; Richter, M.; Moser, D.; Mau, S.; Reich, N.; Jahn, U. Monitoring of Photovoltaic Systems: Good Practices and Systematic Analysis. *J. Chem. Inf. Model.* **2013**, *53*, 1689–1699.
33. Woyte, A.; Richter, M.; Moser, D.; Reich, N.; Green, M.; Mau, S.; Beyer, H. *Analytical Monitoring of Grid-Connected Photovoltaic Systems—Good Practices for Monitoring and Performance Analysis*; Technical Report; IEA-PVPS: St. Ursen, Switzerland, 2014.
34. Glotzbach, T.; Schulz, B.; Zehner, M.; Fritze, P.; Schlatterer, M.; Vodermayr, C.; Wotruba, G.; Mayer, M. Round-Robin-Test of Irradiance Sensors. In Proceedings of the 23th PVSEC, Valencia, Spain, 1–5 September 2008.
35. King, D.L.; Myers, D.R. Silicon-photodiode pyranometers: operational characteristics, historical experiences, and new calibration procedures. In Proceedings of the Conference Record of the Twenty-Sixth IEEE Photovoltaic Specialists Conference, Anaheim, CA, USA, 29 September–3 October 1997; pp. 1285–1288.
36. Garg, H.P.; Prakash, J. *Solar Energy Fundamentals and Applications*; Tata McGraw-Hill: New York, NY, USA, 2005.
37. Perez, R.; Seals, R.; Ineichen, P.; Stewart, R.; Menicucci, D. A new simplified version of the perez diffuse irradiance model for tilted surfaces. *Sol. Energy* **1987**, *39*, 221–231. [[CrossRef](#)]
38. Hofmann, M.; Seckmeyer, G. A New Model for Estimating the Diffuse Fraction of Solar Irradiance for Photovoltaic System Simulations. *Energies* **2017**, *10*, 248. [[CrossRef](#)]



© 2017 by the authors. Licensee MDPI, Basel, Switzerland. This article is an open access article distributed under the terms and conditions of the Creative Commons Attribution (CC BY) license (<http://creativecommons.org/licenses/by/4.0/>).

4 Outlook

The presented work in the field of irradiance modelling includes two new models for the irradiance processing in PV system simulations, a thorough analysis of the influence of the irradiance model chain on the output of PV simulations and a detailed validation study of models for the calculation of the irradiance on tilted planes. While the author hopes that this work will be a valuable contribution for the PV community, there are a few details in the algorithms where the author still sees room for improvement.

With regard to the first model, the synthesis of one-minute time series of the global irradiance, the following possible further improvements come to mind. Dawn and dusk situations might need a separate modelling approach as the global irradiance follows a very specific pattern during sunrise and sunset that is not representable by transition probability matrices (TPM) in a satisfying manner. Also, the transitions from one synthesized hour to the next might profit from a bit more algorithmic finesse. It would be interesting to investigate the effect of an increase of weather detection classes used to categorize the input data. Another interesting possible improvement would be to base both the TPM and the algorithm itself on the ESRA [88] or Rest2 [89] clear-sky model that were found to be the most accurate in recent studies [90], [91], [92], [93]. Finally, it can be assumed that a more careful modelling of irradiance enhancement effects and integration of recent research results would be another promising point of improvement [19], [94], [95].

Improvements of diffuse fraction model would include a more profound analysis and modelling of the minimal diffuse fraction that is reached during clear-sky days. In the version of the algorithm presented here the determination of the minimal diffuse fraction already forms a major part of the algorithm. In the author's opinion there is still the possibility for improvement, and a realization of this improvement would without doubt increase the model quality a lot. Similar to the proposed improvements of the synthesis algorithm, it might ameliorate the diffuse fraction model as well if more weather detection classes and a state-of-the-art clear-sky model were incorporated.

Apart from the two new algorithms presented here, the author sees an utmost importance to analyze more in detail and improve the transposition models that calculate the irradiance on the titled plane. The publications presented here showed that there are still considerable uncertainties and are in good agreement with similar studies [84], while the investigations on the effects of transposition models on the simulation output also indicated a strong influence. A possible approach would be to use methods to derive the spectral sky radiance from all-sky camera images [96], [97] or from measurements performed by the newly developed multidirectional spectroradiometer [98], deduce the distribution of the diffuse irradiance over the sky dome and correlate these distributions with statistical meteorological features in order to extrapolate them to other locations.

The ground reflected irradiance would be another interesting field to investigate, especially with new bi-facial PV modules coming into the market.

5 Declaration of Authorship / Eidesstattliche Erklärung

I hereby declare that the thesis submitted is my own unaided work. All direct or indirect sources used are acknowledged as references.

Ich erkläre hiermit an Eides statt, dass ich die vorliegende Arbeit selbständig angefertigt habe. Die aus fremden Quellen direkt und indirekt übernommenen Gedanken sind als solche kenntlich gemacht.

Berlin, 14.12.2018

Martin Hofmann

6 Acknowledgements

First of all, I want to thank my supervisor Prof. Dr. Gunther Seckmeyer of the Institute of Climatology and Meteorology (IMuK) at the Leibniz University of Hannover for accepting me as an external Ph.D. student and for all his valuable support over the years. His scientific precision and experience is an invaluable source of inspiration for any of his students and I am very happy and proud that I was given the opportunity to work with him in this context.

I also want to thank my second supervisor, Dr. Rolf Brendel for inviting me to his institute and giving me the opportunity to present my ideas to his team.

A special thank goes to Prof. Dr. Volker Quaschnig, my professor during my bachelor and master years at HTW Berlin, for introducing me to the world of the renewable energy systems and especially to the field of modelling and simulation.

Stefan Riechelmann, Cristian Crisosto and Riyad Mubarak, co-authors of the first paper and like me PhD students in Prof. Dr. Seckmeyer's group, were of great help in developing the ideas of the algorithms, discussing the concepts and exchanging ideas and methodology. Thanks a lot, guys!

A warm thank also to my colleague Rainer Hunfeld and my boss Steffen Lindemann at Valentin Software, Berlin, for their support both technically and in terms of being flexible to provide me with enough free time to work on my thesis. Without such friendly, supporting and understanding colleagues and managers it would not have been possible for me to conduct this work parallel to my work as a software developer of PV*SOL.

I would further like to thank Jan Remund of Meteotest, Switzerland, for the fruitful discussions on irradiance modelling, for validating my new synthesizing algorithm thoroughly and, of course, for including it into the widely known climate data software MeteoNorm.

Ben Liley from the National Institute of Water and Atmospheric Research, New Zealand, has always been open to discuss irradiance modelling topics when we met at the institute or at conferences, and helped me a great deal in bringing forward the English language quality of the abstract. Thanks a lot for that!

Thanks also to my good friends Peter and Simon who were so kind to proofread good deals of the work and uncovered some issues of organizational blindness in my writing with their fresh and sharp logical view.

Finally, I want to thank you, Dona, for your lovely support over the years, for being so understandable when I had to work until late in the evening or on weekends. And especially thank you for encouraging me to continue this undertaking in the last years where progress was so little.

I really appreciate the support from all of you, knowing that without you this work would not have been possible.

7 References

- [1] M. Hofmann, S. Riechelmann, C. Crisosto, R. Mubarak, and G. Seckmeyer, "Improved Synthesis of Global Irradiance with One-Minute Resolution for PV System Simulations," *Int. J. Photoenergy*, vol. 2014, pp. 1–10, 2014.
- [2] M. Hofmann and G. Seckmeyer, "A New Model for Estimating the Diffuse Fraction of Solar Irradiance for Photovoltaic System Simulations," *Energies*, vol. 10, no. 2, p. 248, 2017.
- [3] M. Hofmann and G. Seckmeyer, "Influence of Various Irradiance Models and Their Combination on Simulation Results of Photovoltaic Systems," *Energies*, vol. 10, no. 10, p. 1495, Sep. 2017.
- [4] R. Mubarak, M. Hofmann, S. Riechelmann, and G. Seckmeyer, "Comparison of Modelled and Measured Tilted Solar Irradiance for Photovoltaic Applications," *Energies*, vol. 10, no. 11, p. 1688, Oct. 2017.
- [5] SolarPower Europe, "Global Market Outlook For Solar Power / 2017 - 2021," Brussels, 2017.
- [6] Advanced Energy Economy Institute (AEE Institute), "Competitiveness of renewable energy and energy efficiency in the U.S. markets," Washington DC, 2015.
- [7] M. J. De Wild-Scholten, "Energy payback time and carbon footprint of commercial photovoltaic systems," *Sol. Energy Mater. Sol. Cells*, vol. 119, pp. 296–305, 2013.
- [8] C. J. Sarasa-Maestro, R. Dufo-López, and J. L. Bernal-Agustín, "Photovoltaic remuneration policies in the European Union," *Energy Policy*, vol. 55, pp. 317–328, Apr. 2013.
- [9] C. A. Gueymard, "A review of validation methodologies and statistical performance indicators for modeled solar radiation data: Towards a better bankability of solar projects," *Renew. Sustain. Energy Rev.*, vol. 39, pp. 1024–1034, Nov. 2014.
- [10] Valentin Software, "PV*SOL premium." Valentin Software, Berlin, Germany, 2017.
- [11] J. W. Spencer, "A comparison of methods for estimating hourly diffuse solar radiation from global solar radiation," *Sol. Energy*, vol. 29, no. 1, pp. 19–32, 1982.
- [12] "DIN 5031-1 Optical radiation physics and illuminating engineering; quantities, symbols and units of radiation physics," 1982.
- [13] G. Kopp and J. L. Lean, "A new, lower value of total solar irradiance: Evidence and climate significance," *Geophys. Res. Lett.*, vol. 38, no. 1, 2011.
- [14] N. G. Loeb *et al.*, "Toward Optimal Closure of the Earth's Top-of-Atmosphere Radiation Budget," *J. Clim.*, vol. 22, no. 3, pp. 748–766, Feb. 2009.
- [15] K. E. Trenberth, J. T. Fasullo, and J. Kiehl, "Earth's Global Energy Budget," *Bull. Am. Meteorol. Soc.*, vol. 90, no. 3, pp. 311–323, Mar. 2009.
- [16] ASTM, "Solar Constant and Zero Air Mass Solar Spectral Irradiance," *Annu. B. ASTM Stand.*, vol. 15.03, pp. 1–16, 2006.
- [17] Astm, "References Solar Spectral Irradiance at Air Mass 1.5: Direct Normal and Hemispherical for a 37° Tilted Surface 1," *Policy*, vol. 14, pp. 1–10, 2004.
- [18] R. H. Inman, Y. Chu, and C. F. M. Coimbra, "Cloud enhancement of global horizontal irradiance in California and Hawaii," *Sol. Energy*, vol. 130, pp. 128–138, Jun. 2016.
- [19] C. A. Gueymard, "Cloud and albedo enhancement impacts on solar irradiance using high-frequency measurements from thermopile and photodiode radiometers. Part 1: Impacts on global horizontal irradiance," *Sol. Energy*, vol. 153, pp. 755–765, 2017.
- [20] G. L. Stephens and S. -C Tsay, "On the cloud absorption anomaly," *Q. J. R. Meteorol. Soc.*, vol. 116, no. 493, pp.

- 671–704, 1990.
- [21] K.-N. Liou, “On the Absorption, Reflection and Transmission of Solar Radiation in Cloudy Atmospheres,” *J. Atmos. Sci.*, vol. 33, no. 5, pp. 798–805, May 1976.
- [22] A. Kokhanovsky, “Optical properties of terrestrial clouds,” *Earth-Science Rev.*, vol. 64, no. 3–4, pp. 189–241, 2004.
- [23] K. A. Prather, C. D. Hatch, and V. H. Grassian, “Analysis of Atmospheric Aerosols,” *Annu. Rev. Anal. Chem.*, vol. 1, no. 1, pp. 485–514, Jul. 2008.
- [24] R. R. Cordero *et al.*, “Aerosol effects on the UV irradiance in Santiago de Chile,” *Atmos. Res.*, vol. 149, pp. 282–291, 2014.
- [25] J. Lenoble *et al.*, “Retrieval of the ultraviolet aerosol optical depth during a spring campaign in the Bavarian Alps,” *Appl. Opt.*, vol. 41, no. 9, p. 1629, Mar. 2002.
- [26] R. Levy, C. Hsu, A. Sayer, S. Mattoo, and L. J., “MODIS Atmosphere L2 Aerosol Product.” NASA MODIS Adaptive Processing System, Goddard Space Flight Center, 2015.
- [27] R. G. Pinnick, J. M. Rosen, and D. J. Hofmann, “Measured light-scattering properties of individual aerosol particles compared to mie scattering theory,” *Appl. Opt.*, vol. 12, no. 1, pp. 37–41, 1973.
- [28] E. J. Highwood *et al.*, “Aerosol scattering and absorption during the EUCAARI-LONGREX flights of the Facility for Airborne Atmospheric Measurements (FAAM) BAe-146: Can measurements and models agree?,” *Atmos. Chem. Phys.*, vol. 12, no. 15, pp. 7251–7267, 2012.
- [29] D. G. Kaskaoutis, H. D. Kambezidis, N. Hatzianastassiou, P. G. Kosmopoulos, and K. V. S. Badarinath, “Aerosol climatology: dependence of the Angstrom exponent on wavelength over four AERONET sites,” *Atmos. Chem. Phys. Discuss.*, 2007.
- [30] K.-N. Liou, *An introduction to Atmospheric Radiation, 2nd Edition*, 2nd ed., vol. 84, no. 590. Academic Press An imprint of Elsevier Science, 2002.
- [31] P. Stier, J. H. Seinfeld, S. Kinne, and O. Boucher, “Aerosol absorption and radiative forcing,” *Atmos. Chem. Phys.*, vol. 7, no. 19, pp. 5237–5261, Oct. 2007.
- [32] U. Lohmann *et al.*, “Total aerosol effect: Radiative forcing or radiative flux perturbation?,” *Atmos. Chem. Phys.*, vol. 10, no. 7, pp. 3235–3246, 2010.
- [33] N. Bellouin, O. Boucher, J. Haywood, and M. S. Reddy, “Global estimate of aerosol direct radiative forcing from satellite measurements,” *Nature*, vol. 438, no. 7071, pp. 1138–1141, 2005.
- [34] D. G. Kaskaoutis, H. D. Kambezidis, U. C. Dumka, and B. E. Psiloglou, “Dependence of the spectral diffuse-direct irradiance ratio on aerosol spectral distribution and single scattering albedo,” *Atmos. Res.*, vol. 178–179, pp. 84–94, Sep. 2016.
- [35] J. A. Ruiz-Arias, J. Dudhia, and C. A. Gueymard, “A simple parameterization of the short-wave aerosol optical properties for surface direct and diffuse irradiances assessment in a numerical weather model,” *Geosci. Model Dev.*, vol. 7, no. 3, pp. 1159–1174, Jun. 2014.
- [36] B. N. Holben *et al.*, “AERONET—A Federated Instrument Network and Data Archive for Aerosol Characterization,” *Remote Sens. Environ.*, vol. 66, no. 1, pp. 1–16, 1998.
- [37] O. Dubovik *et al.*, “Variability of Absorption and Optical Properties of Key Aerosol Types Observed in Worldwide Locations,” *J. Atmos. Sci.*, vol. 59, no. 3, pp. 590–608, Feb. 2002.
- [38] K. H. Rosenlof and G. C. Reid, “Trends in the temperature and water vapor content of the tropical lower stratosphere: Sea surface connection,” *J. Geophys. Res. Atmos.*, vol. 113, no. 6, 2008.
- [39] H. Kraus, *Die Atmosphäre der Erde - Eine Einführung in die Meteorologie*. 2004.

- [40] E. J. Mlawer *et al.*, “Comparison of spectral direct and diffuse solar irradiance measurements and calculations for cloud-free conditions,” *Geophys. Res. Lett.*, vol. 27, no. 17, pp. 2653–2656, 2000.
- [41] E. Borbas, P. Menzel, and B. Gao, “MODIS Atmosphere L2 Water Vapor Product.” NASA MODIS Adaptive Processing System, Goddard Space Flight Center, 2015.
- [42] Lord Rayleigh, “On the scattering of light by small particles,” *Philos. Mag.*, vol. 41, no. 4, pp. 447–454, 1871.
- [43] D. R. Bates, “Rayleigh scattering by air,” *Planet. Space Sci.*, vol. 32, no. 6, pp. 785–790, 1984.
- [44] R. Thalman, K. J. Zarzana, M. A. Tolbert, and R. Volkamer, “Rayleigh scattering cross-section measurements of nitrogen, argon, oxygen and air,” *J. Quant. Spectrosc. Radiat. Transf.*, vol. 147, pp. 171–177, 2014.
- [45] S. Senthilarasu, E. F. Fernández, F. Almonacid, and T. K. Mallick, “Effects of spectral coupling on perovskite solar cells under diverse climatic conditions,” *Sol. Energy Mater. Sol. Cells*, vol. 133, pp. 92–98, Feb. 2015.
- [46] M. Hofmann, P. Vanicek, and H. R., “Is the Average Photon Energy (APE) a Suitable Measure to Describe the Uniqueness of Solar Spectra?Title,” *29th Eur. Photovolt. Sol. Energy Conf. Exhib.*, pp. 3461–3466, 2014.
- [47] Meteonorm, “Meteonorm Handbook part II : Theory. V7,” no. May, p. 82, 2012.
- [48] T. Cebecauer and M. Suri, “Typical Meteorological Year Data: SolarGIS Approach,” *Energy Procedia*, vol. 69, pp. 1958–1969, May 2015.
- [49] C. Rigollier, M. Lefèvre, and L. Wald, “The method Heliosat-2 for deriving shortwave solar radiation from satellite images,” *Sol. Energy*, vol. 77, no. 2, pp. 159–169, 2004.
- [50] U. Pfeifroth *et al.*, “Surface Radiation Data Set - Heliosat (SARAH) - Edition 2,” Jan. 2017.
- [51] B. Burger and R. Rütther, “Inverter sizing of grid-connected photovoltaic systems in the light of local solar resource distribution characteristics and temperature,” *Sol. Energy*, vol. 80, no. 1, pp. 32–45, 2006.
- [52] S. Ransome and P. Funtan, “Why hourly averaged measurement data is insufficient to model PV performance accurately,” *20th Eur. Photovolt. Sol. Energy Conf.*, pp. 2752–2755, 2005.
- [53] B. Y. H. Liu and R. C. Jordan, “The interrelationship and characteristic distribution of direct, diffuse and total solar radiation,” *Sol. Energy*, vol. 4, no. 3, pp. 1–19, 1960.
- [54] J. F. Orgill and K. G. T. Hollands, “Correlation equation for hourly diffuse radiation on a horizontal surface,” *Sol. Energy*, vol. 19, no. 4, pp. 357–359, 1977.
- [55] A. Skartveit and J. A. Olseth, “A model for the diffuse fraction of hourly global radiation,” *Sol. Energy*, vol. 38, no. 4, pp. 271–274, 1987.
- [56] D. T. Reindl, W. A. Beckman, and J. A. Duffie, “Diffuse fraction corrections,” *Sol. Energy*, vol. 45, no. 1, pp. 1–7, 1990.
- [57] R. Perez, P. Ineichen, R. Seals, J. Michalsky, and R. Stewart, “Modeling daylight availability and irradiance components from direct and global irradiance,” *Sol. Energy*, vol. 44, no. 5, pp. 271–289, 1990.
- [58] A. Skartveit, J. A. Olseth, and M. E. Tuft, “An hourly diffuse fraction model with correction for variability and surface albedo,” *Sol. Energy*, vol. 63, no. 3, pp. 173–183, 1998.
- [59] W. Köppen, “Klassifikation der Klimate nach Temperatur, Niederschlag und Jahresablauf (Classification of climates according to temperature, precipitation and seasonal cycle).,” *Petermanns geographische Mitteilungen*, vol. 64, pp. 193–203, 1918.
- [60] M. Kottke, J. Grieser, C. Beck, B. Rudolf, and F. Rubel, “World Map of Köppen – Geiger Climate Classification,” *Meteorol. Z.*, vol. 15, pp. 259–263, 2006.
- [61] G. König-Langlo and R. Sieger, “Report of the working group BSRN - Baseline Surface Radiation Network,” in *AIP Conference Proceedings*, 2013, vol. 1531, pp. 668–671.

- [62] G. König-Langlo, A. Bücken, F. Richter, and R. Sieger, "BSRN snapshot 2013-07 in two ISO image files (4.84 GB)." 01-Jan-2013.
- [63] G. König-Langlo, R. Sieger, H. Schmithüsen, A. Bücken, F. Richte, and E. G. Dutton, "Baseline Surface Radiation Network (BSRN) Update of the Technical Plan for BSRN Data Management," 2013.
- [64] S. A. Klein, "Calculation of monthly average insolation on tilted surfaces," *Solar Energy*, vol. 19, no. 4, pp. 325–329, 1977.
- [65] R. B. Benson, M. V. Paris, J. E. Sherry, and C. G. Justus, "Estimation of daily and monthly direct, diffuse and global solar radiation from sunshine duration measurements," *Sol. Energy*, vol. 32, no. 4, pp. 523–535, 1984.
- [66] M. Iqbal, "A study of Canadian diffuse and total solar radiation data-I Monthly average daily horizontal radiation," *Sol. Energy*, vol. 22, no. 1, pp. 81–86, 1979.
- [67] B. Bartoli *et al.*, "Statistical correlation between daily and monthly averages of solar-radiation data," *Nuovo Cim. C*, vol. 2, no. 2, pp. 222–234, 1979.
- [68] R. J. Aguiar, M. Collares-Pereira, and J. P. Conde, "Simple procedure for generating sequences of daily radiation values using a library of Markov transition matrices," *Sol. Energy*, vol. 40, no. 3, pp. 269–279, 1988.
- [69] R. J. Aguiar and M. Collares-Pereira, "The modelling of daily sequences of hourly radiation through autoregressive methods," *Clean and Safe Energy Forever. Proceedings of the 1989 Congress of the International Solar Energy Society*. 1990.
- [70] R. Aguiar and M. Collares-Pereira, "TAG: A time-dependent, autoregressive, Gaussian model for generating synthetic hourly radiation," *Sol. Energy*, 1992.
- [71] L. Mora-López and M. Sidrach-De-Cardona, "Multiplicative arma models to generate hourly series of global irradiation," *Sol. Energy*, vol. 63, no. 5, pp. 283–291, 1998.
- [72] A. Skartveit and J. A. Olseth, "The probability density and autocorrelation of short-term global and beam irradiance," *Sol. Energy*, vol. 49, no. 6, pp. 477–487, Dec. 1992.
- [73] C. A. Balafas, M. D. Athanassopoulou, T. Argyropoulos, P. Skafidas, and C. T. Dervos, "Effect of the diffuse solar radiation on photovoltaic inverter output," in *Proceedings of the Mediterranean Electrotechnical Conference - MELECON*, 2010, pp. 58–63.
- [74] J. D. Mondol, Y. G. Yohanis, and B. Norton, "Solar radiation modelling for the simulation of photovoltaic systems," *Renew. Energy*, vol. 33, no. 5, pp. 1109–1120, 2008.
- [75] G. Notton, P. Poggi, and C. Cristofari, "Predicting hourly solar irradiances on inclined surfaces based on the horizontal measurements: Performances of the association of well-known mathematical models," *Energy Convers. Manag.*, vol. 47, no. 13–14, pp. 1816–1829, 2006.
- [76] M. Diez-Mediavilla, A. De Miguel, and J. Bilbao, "Measurement and comparison of diffuse solar irradiance models on inclined surfaces in Valladolid (Spain)," *Energy Convers. Manag.*, vol. 46, no. 13–14, pp. 2075–2092, 2005.
- [77] T. M. Klucher, "Evaluation of models to predict insolation on tilted surfaces," *Sol. Energy*, vol. 23, no. 2, pp. 111–114, 1979.
- [78] J. E. HAY and J. A. Davies, "Calculation of the Solar Radiation Incident on an Inclined Surface," in *Proceedings of First Canadian Solar Radiation Data Workshop*, 1980.
- [79] D. T. Reindl, W. A. Beckman, and J. A. Duffie, "Evaluation of hourly tilted surface radiation models," *Sol. Energy*, vol. 45, no. 1, pp. 9–17, 1990.
- [80] C. Gueymard, "An anisotropic solar irradiance model for tilted surfaces and its comparison with selected engineering algorithms," *Sol. Energy*, vol. 38, no. 5, pp. 367–386, 1987.
- [81] T. Muneer, "Solar radiation model for Europe," *Build. Serv. Eng. Res. Technol.*, vol. 11, no. 4, pp. 153–163, Nov.

- 1990.
- [82] T. Muneer, "Solar radiation: Further evaluation of the Muneer model," *Build. Serv. Eng. Res. Technol.*, vol. 11, no. 2, pp. 77–78, 1990.
- [83] A. Skartveit and J. Asle Olseth, "Modelling slope irradiance at high latitudes," *Sol. Energy*, vol. 36, no. 4, pp. 333–344, 1986.
- [84] D. Yang, "Solar radiation on inclined surfaces: Corrections and benchmarks," *Sol. Energy*, vol. 136, no. October, pp. 288–302, 2016.
- [85] C. A. Gueymard and D. R. Myers, "Validation and ranking methodologies for solar radiation models," in *Modeling Solar Radiation at the Earth's Surface: Recent Advances*, 2008, pp. 479–509.
- [86] P. G. Loutzenhiser, H. Manz, C. Felsmann, P. A. Strachan, T. Frank, and G. M. Maxwell, "Empirical validation of models to compute solar irradiance on inclined surfaces for building energy simulation," *Sol. Energy*, vol. 81, no. 2, pp. 254–267, 2007.
- [87] H. D. Kambezidis, B. E. Psiloglou, and C. Gueymard, "MEASUREMENTS AND MODELS FOR TOTAL SOLAR IRRADIANCE ON INCLINED SURFACE IN ATHENS, GREECE," *Sol. Enerav*, vol. 53, no. 2, pp. 177–185, 1994.
- [88] C. Rigollier, O. Bauer, and L. Wald, "On the clear sky model of the ESRA — European Solar Radiation Atlas — with respect to the heliosat method," *Sol. Energy*, vol. 68, no. 1, pp. 33–48, 2000.
- [89] C. A. Gueymard, "REST2: High-performance solar radiation model for cloudless-sky irradiance, illuminance, and photosynthetically active radiation - Validation with a benchmark dataset," *Sol. Energy*, vol. 82, no. 3, pp. 272–285, 2008.
- [90] N. A. Engerer and F. P. Mills, "Validating nine clear sky radiation models in Australia," *Sol. Energy*, vol. 120, 2015.
- [91] P. Ineichen, "Validation of models that estimate the clear sky global and beam solar irradiance," *Sol. Energy*, vol. 132, pp. 332–344, Jul. 2016.
- [92] C. A. Gueymard, "Clear-sky irradiance predictions for solar resource mapping and large-scale applications: Improved validation methodology and detailed performance analysis of 18 broadband radiative models," *Solar Energy*, vol. 86, no. 8, pp. 2145–2169, 2012.
- [93] M. Meyer, "Analyse von Modellen zur Berechnung der Clear-Sky-Strahlung," Hochschule für Technik und Wirtschaft Berlin, 2017.
- [94] A. Voskresbenzev, S. Riechelmann, A. Bais, H. Slaper, and G. Seckmeyer, "Estimating probability distributions of solar irradiance," *Theor. Appl. Climatol.*, vol. 119, no. 3–4, pp. 465–479, Feb. 2015.
- [95] C. A. Gueymard, "Cloud and albedo enhancement impacts on solar irradiance using high-frequency measurements from thermopile and photodiode radiometers. Part 2: Performance of separation and transposition models for global tilted irradiance," *Sol. Energy*, vol. 153, pp. 766–779, Sep. 2017.
- [96] K. Tohsing, M. Schrempf, S. Riechelmann, H. Schilke, and G. Seckmeyer, "Measuring high-resolution sky luminance distributions with a CCD camera.," *Appl. Opt.*, vol. 52, no. 8, pp. 1564–1573, 2013.
- [97] K. Tohsing, M. Schrempf, S. Riechelmann, and G. Seckmeyer, "Validation of spectral sky radiance derived from all-sky camera images - A case study," *Atmos. Meas. Tech.*, vol. 7, no. 7, pp. 2137–2146, 2014.
- [98] S. Riechelmann, M. Schrempf, and G. Seckmeyer, "Simultaneous measurement of spectral sky radiance by a non-scanning multidirectional spectroradiometer (MUDIS)," *Meas. Sci. Technol.*, vol. 24, no. 12, 2013.

Curriculum Vitae

Personal Details	Name	Martin Hofmann
	Date of Birth	16 April 1983
	Place of Birth	Mannheim, Germany
University	10/2008 - 02/2011	HTW Berlin, Renewable Energy Systems (M.Sc.) Grade 1.2 – “With distinction“, best student Thesis: „Validierung und Weiterentwicklung des Modells zur Bestimmung der I-U-Kennlinie von PV-Modulen in PV*Sol“
	10/2005 - 09/2008	FHTW Berlin, Renewable Energy Systems (B.Sc.) Grade 1.42 Thesis: „Modellierung & Simulation konzentrierender Photovoltaik-Anlagen“
	10/2003 - 09/2004	Technische Universität Darmstadt, Physics (B.Sc.)
Professional Career	Since 10/2011	Software Engineer for Photovoltaics & Modelling at Valentin Software Berlin
	03/2011 - 09/2011	Project engineer for Photovoltaics at DGS Berlin
	10/2008 - 09/2010	Student assistant for Prof. Dr. Quaschnig at HTW Berlin
	02/2006 - 02/2008	Student assistant at Hahn-Meitner-Institut Berlin (HMI – now HZB), Department Solar Energy Research 3 – Institute for Technology
	11/2004 - 09/2005	One-year employment for prototype design of a two-axis tracking concentrating PV system at Sunvention GmbH, Heppenheim
Personal projects	Since 03/2011	Technical development, design and maintenance of the meteorological measurement system of the HTW Berlin
	10/2008 - 07/2010	Participation at the Solar Decathlon Europe 2010, Madrid, Spain, for the construction of a plus energy house (team lead and head of solar systems)

- Publications
- M. Hofmann, S. Riechelmann, C. Crisosto, R. Mubarak, and G. Seckmeyer, “Improved synthesis of global irradiance with one-minute resolution for PV system simulations,” *Int. J. Photoenergy*, vol. 2014, 2014.
<https://www.hindawi.com/journals/ijp/2014/808509/>
- M. Hofmann and G. Seckmeyer, “A New Model for Estimating the Diffuse Fraction of Solar Irradiance for Photovoltaic System Simulations,” *Energies*, vol. 10, no. 2, p. 248, 2017.
<http://www.mdpi.com/1996-1073/10/2/248>
- M. Hofmann and G. Seckmeyer, “Influence of Various Irradiance Models and Their Combination on Simulation Results of Photovoltaic Systems,” *Energies*, vol. 10, no. 10, p. 1495, Sep. 2017.
<http://www.mdpi.com/1996-1073/10/10/1495>
- R. Mubarak, M. Hofmann, S. Riechelmann, and G. Seckmeyer, “Comparison of Modelled and Measured Tilted Solar Irradiance for Photovoltaic Applications,” *Energies*, vol. 10, no. 11, p. 1688, Oct. 2017.
<http://www.mdpi.com/1996-1073/10/11/1688>
-
- Conference Contributions
- EU PVSEC 2017, Amsterdam
- Talk: *A new model for the calculation of the diffuse irradiance from global irradiance time series*
- PV Symposium 2017, Bad Staffelstein
- Poster: *Solare Elektromobilität – welches E-Auto fährt am besten mit der Sonne?*
- EU PVSEC 2016, Munich
- Poster: *Modelling PV modules based on IEC 61583 data*
- EU PVSEC 2014, Amsterdam
- Talk: *Improved simulation of PV systems by an algorithm generating irradiance data with one minute resolution*
- Poster: *Is the average photon energy (APE) a suitable measure to describe the uniqueness of solar spectra?*
- PV Symposium 2014, Bad Staffelstein
- Poster: *Analyse und Weiterentwicklung von Algorithmen zur Generation von Minutenwerten aus Stundenwerten der Globalstrahlung*
- PV Symposium 2012, Bad Staffelstein
- Poster: *Entwicklung der Parameter des Zwei-Dioden-Modells aus Datenblatt-Angaben für die Ertrags-Simulation von PV-Modulen*